SLAC-R-576

Generation and Use of Coherent Transition Radiation from Short Electron Bunches[1]

Chitrlada Settakorn
Stanford Linear Accelerator Center
Stanford University
Stanford, CA 94309

SLAC-Report-576
August 2001

Prepared for the Department of Energy
under contract number DE-AC03-76SF00515

Printed in the United States of America. Available from the National Technical Information Service, U.S. Department of Commerce, 5285 Port Royal Road, Springfield, VA 22161.

[1] Ph.D. thesis, Stanford Linear Accelerator Center OR Stanford University, Stanford, CA 94309.

Abstract

When accelerated, an electron bunch emits coherent radiation at wavelength longer than or comparable to the bunch length. The coherent radiation intensity scales with the square of the number of electron per bunch and its radiation spectrum is determined by the Fourier Transform of the electron bunch distribution squared. At the SUNSHINE (Stanford UNiversity SHort INtense Electron source) facility, electron bunches can be generated as short as $\sigma_z = 36$ μm (120 femtosecond duration) and such bunches can emit coherent radiation in the far-infrared. Since a typical number for the electron population in a bunch is $10^8 - 10^9$, the coherent radiation intensity is much higher than that of incoherent radiation as well as that of a conventional far-infrared radiation source.

This thesis concentrates on coherent transition and diffraction radiation from short electron bunches as a potential high intensity far-infrared radiation source and for sub-picosecond electron bunch length measurements. Coherent transition radiation generated from a 25 MeV beam at a vacuum-metal interface is characterized. Such a high intensity radiation source allows far-infrared spectroscopy to be conducted conveniently with a Michelson interferometer and a room temperature detector. Measurements of the refractive index of silicon are described to demonstrate the possibilities of far-infrared spectroscopy using coherent transition radiation. Coherent diffraction radiation, which is closely related to coherent transition radiation, can be considered as another potential FIR radiation source. Since the perturbation by the radiation generation to the electron beam is relatively small, it has the advantage of being a nondestructive radiation source. The coherent diffraction radiation, therefore, can be generated at several experimental stations along the beam trajectory. To further

increase the intensity of the radiation, stimulated coherent transition radiation is considered. The stimulation can be done by circulating radiation pulses generated by previous electron bunches in an optical cavity while adjusting the cavity length such that these radiation pulses coincide at the radiator with incoming electron bunches to stimulate more radiation from the electrons. In this thesis, detailed studies on this subject are presented with the goal of obtaining as high a stimulation as possible. Experimental results confirming the expected performance of stimulation will be discussed.

Not only does the high intensity of coherent transition radiation make the radiation by itself outstanding, its radiation spectrum carries information of the particle distribution which allows a bunch length measurement technique capable of measuring sub-picosecond electron bunches. The technique extracts bunch length information from an autocorrelation of the coherent transition radiation generated from the electron bunch. Impact of experimental conditions on the measurement have been investigated. These effects can lead to wrong experimental conclusions and need to be evaluated to interpret the measurement correctly. By featuring coherent radiation properties, coherent diffraction radiation can be used for autocorrelation bunch length measurement as well with the great advantage of being nondestructive. However, subtleties of diffraction radiation spectrum impact the accuracy of bunch length measurement and data analysis must be done carefully. Autocorrelation bunch length measurements with diffraction radiation, evaluation, and limitation of the technique will be discussed in this thesis.

Acknowledgements

Without help and support from many people and organizations, the completion of this thesis would not have been possible. I am very grateful to all of them.

First of all, I would like to thank my advisor Prof. Helmut Wiedemann for his advice, guidance and encouragement through the project. I treasure the opportunity and experience of doing research under his supervision at SUNSHINE. Without his efforts (from introducing me into the field of accelerator physics, providing valuable guidance, to carefully correcting my manuscript), this thesis would simply not exist.

Next, I would like to express my gratitude to all members that served on my reading and examination committee: Prof. Robert Byer, Prof. Ingolf Lindau, Prof. Tor Raubenheimer, Prof. Herman Winick, with my deep appreciation to Prof. Raubenheimer and Prof. Winick for their time and efforts in reading and polishing this thesis to better the work.

I wish to acknowledge the Development and Promotion of Science and Technology Talents project under the Royal Thai Government for the generous scholarship during my undergraduate and parts of graduate studies. I am also very thankful to SSRL management for their RA fellowships from DOE (contract number DE-AC03-76SF00515) during the last years of my graduate studies.

In addition to their friendships, I would like to thank my colleagues for their help and contribution. The following is just part of their contribution. Dr. Pamela Kung did much of initial work on the electron bunch generation. Dr. Hung-Chi Lihn developed the bunch length measurement technique and did initial work on the stimulated transition radiation experiments. Dr. David Bocek and Mike Hernandez gave me a lot of useful advice on accelerator operation and instrumentation. I also

benefited from Davis's feedback control system for the cathode heater. Alex Leung wrote the PC programs to acquire and analyze the transverse beam profiles. Kristina Woods suggested to me several interesting papers of far-infrared spectroscopy and gave me useful suggestions on this subject. I am also in great debt to Jim Sebek who provides his time and efforts in answering my questions as well as offering so many constructive suggestions. Jim is my valuable resource not just in physics but in many other subjects.

For their help, suggestions and friendships, I would like to thank the following individuals: Nancy Lai, Dr. Rui Farias, Holger Mannweiler, Dr. Cecile Limborg, Prof. David Whittum, Sakhorn Rimjeam, Yue Yang, Debopriya Das and Manuel Ortega.

Thanks also go to Prof. Todd Smith and Dr. Kenneth Ricci for generously showing me their in-vacuum Michelson interferometer setup, with a special thanks to Kenneth for his insight of the P1-62 detector availability.

For their constant technical assistance, I thank Greg Johnson, Harold Morales, Mike Nalls, Ramona Theobald, Mike Swanson, Kane Zuo and other staff from Mechanical, Electronics, Engineering, and Vacuum Group of SSRL. Mike Hennessy of HEPL also provided help and equipment in several occasions of vacuum break-down. I wish to thank Perron Perron in the Applied Physics main office for being so helpful to me through out my time at Stanford.

I am very thankful to my friends and family who have been a tremendous support. I am grateful to my parents and my dear sister, Jongkolnee Settakorn, for their support and understanding throughout my education. Thanks for all the love they have given me.

Last but not least, I thank Thanakorn Thongbai for his support, for his encouragement and for always being a source of my strength.

Contents

List of Tables

List of Figures

Chapter 1

Introduction

This thesis presents experimental and theoretical investigation on the generation, characterization and use of high intensity far-infrared radiation from short electron bunches. The work has been done at the SUNSHINE (Stanford UNiversity SHort INtense Electron source) facility. The facility is dedicated to study the generation of femtosecond electron bunches and their use in other fields. Most of the past and on-going projects at the SUNSHINE facility are efforts to providing high intensity radiation in the far-infrared, where only a few high intensity radiation sources exist.

When accelerated, an electron bunch can emit coherent radiation at wavelengths longer than or comparable to the bunch length with an intensity proportional to the square of the number of electrons per bunch. Since a typical electron population in a bunch is $10^8 - 10^9$, the coherent radiation intensity generated from electron bunches of some 100 μm is expected to be much higher than incoherent radiation as well as conventional far infrared radiation sources like synchrotron radiation or black body radiation. In principle, any methods to produce radiation from charged-particles can be used to generate coherent radiation. In this thesis, we concentrate specifically on the generation of coherent transition and coherent diffraction radiation.

The generation and characterization of femtosecond electron bunches at the SUNSHINE facility has been studied in the earlier stage of the project [1]. Short electron bunches are generated from an rf-gun with a thermionic cathode and an alpha-magnet. A compressed bunch can be as short as $\sigma_z = 40$ μm and thus allows us to generate

coherent radiation in the far infrared regime. Coherent radiation from an electron bunch and an overview of femtosecond electron-bunch generation will be described in Chapter 2. Experimental characterization of coherent transition radiation generated from short electron bunches at SUNSHINE will be presented in Chapter 4. The characterization covers coherent intensity, total energy measurement, spatial distribution, polarization, spectral distribution and effects of electron beam sizes on the coherent radiation. These studies are significant to complete the characterization of the radiation source at the SUNSHINE facility.

Along with the generation of femtosecond electron bunches, a bunch length measurement technique using autocorrelation of coherent transition radiation has been developed at the SUNSHINE facility [2]. The technique is capable of measuring bunch lengths well below one picosecond and it has been recognized and implemented in many facilities. The impacts of experimental conditions on the measurement have been investigated in this thesis. These impacts can lead to wrong experimental conclusions and need to be considered to interpret the measurement correctly. The effect of humid air to the measurement has been investigated by comparing autocorrelation bunch length measurements made in and outside of the vacuum chamber. The results show significant broadening of radiation pulses after propagating through ambient air. The effects of the pyroelectric detector used in the measurement on the bunch length measurement has been analyzed and is resolved. Transverse effects on the bunch length measurement have been investigated experimentally as well as theoretically.

Coherent diffraction radiation generated from short electron bunches is another subject which has been studied. The radiation itself can be used as a high intensity far-infrared radiation source. Since the electron is less perturbed by the radiation generation, it has the advantage of being a nondestructive radiation source. The radiation, therefore, can be generated at many experimental stations along the beam trajectory. Furthermore, coherent diffraction radiation can be used for nondestructive autocorrelation bunch length measurements. However, subtleties of diffraction radiation spectrum impact the bunch length measurement and the data analysis must be done with care. Autocorrelation bunch length measurements with diffraction radiation at SUNSHINE and the limitations of the technique will be discussed in this

thesis.

To further increase the intensity of the radiation, stimulated coherent transition radiation was considered. The stimulation can be done by circulating radiation pulses generated by previous electron bunches in an optical cavity while adjusting the cavity length such that these radiation pulses coincide at the radiator with an incoming electron bunch to stimulate more radiation from the electrons. The stimulated coherent transition radiation principle has been demonstrated in Ref. [3]. In this thesis, more detailed studies of this subject are presented with the goal of obtaining as high a stimulation as possible. The experimental results confirm the expected performance of stimulation and will be discussed.

High intensity coherent far-infrared radiation from short electron bunches provides a great radiation source for far-infrared research. Far-infrared spectroscopy and some experiments that can be conducted easily with coherent far-infrared radiation generated from short electron bunches at SUNSHINE are discussed in Chapter 8. Optical property measurements of silicon with Dispersive Fourier Transform Spectroscopy technique are presented. Using the same technique, the refractive index of the pyroelectric detector crystal can also be obtained.

The thesis will discuss the generation of coherent radiation from short electron bunches at SUNSHINE in Chapter 2. Chapter 3 describes the experimental setup and instrumentation. Chapter 4 presents a characterization of coherent transition radiation. Chapter 5 reveals important issues concerning an autocorrelation bunch length technique using coherent transition radiation. Chapter 6 presents the coherent diffraction radiation itself as a far-infrared radiation source and the coherent diffraction radiation for nondestructive bunch length measurements. Chapter 7 describes theoretical aspects of the stimulated coherent transition radiation and experimentation. Chapter 8 covers a possible use of the radiation for far-infrared spectroscopy.

Facility	Wavelength tuning range	Peak power
UCSB mm-FEL [5]	338 μm$-$2.5 mm	1-15 kW
UCSB μm-FEL [5]	$63 - 338$ μm	1-6 kW
Stanford FIREFLY [6]	$15 - 65$ μm	100 - 500 kW
CLIO FEL [7]	$3 - 50$ μm	4-100 MW
FELIX [8]	$4 - 250$ μm	0.5-100 MW

Table 1.1: Operating far-infrared FEL facilities

1.1 Far-infrared Radiation

The electromagnetic radiation spectrum between wavelengths of 10 μm -1000 μm is commonly called the far-infrared regime and located between microwave and the infrared band (1 μm - 10 μm). The far-infrared is the spectral range where, for example, the molecule-surface-bond vibrations, intermolecular cluster vibrations, and transition in semiconductor quantum-wells can be excited. It is also the region for probing transitions between adjacent high-lying Rydberg states of atoms and low-frequency motions in large biomolecules. Some far-infrared applications are pump-probe surface science, pump-probe studies of materials, studies of mode-selective chemistry, studies of carrier dynamics of high-Tc superconductors, studies of low-frequency modes of large biomolecules, and plasma diagnostics [4].

There are a few FELs operated in the far-infrared regime. These facilities and their radiation output are listed in Table 1.1. Although FELs are capable of covering most of the far-infrared spectral band within their tuning range, the FEL spectrum is narrow band. A broadband far-infrared radiation source which is commonly used is a thermal source which is considered as a black body radiation source. There are two broadband thermal sources: silicon carbide and mercury lamps, that are conventionally used. The hot silicon carbide source used in commercial infrared spectrometers, commonly called "glowbar", is limited to wavelengths shorter than 100 μm. The mercury discharge lamp is used for wavelengths longer than 100 μm. For reference, the radiance of a black body radiation source is shown in (1.1). The black body radiation

radiance [9],

$$R(W/Sr/m^2/100\%BW) = \frac{2hc^2\nu^4}{[e^{hc\nu/kT}-1]} \approx 2hc^2\nu^4\frac{kT}{hc\nu}, \tag{1.1}$$

where T is black body temperature in Kelvin, ν is wavenumber, h is the Plank constant and k is the Boltzmann constant. The black body radiation will be compared to the coherent transition radiation generated from short electron bunches at SUNSHINE later in this thesis.

1.2 Transition Radiation (TR)

Transition radiation, first predicted by Ginzberg and Frank [10], occurs when a charged particle passes through an interface between media with different dielectric constants. The transition of the dielectric constants of the media along the electron's path causes a discontinuity in the electric field at the interface. This discontinuity readjusts itself as radiation spreading out from the point where the electron passes through the discontinuity. The angular spectral energy density of the transition radiation depends on the dielectric constants of the two media [11],[12]. In this thesis, however, we concentrate only on the vacuum-conductor interface.

1.2.1 General Theory

The simplest case in the theory of transition radiation is an electron traveling at a constant velocity $\vec{v}$ across the boundary between vacuum ($\epsilon = 1$) and a perfect conductor ($\epsilon \to \infty$) in a direction normal to the boundary. The schematic diagram of this case is shown in Figure 1.1. Since the boundary is a perfect conductor, one can simplify this physical model and replace the conductor by a positive image charge on the other side of the conductor surface. The problem can then be described by a two-charged-particle collision problem. The radiation emitted when two charges collide can be derived from the radiation emission when charged particles change their velocities instantaneously.

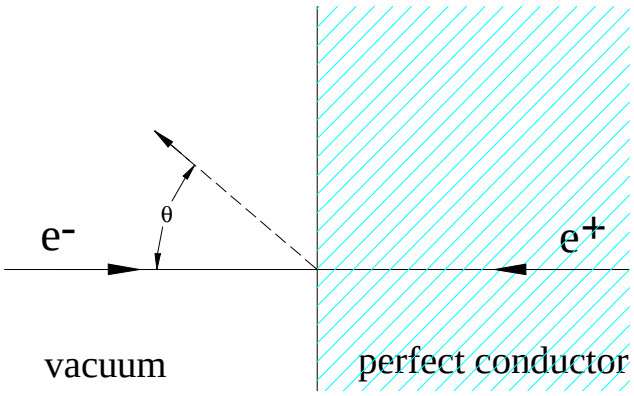

Figure 1.1: Transition radiation emitted when an electron moves from vacuum to metal in a direction normal to the interface. The process can be considered as a two-charged-particle collision problem. The dashed-arrow shows the emitted radiation.

The radiation energy W emitted in the frequency range $\mathrm{d}\omega$ into the solid angle $\mathrm{d}\Omega$ can be obtained from the expression for radiation emission for a sudden change of the charge velocity by [12].

$$\frac{\mathrm{d}W}{\mathrm{d}\Omega \mathrm{d}\omega} = \frac{1}{4\pi^2 c^3}\left[\sum_i q_i \left(\frac{\mathbf{v}_{i,2}\times\mathbf{n}}{1-\mathbf{n}\cdot\boldsymbol{\beta}_{i,2}} - \frac{\mathbf{v}_{i,1}\times\mathbf{n}}{1-\mathbf{n}\cdot\boldsymbol{\beta}_{i,1}}\right)\right]^2, \tag{1.2}$$

where q_i is the charge of i^{th} particle, $\mathbf{v}_{i,1}$ is the velocity before the sudden change,$\mathbf{v}_{i,2}$ is the velocity after the sudden change, $\mathbf{n}$ is the unit vector in the direction of the emitted radiation and $\boldsymbol{\beta} = \mathbf{v}/c$. The "sudden" change in the velocities implies that the collision time (τ), the time in which the velocities change, is satisfying $\tau \ll 2\pi/\omega$, where ω is the frequency of the emitted radiation. The condition is generally satisfied for the frequencies in the far-infrared regime.

With the expression (1.2), the radiation emitted from the two-charged-particle collision can be obtained by considering e charge of an electron moving with velocity $\mathbf{v}$ and $-e$ charge of a positron moving with velocity $-\mathbf{v}$ collide at the boundary. The components $\mathbf{v}_{1,2} = \mathbf{v}_{2,2} = 0$, $\mathbf{v}_{1,1} = \mathbf{v}$ and $\mathbf{v}_{2,1} = -\mathbf{v}$. The energy radiated per unit

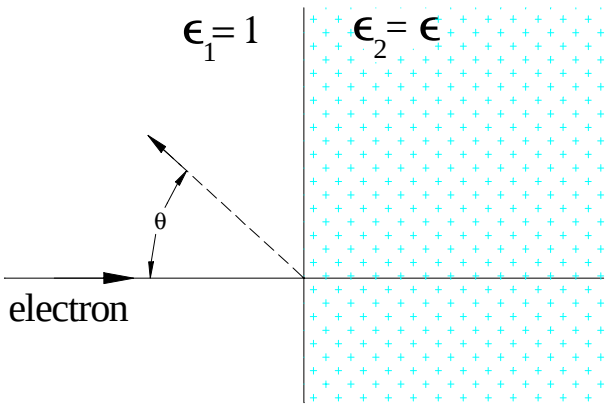

Figure 1.2: Transition radiation emitted from an electron moving through the interface between vacuum and a medium in a direction normal to the interface.

angular frequency per unit solid angle during the collision becomes

$$\frac{\mathrm{d}W}{\mathrm{d}\Omega \mathrm{d}\omega} = \frac{e^2\beta^2 \sin^2\theta}{\pi^2 c(1-\beta^2\cos^2\theta)^2}. \tag{1.3}$$

Here θ is the angle between $-\mathbf{v}$ and the direction $\mathbf{n}$. The radiation is polarized in the radiation plane which is defined as the plane containing the vector $\mathbf{n}$ and the direction normal to the interface. The spectral energy does not depend on the frequency and seems flat for all frequencies. In reality, a conductor can not be treated as perfect at high frequency. The condition $\epsilon \to \infty$ is violated for frequencies close to the plasma frequency of the medium [12].

A more general case is an electron moving across an interface between a vacuum and a finite dielectric constant medium ϵ with normal incidence as shown in Figure 1.2. The angular spectral energy density for the backward transition radiation emitted by an electron is [13]

$$\begin{aligned}\frac{\mathrm{d}W}{\mathrm{d}\Omega \mathrm{d}\omega} &= \frac{e^2\beta^2 \sin^2\theta\cos^2\theta}{\pi^2 c(1-\beta^2\cos^2\theta)^2} \times \\ &\left|\frac{(\epsilon-1)(1-\beta^2+\beta\sqrt{\epsilon-\sin^2\theta})}{(1+\beta\sqrt{\epsilon-\sin^2\theta})(\epsilon\cos\theta+\sqrt{\epsilon-\sin^2\theta}}\right|^2 .\end{aligned} \tag{1.4}$$

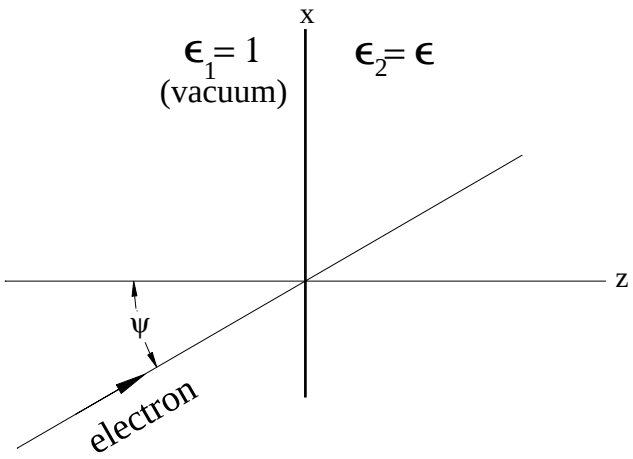

Figure 1.3: An electron moves from vacuum to a medium with a dielectric constant ε at an incident angle ψ with respect to the z axis.

Again, θ is the angle between the direction of emitted radiation $\mathbf{n}$ and $-\mathbf{v}$. The radiation polarization is the same as the case for the previous case. The spectral energy density for the particular case of vacuum-perfect conductor in (1.3) can be recovered by setting ϵ in (1.4) to ∞.

For transition radiation from oblique incidence, we consider an electron moving from vacuum to a medium with a dielectric constant ϵ at an incident angle ψ with respect to the z axis. The schematic diagram for this case is shown in Figure 1.3. Unlike the transition radiation for the case of normal incidence $(\psi = 0)$, in which the emitted electric fields lie in the radiation plane; the radiation, in this case, has an additional component. As a consequence, there may be two polarizations. The first one whose electric field lies in the radiation plane is referred to as the parallel polarization with the index $\|$. The second type whose electric field is perpendicular to the radiation plane is called the perpendicular polarization with the index $\perp$. The derivation of transition radiation for an oblique incidence interface can be found in Ref. [11] and only some results will be shown here.

Radiation intensity for backward transition radiation contributed from the parallel

and perpendicular polarization can be expressed as

$$\frac{\mathrm{d}W}{\mathrm{d}\Omega\mathrm{d}\omega} = \frac{\mathrm{d}W^{\parallel}}{\mathrm{d}\Omega\mathrm{d}\omega} + \frac{\mathrm{d}W^{\perp}}{\mathrm{d}\Omega\mathrm{d}\omega}. \tag{1.5}$$

For a perfectly conducting medium ($\varepsilon \to \infty$), the two components are

$$\frac{\mathrm{d}W^{\parallel}}{\mathrm{d}\Omega\mathrm{d}\omega} = \frac{e^2\beta^2\cos^2\psi}{\pi^2 c}\left[\frac{\sin\theta - \beta\cos\phi\sin\psi}{(1-\beta\sin\theta\cos\phi\sin\psi)^2 - \beta^2\cos^2\theta\cos^2\psi}\right]^2, \tag{1.6}$$

$$\frac{\mathrm{d}W^{\perp}}{\mathrm{d}\Omega\mathrm{d}\omega} = \frac{e^2\beta^2\cos^2\psi}{\pi^2 c}\left[\frac{\beta\cos\theta\sin\phi\sin\psi}{(1-\beta\sin\theta\cos\phi\sin\psi)^2 - \beta^2\cos^2\theta\cos^2\psi}\right]^2. \tag{1.7}$$

For a case of 45° incidence ($\psi = 45°$), which is used extensively in our experimental setup, the two components reduce to

$$\frac{\mathrm{d}W^{\parallel}}{\mathrm{d}\Omega\mathrm{d}\omega} = \frac{e^2\beta^2}{2\pi^2 c}\left[\frac{2\sin\theta - \sqrt{2}\beta\cos\phi}{(\sqrt{2} - \beta\sin\theta\cos\phi)^2 - \beta^2\cos^2\theta}\right]^2 \tag{1.8}$$

$$\frac{\mathrm{d}W^{\perp}}{\mathrm{d}\Omega\mathrm{d}\omega} = \frac{e^2\beta^2}{2\pi^2 c}\left[\frac{\sqrt{2}\beta\cos\theta\sin\phi}{(\sqrt{2} - \beta\sin\theta\cos\phi)^2 - \beta^2\cos^2\theta}\right]^2. \tag{1.9}$$

In these formulas, θ represents the angle between the direction of emitted radiation $\mathbf{n}$ and the $-\mathbf{z}$ axis while ϕ is the azimuthal angle defined in the xy-plane with respect to the $-\mathbf{x}$ axis.

1.2.2 Transition Radiation Properties

In the following sections, some properties of transition radiation emitted from a vacuum-conductor interface will be discussed. In our experiments, we use aluminum as a conducting surface. Since the dielectric constant of aluminum is much more than that of vacuum in the far-infrared regime (see Appendix A), we will use the formulas for a perfect conductor to discuss the transition radiation properties.

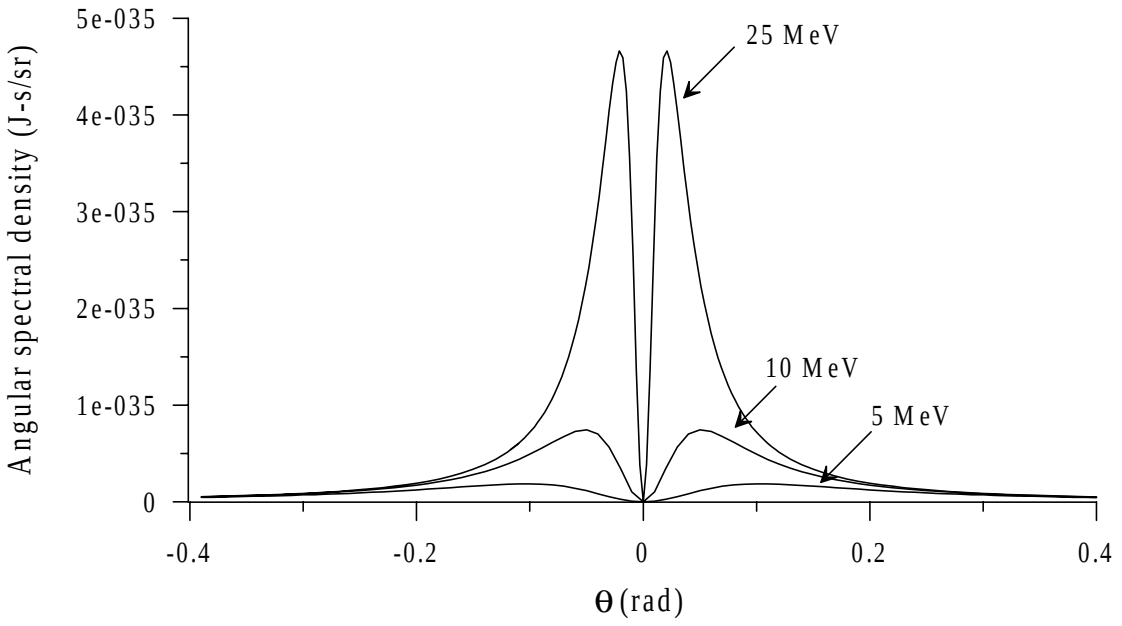

Figure 1.4: Angular distributions of normal incident transition radiation generated by 5 MeV, 10 MeV and 25 MeV electrons.

Angular Distribution

In the case of normal incidence, the angular spectral distribution of the transition radiation can be explained by (1.3). The expression suggests that there is no radiation in the forward direction ($\theta = 0$). The radiation intensity reaches its maximum at $\sin\theta = 1/(\beta\gamma)$, where γ is the Lorentz factor with $\gamma = 1/\sqrt{1-\beta^2}$. At this specific angle, the radiation intensity is $e^2\gamma^2/(4\pi^2 c)$. For relativistic electrons ($\gamma \gg 1$ and $\beta \to 1$), we can approximate $\sin\theta \approx \theta$ and the maximum intensity is therefore located at $\theta \approx \pm 1/\gamma$. The angular distributions of transition radiation generated by various electron energies are shown in Figure 1.4. The distributions show no radiation emitted at $\theta = 0$ and the radiation distribution becomes more collimated for higher electron energies. In case of a 25 MeV electron, the maximum intensity is expected to be at $\theta = \pm 20.4$ mrad, comparing to that of 5 MeV, which has the maximum theoretical intensity at $\theta = \pm 102$ mrad. The radiation angular distribution has no ϕ

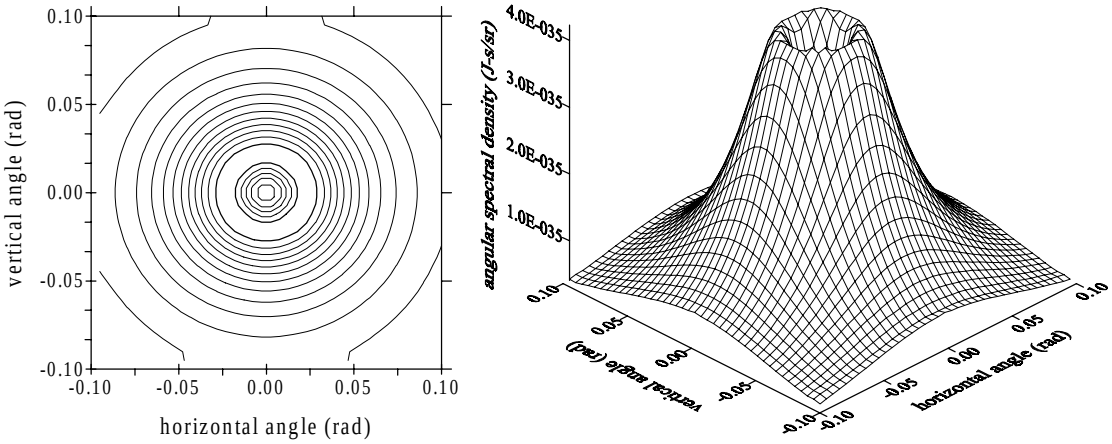

Figure 1.5: Angular distribution of transition radiation for the case of normal incidence.

dependence indicating an azimuthal symmetry of the distribution. Angular distribution of transition radiation for normal incidence is shown in Figure 1.5 displaying an azimuthal symmetry of the distribution.

For the case of oblique incidence, the angular distribution has some azimuthal dependence and thus has an azimuthal asymmetry. Figure 1.6 shows the angular distribution of forward and backward transition radiation generated by a 25 MeV beam from 45°-oblique-incidence. The center of the distribution or the center of the radiation cone is directed along $\mathbf{v}$ for the forward radiation. Unlike the angular distribution for normal incidence which has an azimuthal symmetry, the distribution for 45° incidence is both θ and ϕ dependent. The asymmetry appears only along horizontal angles but not along the vertical ones because the electrons intercept the interface with oblique incidence on the xz-plane; the horizontal angles for forward and backward radiation are defined in the diagram,. The distribution cross sections at the zero horizontal angle and the zero vertical angle are shown in Figure 1.7 for the case of normal incidence and for the forward radiation from 45°-incidence. The solid lines represent the angular distributions for 45°-incidence while the dashed-lines are representing that of normal incidence. It can be clearly seen that only the horizontal cross section of the distribution (along the zero vertical angle) is asymmetric. Even

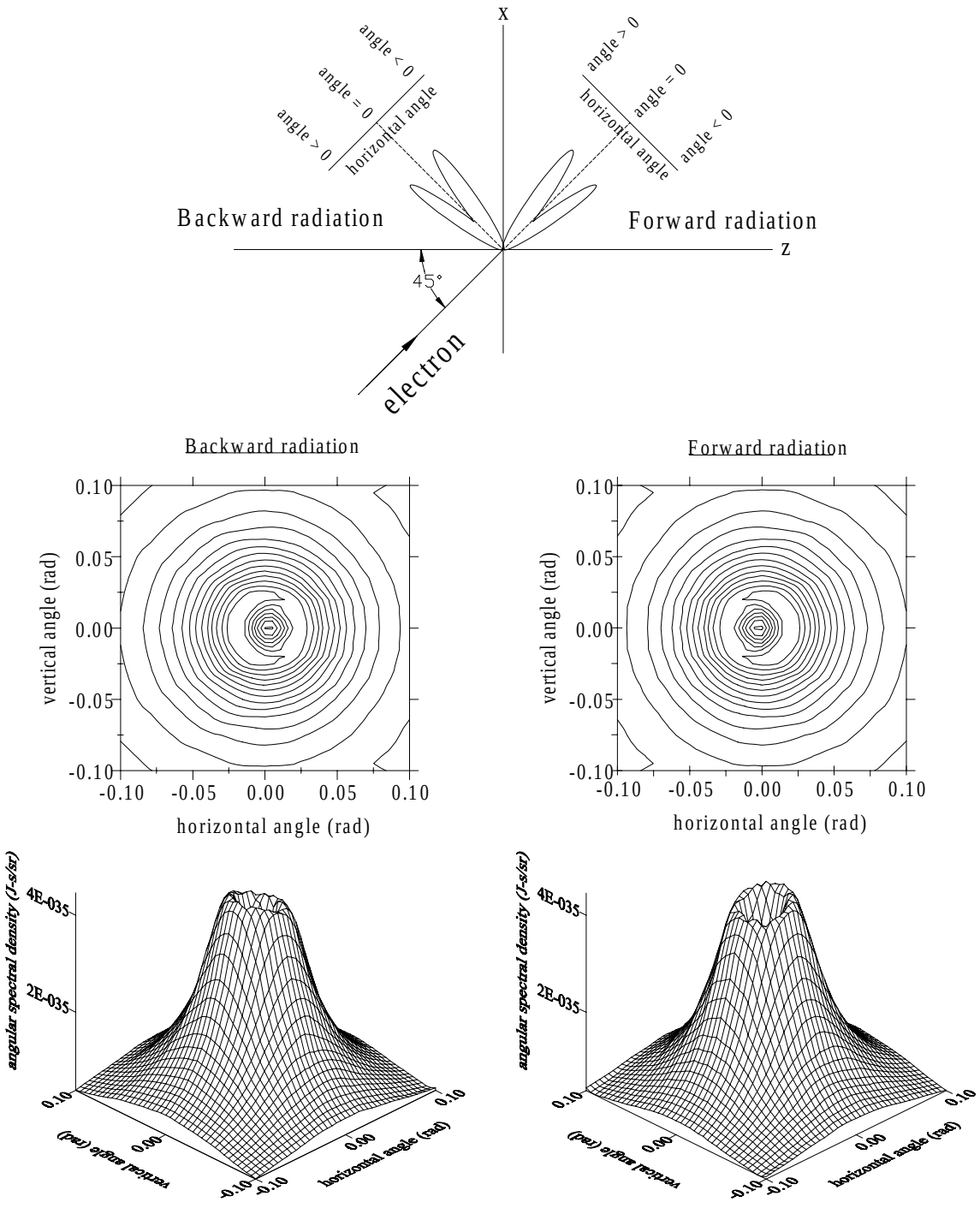

Figure 1.6: Angular distribution of forward and backward transition radiation from 45°-incidence. The diagram on the top shows horizontal angles for the radiation distribution in both directions.

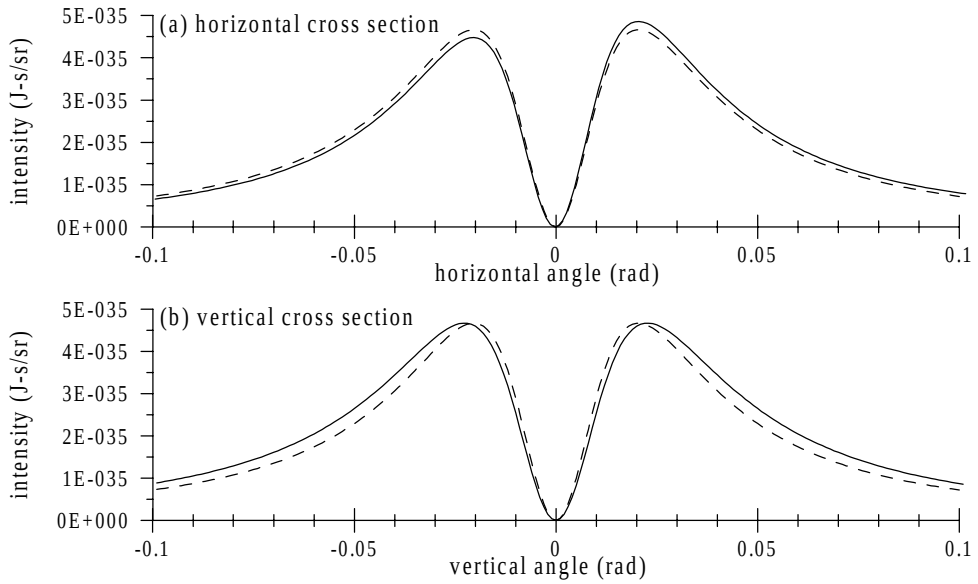

Figure 1.7: Angular distribution cross sections of the transition radiation emitted by a 25 MeV electron for the case of normal incidence (dashed-line) and 45°-incidence (solid).

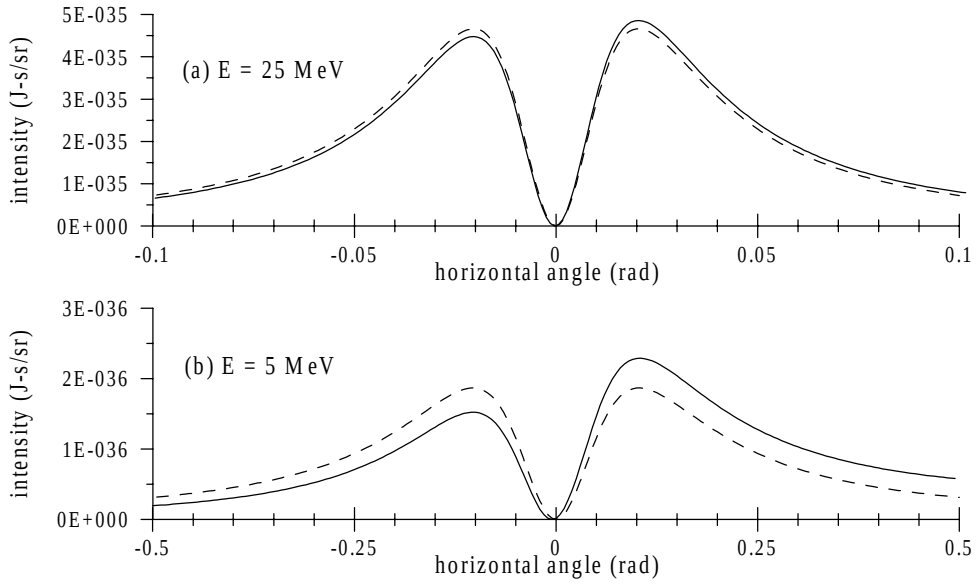

Figure 1.8: Angular distribution along the zero vertical angle of the radiation emitted from a 25 MeV (a) and a 5 MeV (b) electron for the case of normal incidence (dashed-line) and 45°-incidence (solid).

though the vertical cross section (along the zero horizontal angle) is symmetric, it differs from that of normal incidence. The maximum radiation intensity for the case of 45° incidence is located further from the center than the intensity peak for the case of normal incidence. In other words, the intensity is maximum at an angle larger than $1/\gamma$.

The asymmetry in angular distribution, however, vanishes for highly relativistic electrons. The angular distribution becomes closer to that of normal incidence as the electron energy becomes higher. Figure 1.8 shows the angular distribution along the zero vertical angle of the transition radiation emitted from a 25 MeV and 5 MeV electron for normal and 45° incidence displaying a significant asymmetry in the radiation distribution of a low energy beam. As for a 25 MeV beam, the radiation distributions for both cases of incidence are very similar. Therefore, it is reasonable for us to use the radiation distribution for normal incidence which is in a much simpler form to describe the transition radiation distribution in this thesis.

Transition Radiation Collection

Transition radiation has a specific angular distribution which must be taken into consideration when observing the radiation. Generally, the radiation is collected over a certain solid angle. Although the radiation has its maximum intensity around the angle of $1/\gamma$, much of the radiation is emitted at larger angles. The collection of the radiation within an experimental acceptance angle is therefore important By integrating the angular distribution in (1.3) over solid angles to the limit determined by an acceptance angle θ_a, we can obtain the total radiation emitted within the acceptance angle as

$$\begin{aligned}\frac{\mathrm{d}W}{\mathrm{d}\omega}(\theta_a) &= \int_0^{2\pi}\int_0^{\theta_a}\frac{\mathrm{d}W}{\mathrm{d}\Omega\mathrm{d}\omega}\sin\theta\ \mathrm{d}\theta\ \mathrm{d}\phi \\ &= \frac{e^2}{2\pi c}\times \\ &\quad \left[\frac{2(1-\beta^2)\cos\theta_a}{(1-\beta^2\cos^2\theta_a)}+\frac{(1+\beta^2)}{\beta}\ln\left(\frac{(1-\beta\cos\theta_a)(1+\beta)}{(1+\beta\cos\theta_a)(1-\beta)}\right)-2\right]\end{aligned} \tag{1.10}$$

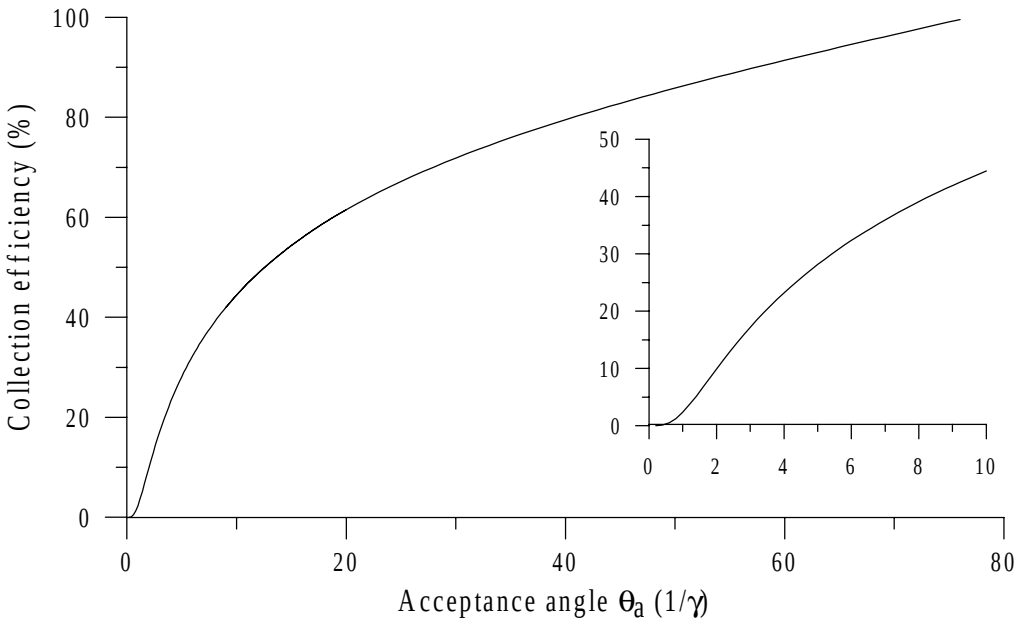

Figure 1.9: Collection efficiency of transition radiation emitted from a 25 MeV electron as a function of acceptance angle.

To get a clear picture of the radiation collection in terms of acceptance angles and electron energy, we consider the collection efficiency which is defined by the ratio of the radiation collected within θ_a to the total radiation. The total radiation is the radiation emitted into the left half space according to Figure 1.1 and Figure 1.2. The integration of radiation energy over the left half space yields

$$\begin{aligned} \frac{\mathrm{d}W}{\mathrm{d}\omega} &= \int_0^{2\pi}\int_0^{\pi/2} \frac{\mathrm{d}W}{\mathrm{d}\Omega \mathrm{d}\omega} \sin\theta \; \mathrm{d}\theta \; \mathrm{d}\phi \\ &= \frac{e^2}{2\pi c}\left[\frac{(1+\beta^2)}{\beta}\ln\left(\frac{1+\beta}{1-\beta}\right) - 2\right]. \end{aligned} \tag{1.11}$$

For high energy electrons with $\gamma \gg 1$ and $\beta \to 1$, the term $(1-\beta)^{-1} \sim 2\gamma^2$. Thus (1.11) also suggests that for high energy electrons the total radiation energy is proportional to $\ln\gamma$.

Collection efficiency as a function of acceptance angle for a 25 MeV electron is shown in Figure 1.9. The acceptance angles are shown in terms of $1/\gamma$ ($1/\gamma = 20.4$

mrad for a 25 MeV electron) with the maximum angle of $\pi/2$ ($\pi/2 \sim 77/\gamma$). The radiation collection efficiency depends greatly on the acceptance angle θ_a which is specified by an experimental setup. Although the maximum intensity of the radiation is located at the angle of $1/\gamma$, the energy contained within this angle is only 2% of the total radiation energy. In our experimental setup, we collect the radiation within acceptance angles of at least $\pm 6/\gamma$. These acceptance angles allow us to collect at least 35% of the total radiation.

Polarization of Transition Radiation

The description of the polarization components was given in Section 1.2.1 for transition radiation from normal and oblique incidence. For the case of normal incidence, the radiation has only one component which is parallel to the radiation plane. Since the radiation for all radiation planes are symmetric about the axis of incidence, the radiation is radially polarized. On the other hand, the transition radiation from oblique incidence has two polarization components, expressed in (1.6) and (1.7) . Equation (1.8) and (1.9) describe the two components of transition radiation generated by an electron with a 45° incident angle at the interface between vacuum and perfect-conductor.

Chapter 2

Coherent FIR Radiation at SUNSHINE

When considering the radiation emitted by a bunch of many electrons, contribution from each electron must be taken into account. The total radiation intensity can be derived by adding all the radiation fields emitted from each single electron with a phase factor determined by its position in the bunch.

At wavelengths shorter than the bunch length, emitted radiation fields from each electron add up incoherently and the total intensity is proportional to the number of electrons in the bunch. On the other hand, emitted radiation fields at wavelengths longer than the bunch length will add up coherently since they are emitted at roughly the same phase. The total intensity in this case is proportional to the number of electrons squared. The coherent enhancement makes the radiation intensity higher than that of an incoherent one by the number of electrons in the bunch. With the typical number of electrons per bunch on the order of $10^8 - 10^9$ electrons, the enhancement is significant and thus becomes of great interest for the development of high intensity radiation sources.

2.1 Coherent Radiation from Electron Bunches

Electromagnetic radiation from an electron bunch can be derived by superimposing the radiation field emitted by each electron in the bunch [14]. Let $\mathbf{r}_j$ be the positional vector from the center of the bunch to the j^{th} electron. The total radiation field from a bunch of N electrons at a frequency of ω is the sum of the field emitted from each electron with a proper phase factor.

$$\begin{aligned} \mathbf{E}_{total}(\omega) &= \sum_{j=1}^{N} \mathbf{E}_j(\omega) e^{i(\omega t - \mathbf{k}_j \cdot \mathbf{r}_j)}. \\ \mathbf{E}_{total}(\omega) &= \sum_{j=1}^{N} \mathbf{E}_j(\omega) e^{i(\omega t - k\mathbf{n}_j \cdot \mathbf{r}_j)}, \end{aligned} \tag{2.1}$$

where $\mathbf{k}_j = k\mathbf{n}_j = (\omega/c)\mathbf{n}_j$ is the wavevector of the j^{th} electron with the direction $\mathbf{n}_j$ to the observer. With a far-field approximation, we then have $\mathbf{n}_j = \mathbf{n}$ and $\mathbf{E}_j(\omega) = E_j(\omega)\mathbf{n}$. The total radiation intensity is proportional to absolute value of the total electric field squared.

$$\begin{aligned} I(\omega) &\propto |\mathbf{E}_{total}(\omega)|^2 \\ &\propto \left| \sum_{j=1}^{N} E_j(\omega) e^{ik\mathbf{n}\cdot\mathbf{r}_j} \right|^2 \\ &= \sum_{j=1}^{N} E_j(\omega) e^{ik\mathbf{n}\cdot\mathbf{r}_j} \sum_{m=1}^{N} E_m^*(\omega) e^{-ik\mathbf{n}\cdot\mathbf{r}_m} \\ &= \sum_{j=1}^{N} |E_j(\omega)|^2 + \sum_{j,m=1,\ j\neq m}^{N} E_j(\omega) E_m^*(\omega) e^{ik\mathbf{n}\cdot(\mathbf{r}_j - \mathbf{r}_m)}. \end{aligned} \tag{2.2}$$

We denote $I_e(\omega)$ as the radiation intensity from one electron at the frequency ω. This $I_e(\omega)$ relates to the emitted field by $I_e(\omega) = |E_e(\omega)|^2$, where $E_e(\omega)$ is the radiation field emitted by one electron. Assuming that all electrons in the bunch have the same energy, we can express the total radiation intensity emitted by the bunch

as

$$I(\omega) = NI_e(\omega) + I_e(\omega) \sum_{j,m=1,\ j\neq m}^{N} e^{ik(\mathbf{r}_j - \mathbf{r}_m)\cdot\mathbf{n}}. \tag{2.3}$$

For wavelengths much longer than the electron bunch length, the phase difference of the emitted fields are very small. The electric fields, therefore, add in phase and the total radiation intensity in (2.3) becomes $I(\omega) = NI_e(\omega) + N(N-1)I_e(\omega) = N^2 I_e(\omega)$. On the other hand, the radiation fields with wavelengths much shorter than the bunch length adds up randomly. The total intensity for this case is then $I(\omega) = NI_e(\omega)$. Between the two limits, the total intensity depends on number of electrons per bunch and positions of each electron with respect to the center of the bunch.

In a continuum limit, we describe the positions of the electrons in the bunch by the bunch distribution. A given bunch distribution $S(\mathbf{r})$ is the probability density for the electrons at the position $\mathbf{r}$ from the bunch center and satisfies $\int S(\mathbf{r})\mathrm{d}^3 r = 1$. The radiation intensity from an electron bunch in term of the bunch distribution is

$$\begin{aligned} I_{total}(\omega) &= \left| \int NE(\omega) e^{ik\mathbf{n}\cdot\mathbf{r}} S(\mathbf{r}) d^3 r \right|^2 \\ &= N^2 I_e(\omega) \left| \int e^{ik\mathbf{n}\cdot\mathbf{r}} S(\mathbf{r}) d^3 r \right|^2 \\ &= N^2 I_e(\omega) f(\omega). \end{aligned} \tag{2.4}$$

The from factor $f(\omega)$ is defined by

$$f(\omega) = \left| \int e^{ik\mathbf{n}\cdot\mathbf{r}} S(\mathbf{r}) d^3 r \right|^2, \tag{2.5}$$

which is the Fourier transform of the normalized bunch distribution squared.

If we use a continuum limit in (2.3), the second term which represents coherent radiation from the bunch becomes

$$I_{coh}(\omega) = I_e(\omega) \int Ne^{ik\mathbf{n}\cdot\mathbf{r}} S(\mathbf{r}) d^3 r \int Ne^{ik\mathbf{n}\cdot\mathbf{r}'} S(\mathbf{r}') d^3 r' \tag{2.6}$$

for $\mathbf{r} \neq \mathbf{r}'$. With a large number of electrons in the bunch, the expression is often written as

$$\begin{aligned} I_{coh}(\omega) &\approx N(N-1)I_e(\omega)\left|\int e^{ik\mathbf{n}\cdot\mathbf{r}}S(\mathbf{r})d^3r\right|^2 \\ &\approx N(N-1)I_e(\omega)f(\omega), \end{aligned} \tag{2.7}$$

with the same definition of $f(\omega)$ as in (2.5). The total radiation following this approach becomes

$$I_{total}(\omega) \approx NI_e(\omega)\left[1+(N-1)f(\omega)\right]. \tag{2.8}$$

Equation (2.8) is often used to show explicitly the enhancement of coherent radiation over incoherent radiation. Both (2.5) and (2.7) are valid as long as there are a large number of electrons in the bunch.

2.1.1 Coherent Enhancement in the Forward Direction

In the forward direction, the form factor in (2.5) can be reduced to

$$f(\omega) = \left|\int e^{ikz}h(z)dz\right|^2, \tag{2.9}$$

where $h(z)$ is the longitudinal distribution of the bunch.

For example, let us consider the form factor for two typical bunch distributions: a uniform and a Gaussian distribution. A uniform distribution, with a width of l, is defined as

$$h(z) = \left\{ \begin{array}{ll} 1/l & \text{, for } |z| \leq l \\ 0 & \text{, otherwise} \end{array} \right\}. \tag{2.10}$$

The from factor for this bunch is

$$f(\omega) = \left[\frac{\sin(\omega l/2c)}{\omega l/2c}\right]^2. \tag{2.11}$$

For a Gaussian bunch with the distribution

$$h(z) = \frac{1}{\sqrt{2\pi}\sigma_z} e^{-z^2/2\sigma_z^2}, \tag{2.12}$$

its form factor is

$$f(\omega) = e^{-(\omega\sigma_z/c)^2}. \tag{2.13}$$

2.1.2 Coherent Enhancement in Arbitrary Direction

If the observation point is not in the forward direction, there is contribution from the bunch transverse distribution and the form factor is evaluated from the three dimensional bunch distribution, $S(\mathbf{r})$. To simplify the problem, we assume $S(\mathbf{r})$ can be expressed as $S(\mathbf{r}) = S_z(\mathbf{z})S_\perp(\mathbf{r}_\perp)$,where $S_z(\mathbf{z})$ is the longitudinal distribution and $S_\perp(\mathbf{r}_\perp)$ is the transverse distribution of the bunch. The longitudinal and transverse positional vectors ($\mathbf{z}$ and $\mathbf{r}_\perp$) relate to the directional vector to the observation point by $\mathbf{n}\cdot\mathbf{z} = z\cos\theta$ and $\mathbf{n}\cdot\mathbf{r}_\perp = r_\perp \sin\theta$, where θ is the angle between $\mathbf{n}$ and the z axis. With these relationships, the form factor in (2.5) becomes

$$f(\omega,\theta) = \left| \int S_\perp e^{ikr_\perp \sin\theta} dr_\perp \int S_z e^{ikz\cos\theta} dz \right|^2. \tag{2.14}$$

In a cylindrical coordinate system, where $S(\mathbf{r}) = S_z(\mathbf{z})S_\perp(\mathbf{r}_\perp) = h(z)g(\rho,\phi)$, we can write the form factor as

$$f(\omega,\theta) = \left| \int_0^{2\pi} \int_0^\infty g(\rho,\phi) e^{ik\rho\cos\phi\sin\theta} \rho d\rho d\phi \int_{-\infty}^\infty h(z) e^{ikz\cos\theta} dz \right|^2, \tag{2.15}$$

where θ is the angle between $\mathbf{n}$ and the z axis and ϕ is the angle between the projection of ρ on the xy-plane and the x axis.

For a bunch with azimuthal symmetry, the transverse distribution is only a function of ρ, therefore $g(\rho,\phi) = g(\rho)$ in this case. Equation (2.15) can now be evaluated

using the identity

$$J_0(u) = \frac{1}{2\pi}\int_0^{2\pi} e^{iu\cos\varphi}d\varphi, \tag{2.16}$$

which is known as the Bessel function of the zero order. The form factor then becomes

$$f(\omega,\theta) = 4\pi^2\left|\int_0^\infty g(\rho)J_0(k\rho\sin\theta)\rho d\rho\int_{-\infty}^{\infty} h(z)e^{ikz\cos\theta}dz\right|^2. \tag{2.17}$$

In case of a cylindrical bunch distribution with a length of l , a radius of a, the transverse distribution defined by

$$g(\rho) = \left\{\begin{array}{ll} 1/a & \text{, for } 0\le\rho\le a \\ 0 & \text{, otherwise} \end{array}\right\}, \tag{2.18}$$

The bunch form factor at a frequency ω and an observation angle θ is

$$f(\omega,\theta) = \left[\frac{2J_1(\omega a\sin\theta/c)}{\omega a\sin\theta/c}\right]^2\left[\frac{\sin(\omega l\cos\theta/2c)}{\omega l\cos\theta/2c}\right]^2, \tag{2.19}$$

where J_1 is the Bessel function of the first order.

For a Gaussian bunch with the transverse distribution

$$g(x,y) = \frac{1}{2\pi\sigma_\rho^2}e^{-(x^2+y^2)/2\sigma_\rho^2} \tag{2.20}$$

and the longitudinal distribution as (2.12) as the one, the bunch form factor is

$$f(\omega) = e^{-(\omega\sigma_\rho\sin\theta/c)^2}e^{-(\omega\sigma_z\cos\theta/c)^2}. \tag{2.21}$$

2.2 FIR Radiation from Short Electron Bunches

At wavelengths longer or comparable to the electron bunch length, the radiation emitted from the bunch is coherent. With a typical number of electrons per bunch on the order of $10^8 - 10^9$, the coherent radiation intensity greatly exceeds that of

incoherent radiation. Especially at long wavelengths compared to the bunch length, the radiation intensity is proportional to the number of electrons in the bunch squared. Therefore, it is possible to generate coherent radiation in the far-infrared spectral range from short electron bunches with bunch lengths of hundreds microns or less. Moreover, the shorter the bunch length, the broader the radiation spectrum that can be generated.

Not only does the spectral distribution of coherent radiation depend on the bunch distribution in terms of the form factor, but it also depends on spectral distribution of the radiation specified by the radiation generation process. For a special case where the radiation spectral distribution itself is not frequency dependent, the coherent radiation spectrum is then determined solely by the bunch distribution. Transition radiation generated at the interface between a vacuum and perfect-conductor happens to be one of these special cases. Although the frequency independence is not completely true for all frequencies of the transition radiation generated at a vacuum-metal interface, it is essentially valid for the transition radiation in the far-infrared regime.

The spectral energy density of incoherent and coherent transition radiation generated from a 25 MeV electron bunch containing 1×10^9 electrons is shown in Figure 2.1. The coherent radiation spectrum is calculated by (2.4) for a Gaussian bunch with $\sigma_z = 50$ μm and for a rectangular bunch with a width of $l = 50$ μm. The coherent radiation intensity for either bunch distribution is nine orders of magnitude higher than that of the incoherent radiation. The coherent radiation spectra from the two bunch distributions are determined by the form factors which are the Fourier transform squared of the bunch distributions.

2.3 The SUNSHINE facility

To generate the far-infrared radiation from electron bunches, the bunch lengths should be of the order of a hundred micron or shorter. At the SUNSHINE facility, electron bunches are generated from an rf-gun with a thermionic cathode. The bunches are

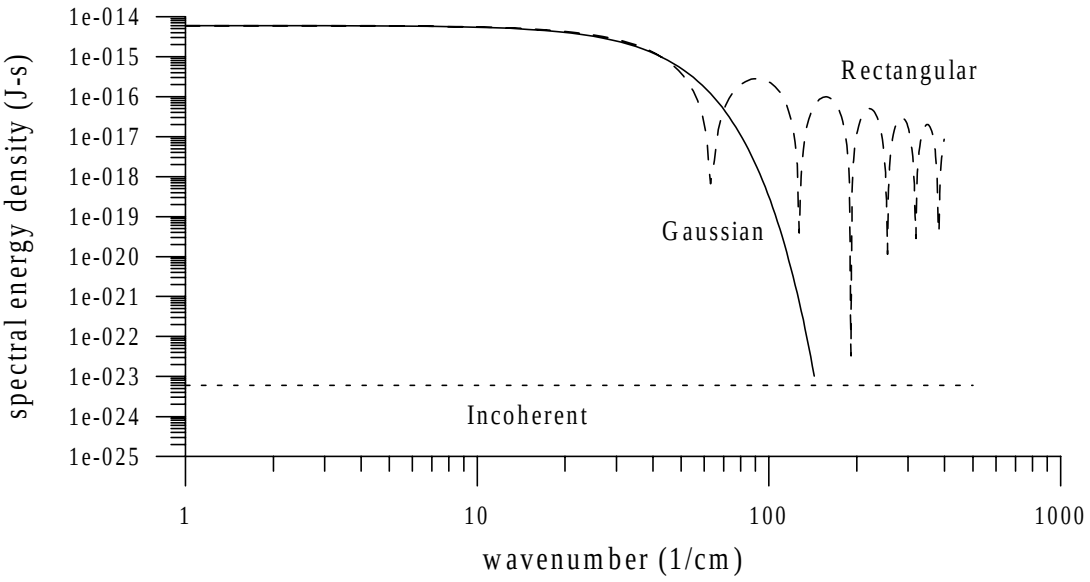

Figure 2.1: Incoherent and coherent transition radiation generated from a 25 MeV beam (— : Gaussian bunch with $\sigma_z = 50$ μm, - - : Rectangular bunch with a width of $l = 50$ μm.).

compressed to less than one picosecond (1 ps $\approx$ 300 μm) by an alpha-magnet, accelerated to some 30 MeV in a S-band linac and guided to the experimental stations. Detailed explanation of the rf-gun and the bunch compression can be found in Refs. [15] and [1]. Reference [1] and [16] also describe the SUNSHINE facility in detail.

2.3.1 Generation of Femtosecond Electron bunches

Our electron source and compression system consist of an rf-gun and a magnetic bunch compressor. The schematic diagram of the system is shown in Figure 2.2. The rf-gun has $1\frac{1}{2}$cavities operating at 2856 MHz with a thermionic cathode attached to one wall of the first half-cell [15], [1]. The fields in both cavities are designed specifically to generate short electron bunches. After electrons are emitted from the cathode, they get accelerated or decelerated from electromagnetic fields depending on cycle of the oscillating fields. The first particle reaches the end of the first half-cell just before the field changes sign so that it gains maximum acceleration. The particles that follow

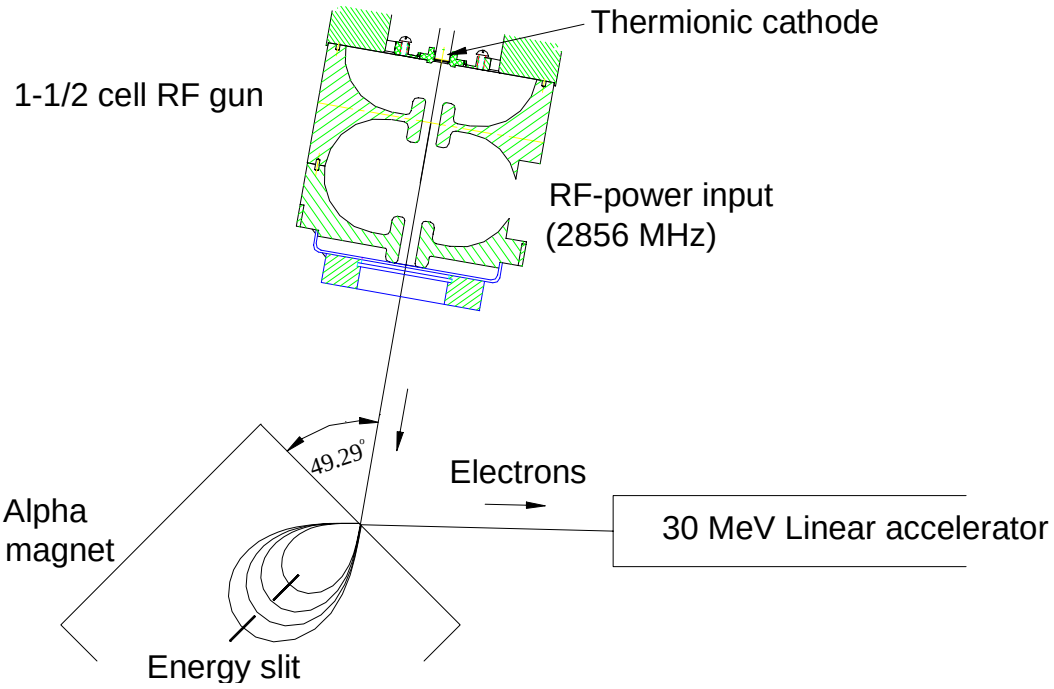

Figure 2.2: Schematic diagram of our electron source and compression system (the rf-gun and the alpha-magnet).

the first one experience some deceleration and have less and less energy.

At the exit of the rf-gun, electrons have been accelerated to about 2.6 MeV with a well-defined correlation between energy and time [Figure 2.3(a)]. Higher energy particles are emitted first, followed by lower energy particles. The electrons are then guided to an alpha-magnet, in which bunches are compressed. The beam enters the alpha-magnet at an angle of 49.29° with respect to the magnet axis, follows an alpha-like path, and exits again at the entrance point with a total deflection angle of 278.58°. In the alpha-magnet, higher energy particles follow longer paths while lower energy particles follow shorter ones. The lower energy particles therefore have a chance to catch up with the higher energy particles in the front, causing the bunch to shorten. By adjusting the alpha-magnet strength, it is possible to compress part of the electron bunch to less than one picosecond. The desired part of the electron bunch is selected by a pair of energy slits located in the alpha-magnet. The bunch is

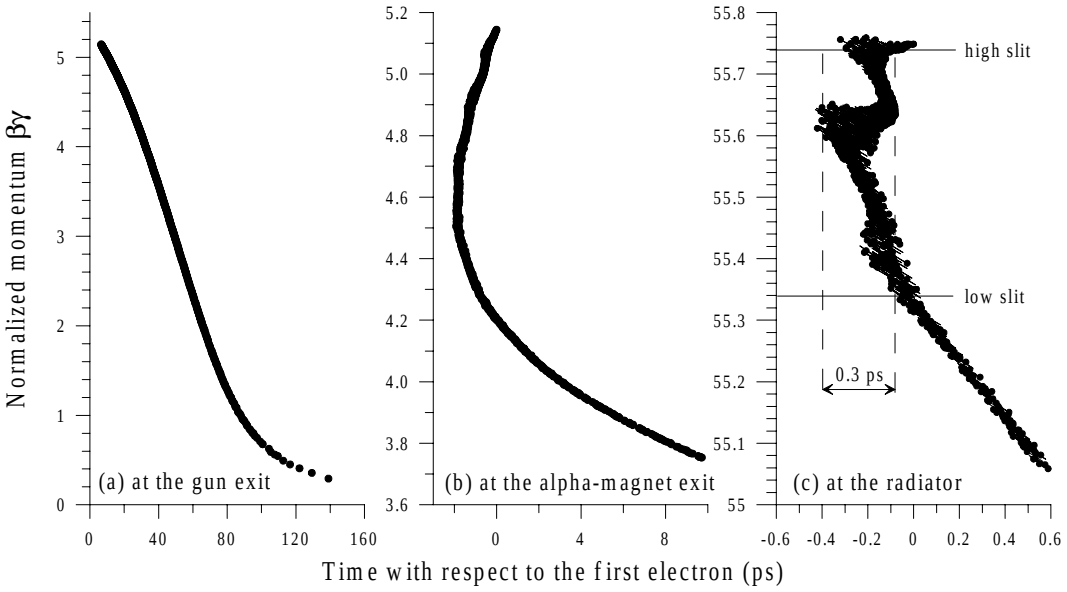

Figure 2.3: The electron momentum-time distribution (a) at the exit of the gun, (b) at the exit of alpha-magnet, and (c) at the radiation point.

then accelerated in a 3-m-single-section S-band linear accelerator and guided to the experimental stations.

Due to some variation in the electron velocities, the bunch spreads as it travels through the beam line. Therefore, it is necessary to overcompress the bunch in order to compensate for this effect. With an overcompression, the bunch length reaches its minimum at the experimental station. The principle of bunch compression is demonstrated in Figure 2.3. At the exit of the gun [Figure 2.3(a)], the highest energy particle is in the front followed by lower and lower energy particles. Bunch compression occurs as the bunch travels within the alpha-magnet. By applying an overcompression, the bunch length has not reached the minimum at the exit of the alpha-magnet. The distribution is shown in Figure 2.3(b) with the highest energy particle having a little lag in time. Further downstream at an experimental station, where the minimum bunch length is desired, part of the electron bunch gathers in less than one picosecond time frame. By selecting only this part of the bunch through the adjustment of the energy slits located in the alpha-magnet, we are able to generate

Parameters	
macropulse length	$\sim 1\ \mu$s
number of bunches	~ 3000 bunches per macropulse
repetition rate	$2 - 30$ Hz
beam energy	$25 - 30$ MeV
number of electrons	$10^8 - 10^9$ electrons per bunch
bunch length (rms)	$100 - 200$ fs

Table 2.1: Typical operating parameters of the electron beam at SUNSHINE.

femtosecond electron bunches. The momentum-time distribution at the radiation point is shown in Figure 2.3(c) displaying, for example, a group of electrons within a certain energy spread which are contained in 300 fs time frame.

2.3.2 The Electron Beam

Table 2.1 shows typical operating parameters of the electron beam at SUNSHINE. In Figure 2.4 a schematic diagram of the macropulse structure is shown. The macropulse is approximately 1 μs long generated at a repetition rate of $2 - 30$ Hz (for most of the work in this thesis, the repetition rate is 10 Hz). Within a macropulse, there is a

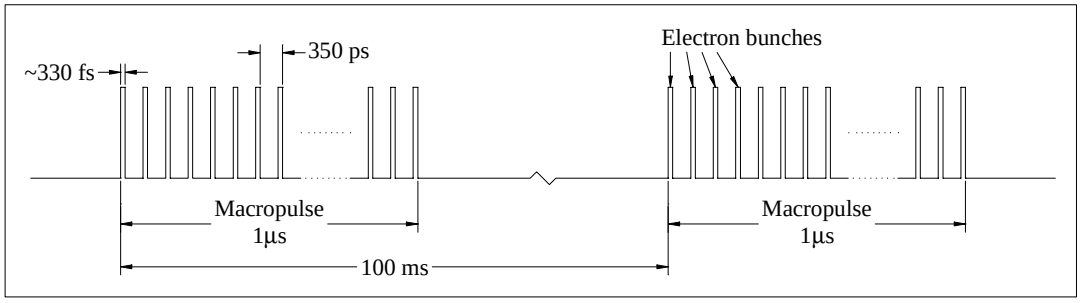

Figure 2.4: A schematic layout of the macropulse containing 3000 electron bunches spaced at 350 ps. At a repetition rate of 10 Hz the macropulses are 100 ms apart.

train of about 3000 electron bunches which are spaced at 350 ps (1/2856 MHz). The length of the bunches is limited by the bunch compression described in the previous section. The highest microbunch peak current of 300 A were reached for the bunch containing 5.3×10^8 electrons and having $\sigma_\tau = 113$ fs.

Chapter 3

Experimental Setup

A schematic diagram of the beam line is displayed in Figure 3.1 showing the rf-gun, the alpha-magnet, the linear accelerator and the experimental stations. There are several experimental stations downstream from the LINAC, including the stations for transition radiation, for diffraction radiation and for stimulated transition radiation. Several stations are set to generate coherent transition radiation from electron bunches both to investigate the coherent radiation characteristics and to characterize the bunch using the coherent transition radiation. This chapter describes the experimental setup and instrumentation in general. Specific features of the setup for each experiment will be described in detail later.

3.1 Beam Instrumentation

The electron beam characteristics determine some properties of the radiation being generated by the beam and thus these parameters become crucial for radiation characterization. This section introduces some of the beam instruments utilized at SUNSHINE including a current monitor, a beam profile monitor, a bunch length measurement system and an energy spectrometer.

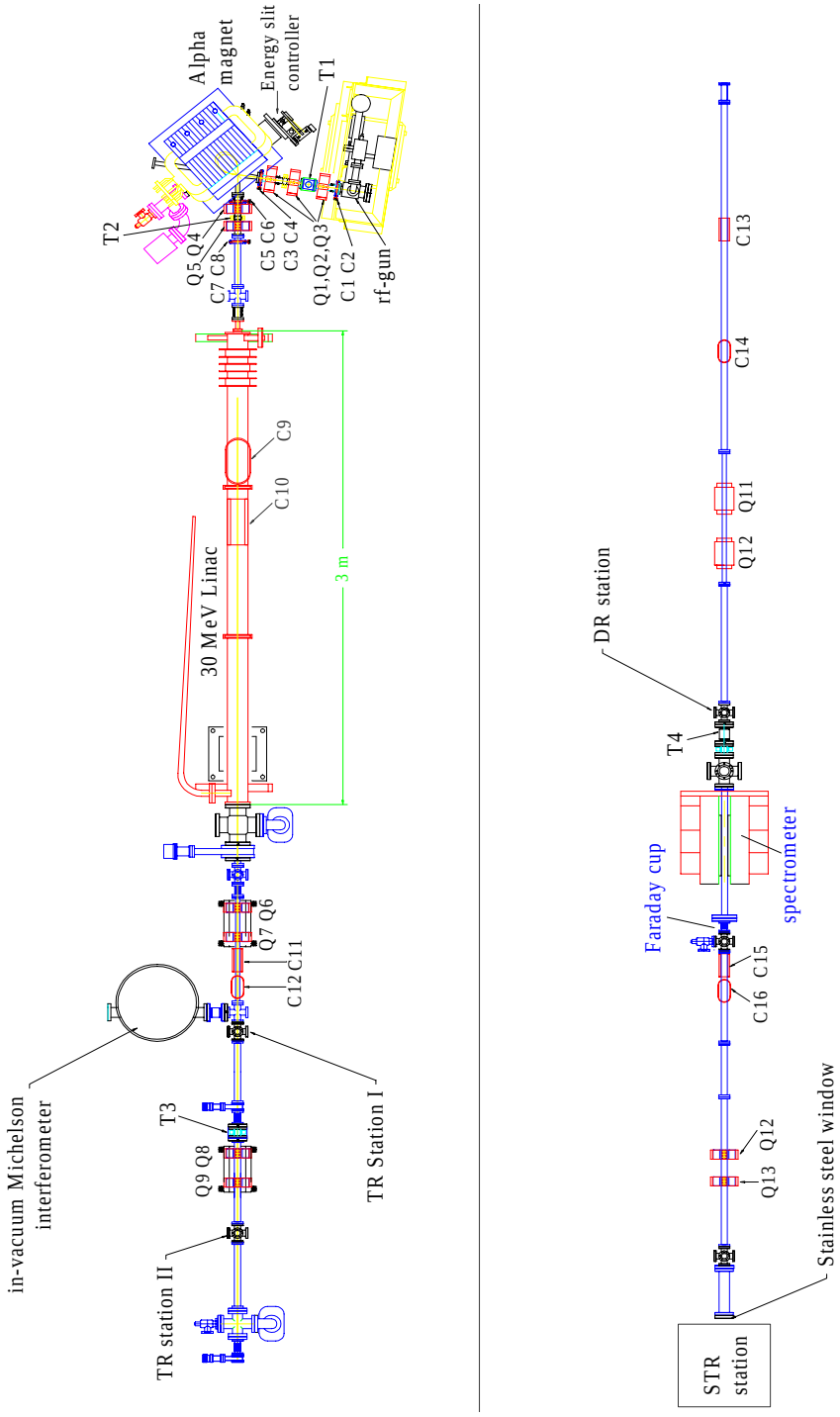

Figure 3.1: Schematic diagram of the beam line.

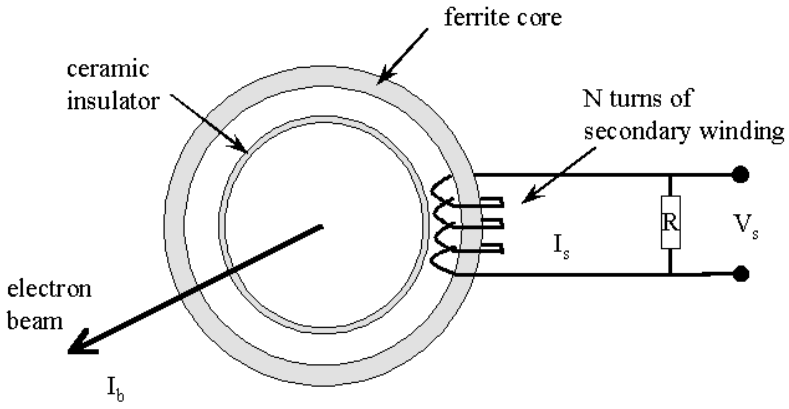

Figure 3.2: Schematic diagram of a current monitor (Toroid).

3.1.1 Current Monitor

The beam current is measured by a current monitor (toroid), which is a pulse transformer with a ferromagnetic core made of ferrite material. A schematic diagram of the current monitor is shown in Figure 3.2. The electron beam acts as a primary winding and the secondary winding of N turns is used to pick up the signal. The toroid is installed around a non-conduction section of the beam pipe to avoid image currents in the vacuum chamber which would cancel the signal from the beam current. The beam current I_b is related to the measured current I_s by $I_b = NI_s$. For convenience, we measure the voltage V_s across a load resistance of $R = 50\Omega$ instead of measuring the current. In most of our toroids, there are $N = 8$ turns in the secondary winding. The beam current is therefore

$$I_b(\mathrm{A}) = 0.16 V_s(\mathrm{V}). \tag{3.1}$$

The toroid does not have the temporal resolution to measure the current of each individual electron bunch, but, it gives a true image of the current pulse for the macropulse as shown in Figure 3.3. Not only does it provide beam current information, but it is also used as a criteria to ensure reproducible electron beam conditions by reproducing the current pulse. There are several toroids installed along the beam

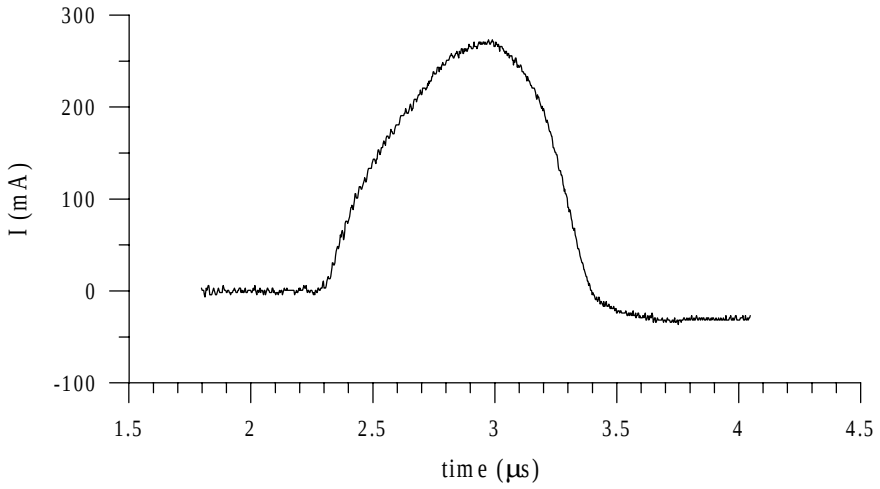

Figure 3.3: A measured current pulse of a macropulse at T3.

line to monitor the beam current at various locations.

3.1.2 Beam Profile Monitor

The transverse beam profile is viewed by projecting the beam on a fluorescent screen which gives off visible photons when irradiated by electron beams. The image is then captured by a CCD camera and observed on a TV monitor. A diagram of the beam profile monitor system is shown in Figure 3.4. A fluorescent screen is mounted on the back of the radiator allowing us to monitor the beam position and get an estimation of the transverse beam size at the locations where the experiments take place. The arrangement of the camera and the screen compensates the aspect ratio of the projected beam profile on tilted screen and therefore the measured beam profiles require no correction. Since the screen is placed very close to the radiator, the scattering of the electron beam through the radiator can be ignored.

For a precise beam profile measurement, the image of the beam is captured with a computer equipped with a frame grabber (DT322 from Data-Translation). Window-based software, compatible with the frame grabber has been developed and used to catch an image of the beam. The software synchronizes the frame grabber to the macropulse cycle to ensure it catches a beam image. The image of the beam can then

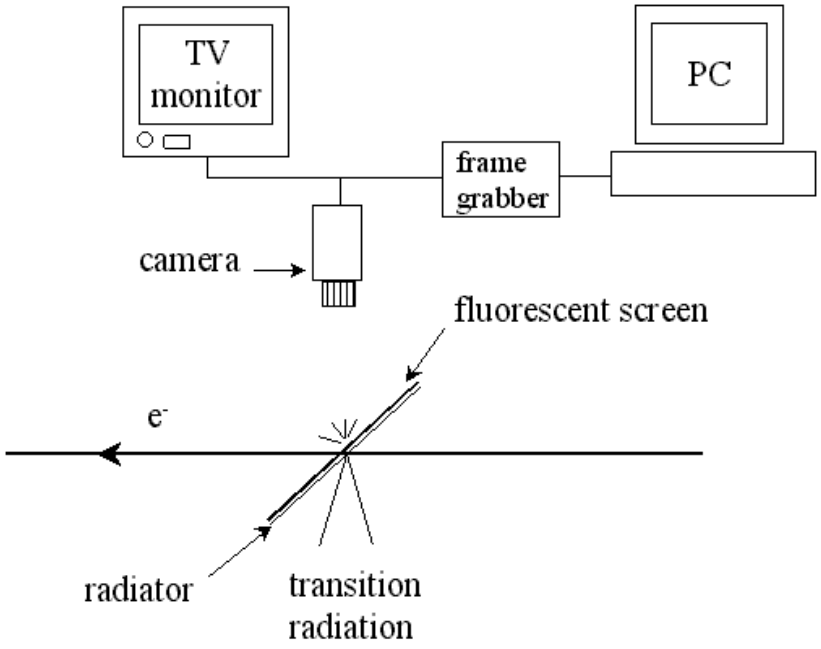

Figure 3.4: A schematic layout of the beam profile monitor system.

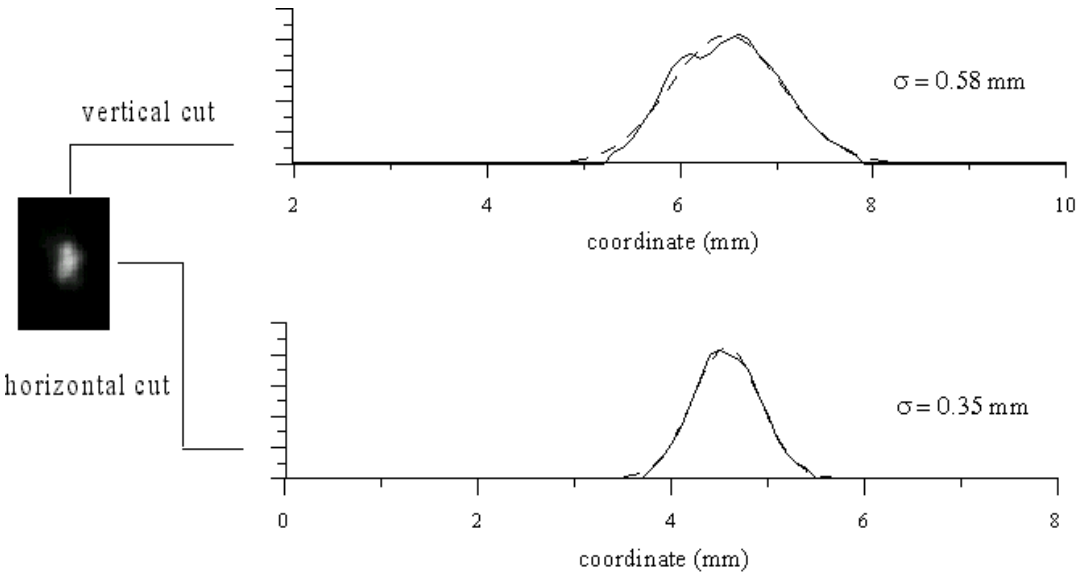

Figure 3.5: A transverse beam profile showing an image of the beam, its horizontal profile, and its vertical profile (— : beam profile and - - : Gaussian fit).

be analyzed to get the transverse beam profile. Figure 3.5 shows an image of the beam with its horizontal and vertical beam profiles. These beam profiles are cross sections through the beam core (the most intense part). Each profile looks more or less like a bell-shape. By fitting the profile to a Gaussian, we can obtain the standard beam sizes (σ_x, σ_y). In Figure 3.5, the Gaussian fits are shown by dashed-lines. It has been found that, in most of the cases, we have oblong beam cross sections with a larger height than width $(\sigma_y > \sigma_x)$. The effective beam radius σ_ρ is then somewhat between σ_y and the arithmetic average of both half axes $\frac{1}{2}(\sigma_x + \sigma_y)$.

3.1.3 Bunch Length Measurement System

The bunch length measurement system is one of the main topics presented in this thesis and will be discussed in details in Chapter 5. The system will be briefly introduced here to complete the beam instrumentation.

We measure the bunch length using an autocorrelation of the coherent transition radiation. This technique extracts the bunch length information from the spectrum of coherent transition radiation generated by the electron bunch. The radiation spectrum is obtained by a Michelson interferometer which will be described later in this chapter. This bunch length measurement technique is capable of resolving bunch lengths well below one picosecond.

3.1.4 Energy Spectrometer

In a bending magnet, electrons with different energy will follow different trajectories because the bending angle is associated with the beam energy. Therefore, the energy distribution can be measured by bending the beam and observing the beam current as a function of bending angle. It is, however, more convenient to monitor the collected beam current at a fixed bending angle and obtain the energy distribution by varying the magnetic field.

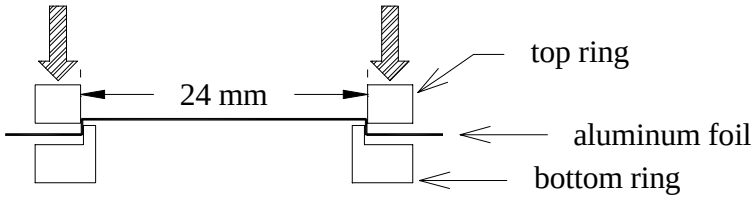

Figure 3.6: Cross-sectional diagram of a radiator for transition radiation.

3.2 Setup to Generate Transition Radiation

At SUNSHINE, we generate transition radiation by inserting a radiator in the beam path. The radiator is made of a stretched 25-μm-thick aluminum foil supported by two aluminum rings using the drumhead stretching principle. The transition radiation is then generated at the vacuum and Al-foil interface. The diagram in Figure 3.6 displays a cross-sectional diagram of the radiator showing the top and the bottom supporting rings. The aluminum foil is placed between the two rings and can be stretched over the edge of the bottom ring. The inner diameter of the supporting ring which represents the size of the conducting surface is 24 mm.

As described in Chapter 1, the spectral intensity of transition radiation is determined by the dielectric constant of the two mediums. Since this thesis is focused on the far-infrared transition radiation generated from the interface between a vacuum ($\epsilon = 1$) and Al- foil, the dielectric constant of aluminum in this regime should be considered. Using Drude's model, the dielectric constant of aluminum ϵ_{AL} in the far-infrared spectral range is calculated and is presented in Appendix A. Its value, in this spectral regime, is higher than $\epsilon_{AL} = 1 \times 10^5$. We may, therefore, assume that $\epsilon_{AL} \gg 1$ in the far-infrared regime, and will treat the Al-foil radiator as a perfect conducting surface ($\epsilon \to \infty$).

By tilting the radiator by 45° with respect to the electron path, the backward transition radiation is emitted at 90° with respect to the beam axis and exits through a high density polyethylene (HDPE) window. According to the data sheet [17] and

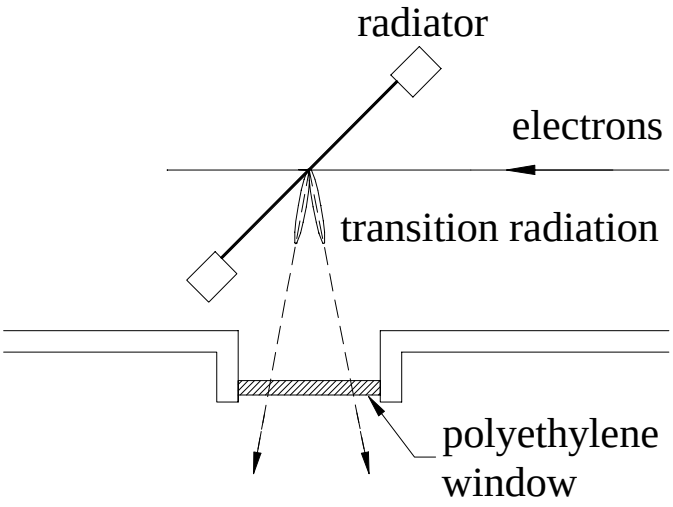

Figure 3.7: A schematic diagram of the setup for generating backward transition radiation.

Ref. [18], the high density polyethylene window transmits most of the radiation in the far-infrared range. A schematic diagram of the setup to generate transition radiation is shown in Figure 3.7. The thickness and the size of the window are different in some experimental setups and will be mentioned specifically for each experiment.

In a setup, collection of the transition radiation is limited by the acceptance angle which may differ in each experimental setup depending on the component configuration. Mostly, the acceptance angle is determined by the size of the polyethylene window and the distance from the radiator to the window. The smallest acceptance angle in our experiments is ± 120 mrad in a setup using a small window (18 mm diameter) and the window is 74 mm away from the radiator. This small acceptance angle is close to $\pm 6/\gamma$ and has a radiation collection efficiency of 33% for a 25 MeV electron beam. The acceptance angle for each experiment setup will be specified where appropriate.

A transition radiation experimental station is usually located after a quadrupole doublet focusing system. This focusing is necessary to minimize the beam spot size at the radiator. The effects of the beam sizes on the radiation properties will be discussed in Chapter 4.

3.3 Pyroelectric Detector

We use a room temperature pyroelectric detector to measure the far-infrared radiation intensity. The detector can be separated into two parts; the pyroelectric sensor and the amplifier. The pyroelectric sensor is manufactured by Molectron (Molectron P1-65). The sensor consists of a 100 μm thick $LiTaO_3$ pyroelectric crystal and a built-in impedance transformer [a field effect transistor (FET) and a resistor] which control the overall electrical time constant of the sensor. When a pyroelectric crystal is exposed to incident radiation, radiation absorption causes the temperature of the element to rise. As a result, the crystal expands and generates a polarization current. The polarization current is then neutralized through an external circuit by electrodes attached to the front and back surfaces of the sensor. The output signal from the sensor is therefore proportional to the change of the crystal temperature which is determined by the incident radiation energy [19]. The Signal from the pyroelectric sensor is amplified by a signal amplifier [3] with an adjustable gain of 1 to 200. The time response of the detector is not fast enough to measure the radiation energy from each microbunch. The signal from the detector is, therefore, proportional to the total radiation per macropulse (3000 microbunches). The detector has been calibrated against a Scientech thermopile power meter. There are three pyroelectric detectors used in the measurements and the three detectors have slightly different voltage-to-power conversion. Results of some measurements will be presented in term of power where appropriate, otherwise we will present relative power in term of the measured voltage.

According to the Molectron data sheet [19], the detector has a uniform spectral response from a few μm to some 100 μm wavelength. However, in our experiments we found that multiple reflections inside the crystal cause some interferences and result in a periodic modulation of the detector spectral response. The effects of these multiple reflections will be described in detail in Chapter 5.

3.4 Translation Stage and Controller

Translation stages and controllers are used to move components such as the movable mirror in a Michelson interferometer, mirrors to adjust the cavity length in the stimulated transition radiation cavity, or a detector. A precision-ball-bearing translation stage (Newport Model 443) is moved by either a Newport 850B or a Newport 850F linear actuator. The system is capable of moving in precise steps as small as 0.1 μm. The actuators are controlled by a Newport PMC2000-P motion controller connected to a PC through a GPIB interface. Through the interface the actuator can be controlled by a computer program written in the LABVIEW environment which can move the actuator in steps or in continuous motion.

3.5 Michelson Interferometer

A Michelson interferometer, sometimes refered to as a two beam interferometer, is used to analyze the radiation spectral distribution. The interferometer is also part of the bunch length measurement system and will also be used for far-infrared spectroscopy. In this section, we will describe the general characteristics of a far-infrared Michelson interferometer. Details will be provided with specific remarks when discussing the bunch length measurement in Chapter 5 and far-infrared spectroscopy in Chapter 8.

A schematic diagram of a far-infrared Michelson interferometer is shown in Figure 3.8. The interferometer consists of a beam splitter, a fixed mirror and a movable mirror, arranging as the diagram shown. Radiation entering the Michelson interferometer is split into two parts by the beam splitter. The two parts then travel in two different directions to be reflected back by mirrors. After reflection, the two radiation pulses are combined again and sent to a detector for measuring the intensity.

At an optical path difference of δ, the combined radiation pulses are the radiation pulse from the fixed arm, $E_{fix}(t) = TRE\,(t)$; and the radiation from the movable arm delayed in time by δ/c, $E_{move}(t) = RTE\,(t + \delta/c)$. Here R and T are the reflection and transmission coefficients of the beam splitter. The intensity measured at the

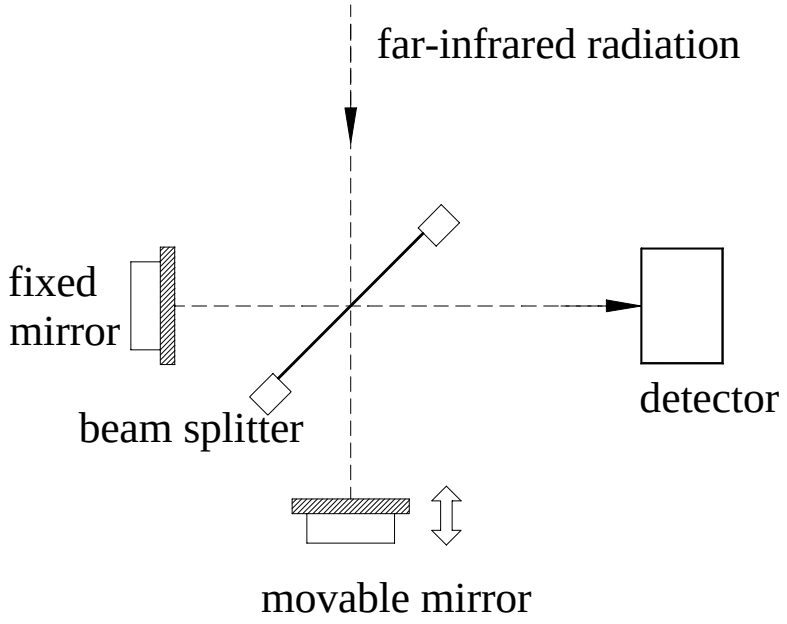

Figure 3.8: A schematic diagram of a Michelson interferometer.

detector is then

$$\begin{aligned} S_D(\delta) &\propto \int \left| TRE(t) + RTE(t + \frac{\delta}{c}) \right|^2 \mathrm{d}t \\ &= 2 \int |RT|^2 \, E(t) E^*(t + \frac{\delta}{c}) \mathrm{d}t + 2 \int |RTE(t)|^2 \, \mathrm{d}t. \end{aligned} \tag{3.2}$$

The second term is independent of the path difference and will determine the baseline whose intensity is half of the maximum intensity when $\delta = 0$. The first term is an autocorrelation of the radiation pulse [20]. We call the variation of the radiation intensity above the base line as a function of path difference *an interferogram*. An interferogram is, therefore, just a representation of the radiation autocorrelation.

$$I(\delta) \propto 2 \, \mathrm{Re} \int |RT|^2 \, E(t) E^*(t + \frac{\delta}{c}) \mathrm{d}t. \tag{3.3}$$

The interferogram can be expressed in frequency domain by a Fourier transformation

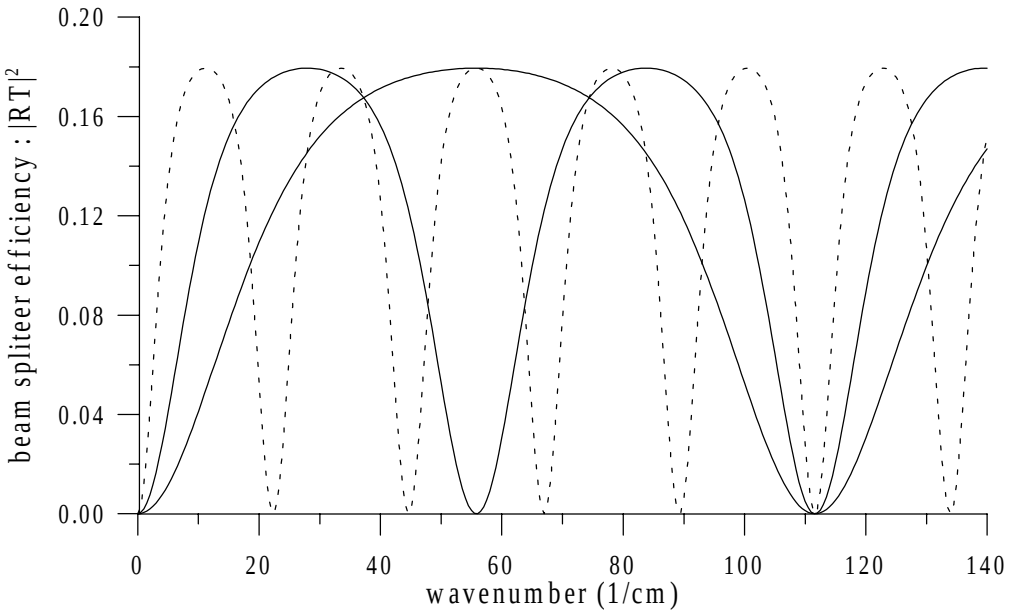

Figure 3.9: Beam splitter efficiency ($|\mathrm{RT}|^2$) of a Kapton beam splitter for various thicknesses (— : 25.4 μm, - - : 50.8 μm, and $\cdots$: 127 μm).

as

$$I(\delta) = 2\,\mathrm{Re}\int_{-\infty}^{+\infty} \left|R(\omega)T(\omega)\tilde{E}(\omega)\right|^2 e^{-i\omega\delta/c}\mathrm{d}\omega. \tag{3.4}$$

From (3.4), the radiation power spectrum is then the Fourier transform of the interferogram.

$$\left|R(\omega)T(\omega)\tilde{E}(\omega)\right|^2 \propto \int_{-\infty}^{+\infty} I(\delta)e^{i\omega\delta/c}\mathrm{d}\delta = \ \mathrm{FT}\left\{I\left(\delta\right)\right\}. \tag{3.5}$$

In a far-infrared Michelson interferometer, a thin film beam splitter is commonly used. Thin film beam splitters have a strong frequency dependence due to interferences of multiple reflections. The total amplitude reflection and transmission (R and

T) of a beam splitter with refractive index n and a thickness of d are [9]

$$R(\omega) = -r\frac{1-e^{i\varphi}}{1-r^2e^{i\varphi}}, \tag{3.6}$$

$$T(\omega) = (1-r^2)\frac{e^{i\varphi/2}}{1-r^2e^{i\varphi}}, \tag{3.7}$$

where $\varphi = (2\omega d/c)\sqrt{n^2-1/2}$ for a 45° incident angle and r is the amplitude reflection coefficient at the air-beam splitter interface which is different for parallel and perpendicular polarization components. With an incident angle of 45° and assuming the refractive index $n_{air} \approx 1$ for air, the two components of r are [21]

$$r_\perp = \frac{1-\sqrt{2n^2-1}}{1+\sqrt{2n^2-1}}, \tag{3.8}$$

$$r_\parallel = \frac{n^2-\sqrt{2n^2-1}}{n^2+\sqrt{2n^2-1}}. \tag{3.9}$$

The beam splitter efficiency is defined as $|R(\omega)T(\omega)|^2$ and it has a specific frequency dependence depending on the thicknesses and refractive index of the beam splitters. The efficiency for some typical thicknesses of Kapton beam splitters, which are used in our measurements, is shown in Figure 3.9. The efficiency becomes zero at certain frequencies, where destructive interferences occur. The thickness of the beam splitter is usually chosen so that the frequencies of interest stay between the first two minima. A Michelson interferometer for the bunch length measurement, however, has different criteria for choosing a beam splitter. The beam splitter effects on the bunch length measurement will be discussed in Chapter 5.

To show the effects of the beam splitter interference on an interferogram and on the spectrum, we compute the interferogram of a Gaussian pulse with and without the beam splitter response. Figure 3.10 shows the interferogram and the spectrum if an ideal beam splitter is used. Figure 3.11 shows the interferogram and the spectrum obtained from the same Gaussian pulse with the beam splitter interference. In the calculation, the parameters for a 25.4-μm-thick Kapton beam splitter have been used. Suppression of frequencies where the beam splitter efficiency becomes zero are

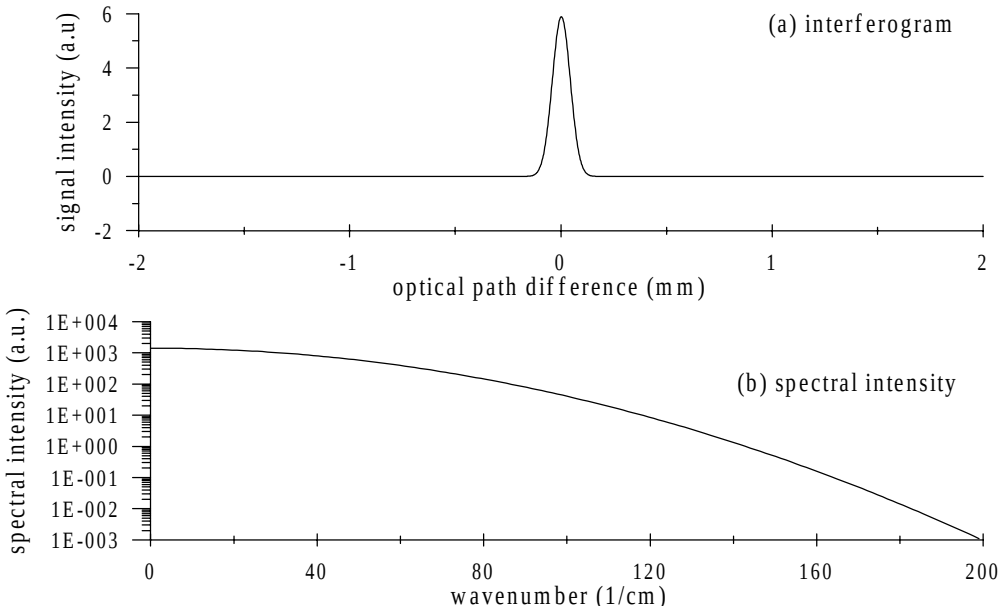

Figure 3.10: An ideal (a) interferogram and (b) spectrum of a Gaussian pulse with a $\sigma_z = 30$ μm.

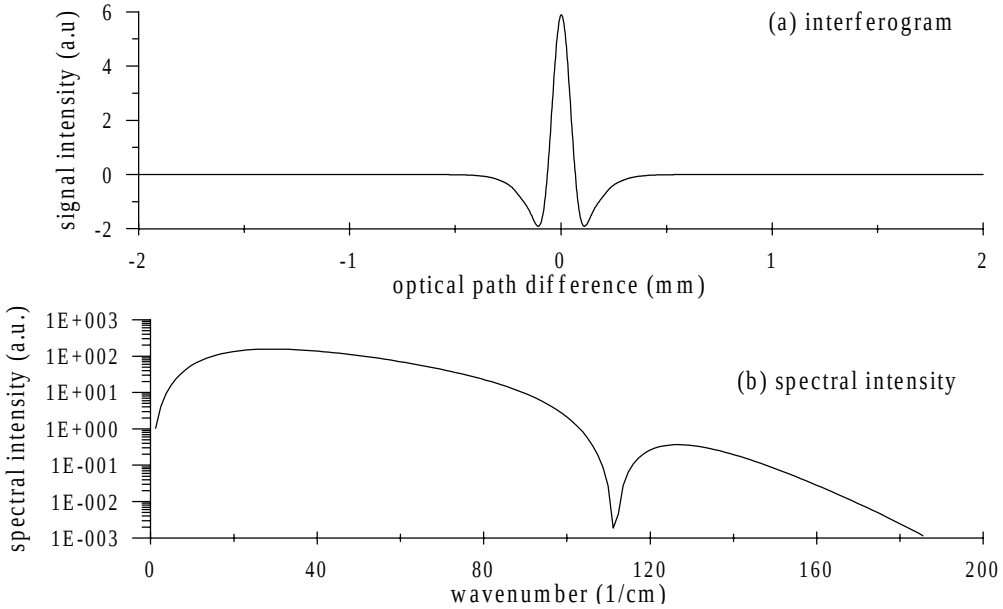

Figure 3.11: Interference effects of a 25.4-μm-thick Kapton beam splitter on (a) the interferogram and on (b) its spectrum for a Gaussian pulse with a $\sigma_z = 30$ μm.

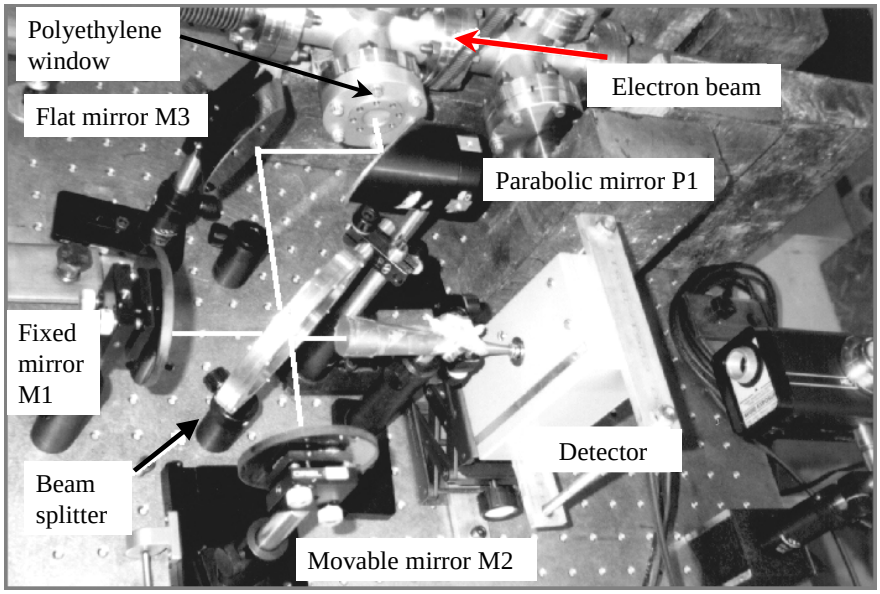

Figure 3.12: The Michelson interferometer setup with the white trace representing the radiation path.

evident. In the interferogram, the beam splitter interference causes negative valleys near the main peak. The beam splitter efficiency must be considered when using the information obtained from the Michelson interferometer.

Figure 3.12 shows the setup of a Michelson interferometer including part of the beam line with the polyethylene window. The main components of the Michelson interferometer; a fixed mirror, a movable mirror, a beam splitter, and a detector are shown in the Figure. The fixed mirror M1 and the movable mirror M2 are Al-coated front surface mirrors. We use an Al-coated parabolic mirror P1 to convert divergent radiation in to a parallel beam. The collimated and parallel beam is then deflected 90° by a flat mirror M3 into the beam splitter. The recombined radiation from the beam splitter is collected with a copper cone and is directed to a pyroelectric detector. The movable mirror is mounted on a translation stage and the movement is control through a PC as described in 3.5. An interferogram is obtained by moving the movable mirror in steps while recording the radiation intensity from the detector.

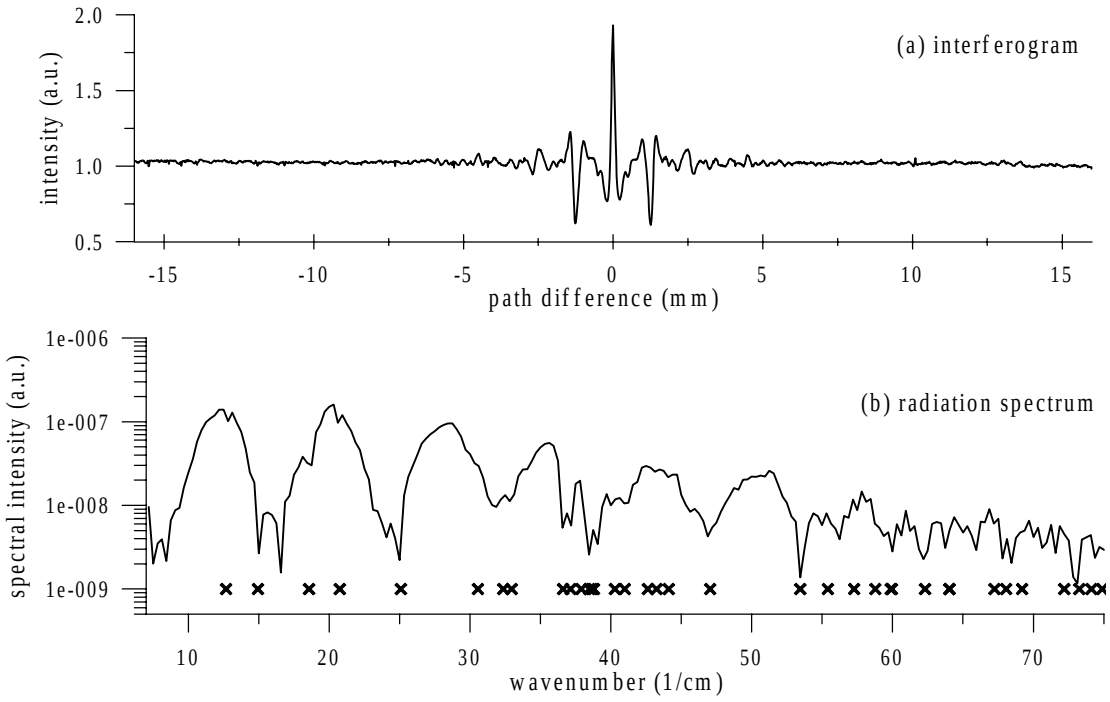

Figure 3.13: (a) interferogram and (b) radiation spectrum obtained from the Michelson interferometer set up in ambient air.

The mirror scan and the detector signals are controlled and recorded through the computer interface with LABVIEW environment.

Figure 3.13 presents an interferogram and its spectrum obtained from the Michelson interferometer setup in ambient air (the setup is shown Figure 3.12). The valleys resulted from the beam splitter interferences are apparent in the interferogram. The two signatures on both sides of the main peak are a detector artifact. This artifact results in a periodic modulation in the spectrum and will be discussed in Chapter 5 in more detail. Many water absorption lines are also visible in the spectrum. The cross marks in the graph indicate the locations where strong water absorption lines are expected. Water absorption appears in the interferogram as small oscillations at the absorption frequencies along the baseline of the interferogram.

3.6 In-vacuum Michelson Interferometer

An in-vacuum Michelson interferometer was assembled for experiments in evacuated environments. The evacuated environment will allow us to separate the effect of water absorption from others in the measurements. The interferometer is set up in a vacuum chamber which is connected to the main beam line. Figure 3.14 shows a side-view schematic diagram of the setup. In the diagram, the electron beam is moving in the direction toward the paper generating backward transition radiation in a downward direction. A gold coated off-axis parabolic mirror P1 which has a diameter of 25 mm and a focal length of 75 mm is used to collimate backward transition radiation generated by the electron beam. The mirror P1 is placed exactly one focal length below the radiator and its focal point aligns at the center of the radiator. Such an arrangement has a radiation acceptance angle of 160 mrad. The collimated and parallel beam then travels through a high density polyethylene window and enters the in-vacuum Michelson interferometer. The window separates the high vacuum system of the beam line from the vacuum system of the interferometer. Figure 3.15 shows a top-view diagram of the setup including the Michelson interferometer inside the vacuum chamber. In this setup, a gold coated off-axis parabolic mirror P2 is used to collect the radiation into the detector. The mirror P2 has a diameter of 25 mm and a focal length of 50 mm. A picture of the in-vacuum Michelson interferometer is displayed in Figure 3.16 showing its components as specified in the schematic diagrams and a translation stage with an actuator to move the movable mirror.

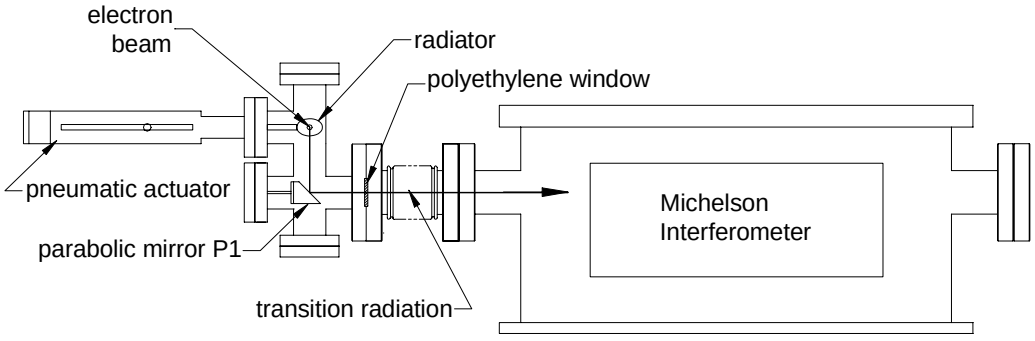

Figure 3.14: A side-view schematic diagram of the in-vacuum Michelson interferometer setup.

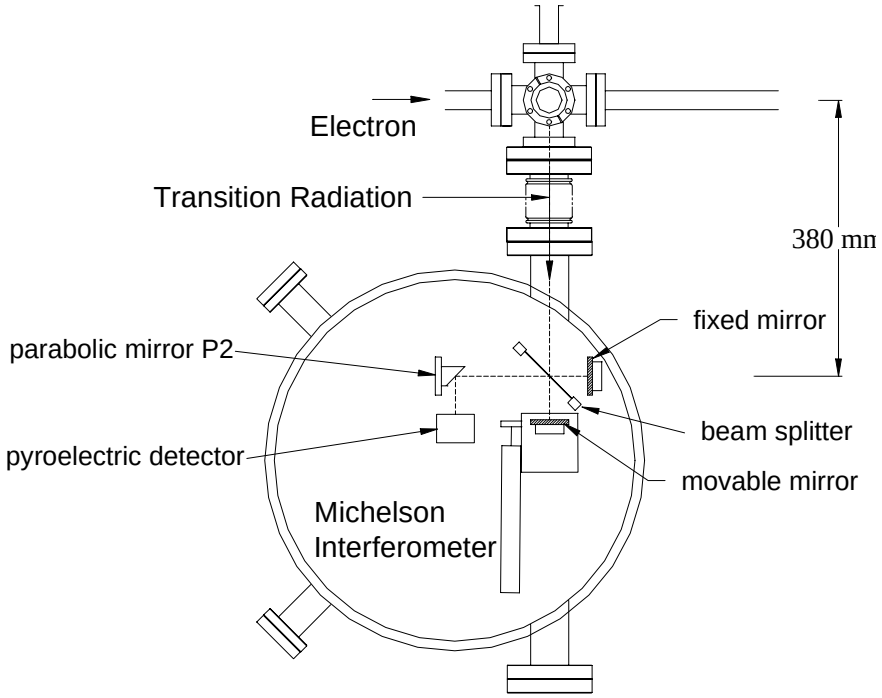

Figure 3.15: A top-view schematic diagram of the in-vacuum Michelson interferometer setup showing components of the interferometer.

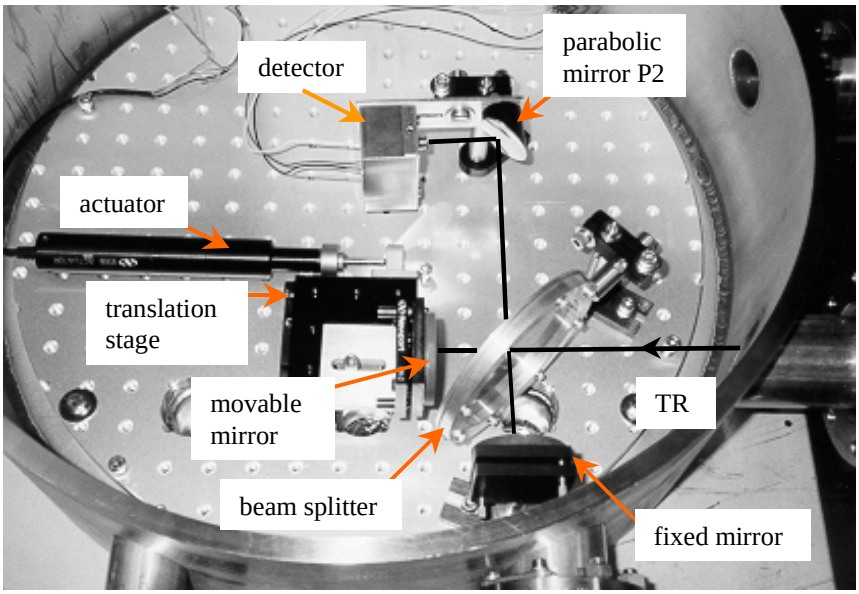

Figure 3.16: A picture of the in-vacuum Michelson interferometer showing its components inside the vacuum chamber.

Chapter 4

Characterization of Coherent TR

This chapter provides the characterization of coherent transition radiation (TR) at SUNSHINE. First, the coherent radiation intensity is illustrated, and then the measured properties of the radiation such as spatial distribution, spectral distribution and polarization are discussed. The electron beam size effects will be discussed later in this chapter.

4.1 Coherent Radiation Intensity

A signature of coherent radiation from short electron bunches is that its intensity scales with the number of electrons in the bunch squared. Measurements of the coherent transition intensity generated from our electron bunches as a function of the number of electrons per bunch have been conducted to verify this quadratic dependence. The radiation intensity is recorded as a function of the electron beam current which is directly proportional to the number of electrons in the bunches. It was found that the most practical way to adjust the beam current at SUNSHINE with the least effect on the electron bunch length is to scrape the beam in the alpha-magnet with the high energy filter while keeping the low energy filter fixed [3].

The beam current is measured with the current pulse monitor T3 (toroid3), located close to the transition radiation radiator. The measured current pulse of a macropulse allows us to estimate the number of electrons in each microbunch. Due to temporal

resolution limitation of the current monitor, we do not know the intensity of each individual microbunch. On the other hand, we have no reason to assume that the intensity changes dramatically from bunch to bunch. The current pulse is therefore a good measurement of the bunch intensity for the duration of the macropulse. To include the temporal variation of the microbunch intensity, a recorded current pulse is sliced into about 400 slices in time and the sum of number of electrons in each slice squared is then calculated. The sum of number of electrons in each microbunch squared

$$\sum_{i=1}^{N_b} N_{ei}^2 \approx \left(\frac{N_b}{N_{slice}}\right) \sum_{j=1}^{N_{slice}} N_{ej}^2, \tag{4.1}$$

where N_b is the number of microbunches in a macropulse and $N_{slice} = 400$ is the number of current pulse slices.

The coherent transition radiation intensity from a bunch of N_e electrons scales linearly with the number of electrons per bunch squared,

$$I_{cTR} \text{ (per bunch)} \propto N_e^2. \tag{4.2}$$

Since we have N_b electron bunches,

$$I_{cTR} \text{ (per macropulse)} \propto \sum_{i=1}^{N_b} N_{ei}^2 \approx \left(\frac{N_b}{N_{slice}}\right) \sum_{j=1}^{N_{slice}} N_{ej}^2. \tag{4.3}$$

We measure the intensity of the backward transition radiation as a function of beam current. The radiation is passed through a 19-mm-diameter, 1.25-mm-thick HDPE window and is collected toward the detector by a copper cone. The acceptance angle is ± 120 mrad which is limited by the size of the window. The transition radiation intensity as a function of the sum of number of electrons in each microbunch squared is shown in Figure 4.1. The measurement confirms that the radiation intensity scales with the number of electrons squared as expected for the coherent radiation.

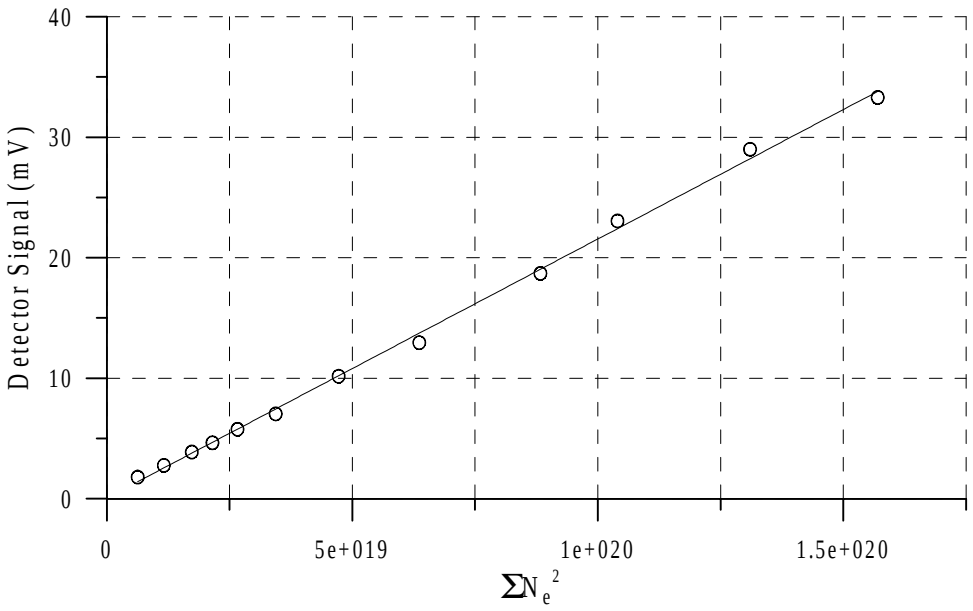

Figure 4.1: Transition radiation intensity as a function of the sum of number of electrons in each microbunch squared. The circular marks represent the measurement and the solid line represents a linear fit.

4.2 Spectral Distribution

The spectral distribution of incoherent transition radiation is uniform up to very high frequencies well beyond our range of interest. The spectral distribution of coherent transition radiation, on the other hand, has a limited range from very long wavelengths down to wavelengths comparable to the electron bunch length. In general, radiation at long wavelengths is suppressed by the vacuum chamber [22]. Wavelengths comparable to and longer than the chamber radius ($10 - 15$ mm in our case) cannot propagate. It is worth mentioning that this effect limits the generation of coherent synchrotron radiation in a storage ring since the bunch length in a storage ring is on the order of a few centimeters or longer. Only recently, burst of coherent synchrotron radiation has been observed [23].

The spectral distribution of coherent transition generated from femtosecond electron bunches at SUNSHINE is measured using a Michelson Interferometer. After

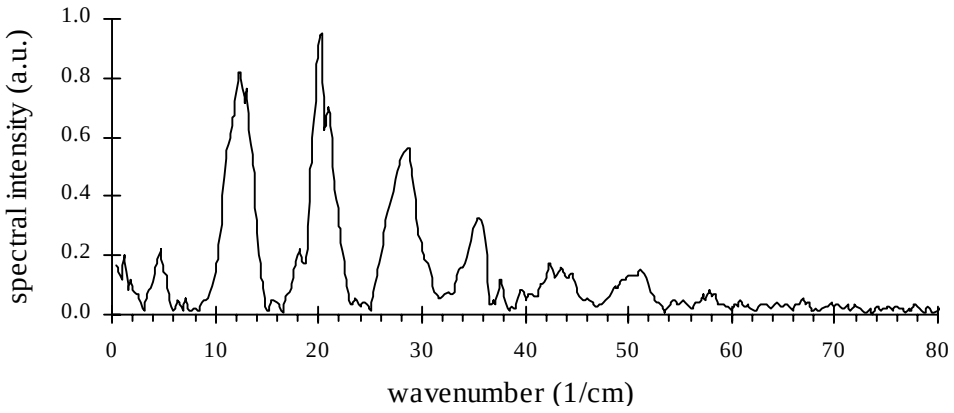

Figure 4.2: Coherent transition radiation spectrum obtained from the in-air Michelson interferometer.

recording an interferogram of the backward transition radiation, the spectral distribution of the radiation is calculated by taking the Fourier transform of the interferogram. The relationship between the radiation power spectrum and the interferogram is shown in (3.5). Figure 4.2 shows the spectral distribution obtained from an interferogram recorded by a Michelson interferometer set up in ambient air. In the interferometer, a 25.4-μm-thick Kapton film has been used as a beam splitter. Such a beam splitter has non-zero frequency response, shown in Figure 3.9, over the frequencies of our interest. The measured radiation spectrum indicates that the radiation obtained from short electron bunches at SUNSHINE covers the far-infrared regime. In addition to the suppression by the vacuum chamber, the low frequency suppression in the spectrum is due to the beam splitter interference as described in 3.5. The spectrum exhibits absorption from the water vapor in air and also reveals strong features of a periodic absorption. This periodic absorption is the result of the interference in the pyroelectric detector used in the Michelson interferometer. The interference causes constructive interferences and destructive interferences at specific frequencies. More details of this effect will be discussed in Chapter 5.

To eliminate the absorption by water vapor, an in-vacuum Michelson interferometer has been constructed. In this case, the measured radiation spectrum is free of water absorption lines as shown in Figure 4.3. Other than the water absorption lines,

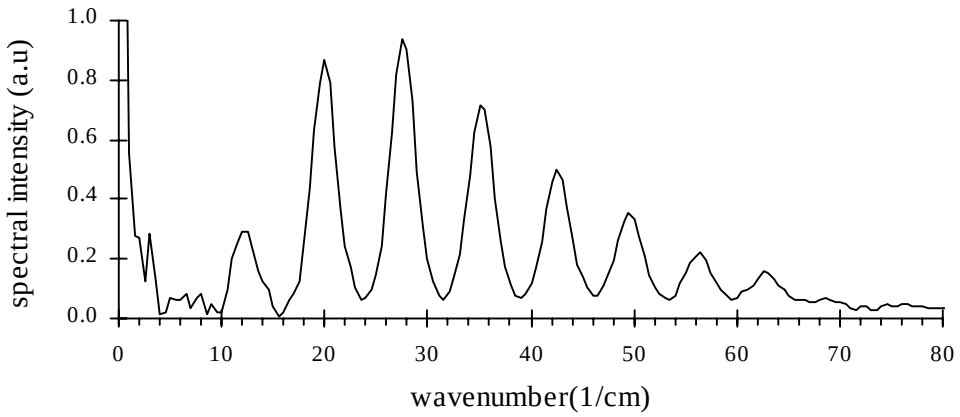

Figure 4.3: Coherent transition radiation spectrum from the in-vacuum Michelson interferometer.

the spectrum in Figure 4.2 and Figure 4.3 show some differences at low frequencies. The low frequency components in the spectrum taken from the in-vacuum seem to be more suppressed even though the two Michelson interferometer are set up with the same kind and same thickness of the beam splitter. This extra suppression at low frequency can be explained by diffraction from the mirrors used in the setup.

The setup of the in-air and in-vacuum Michelson interferometers has been described in Section 3.5 and Section 3.6. Due to space limitations of the in-vacuum setup, smaller parabolic mirrors (25-mm diameter) are used to collimate the coherent transition radiation generated at the radiator and to focus the radiation beam onto the detector. Figure 3.14 shows the first parabolic mirror P1 and Figure 3.15 shows the second parabolic mirror P2. These mirrors however cause some low frequency suppression by diffraction. The low frequency suppression of the system can be estimated by considering two circular apertures placed at 90-cm apart which is the distance between the parabolic mirror P1 and P2. Diffraction from the first aperture results in intensity distribution described by a Bessel function (considering Fraunhofer diffraction). The fraction of total energy contained within an area of the second aperture then can be estimated [24]. The solid line in Figure 4.4 shows the effect of diffraction of two 25-mm-diameter aperture separated by 90 cm, clearly displaying the suppression at low frequency. Frequencies below wavenumbers of 15 cm^{-1} are

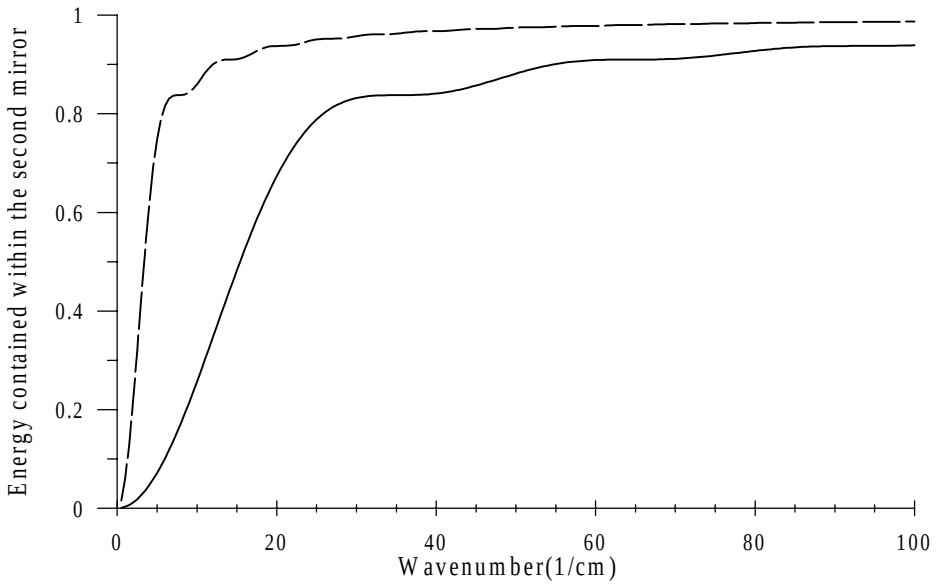

Figure 4.4: Calculation of the diffraction limited spectral transmission through the in-vacuum Michelson interferometer with two 25 mm diameter mirrors P1 and the P2 at a distance of 90 cm apart (solid), and through the in-air Michelson interferometer with a 63 mm diameter mirror P1 and a 25 mm diameter aperture copper cone at a distance of 50 cm apart (dashed-line).

heavily suppressed. For comparison, we estimate the diffraction effect of the in-air interferometer, whose setup shown in Figure 3.12, with the first parabolic mirror P1 having a diameter of 63 mm. In this setup, a copper cone has been used to collect the radiation into the detector instead of a second parabolic mirror. The copper cone has a circular aperture of 25 mm and the distance between the cone and parabolic mirror P1 is 50 cm. Considering the size of the mirror P1, the circular aperture of the cone, and the distance between them, the diffraction effect can be estimated. The result is shown by the dashed-line in Figure 4.4. The low frequency suppression is less severe than that of the in-vacuum interferometer.

Figure 4.5 shows again the radiation spectrum obtained from the in-vacuum Michelson interferometer (in solid) along with the spectrum computed from a 2-mm-long interferogram excluding the signatures from the detector artifacts. By using the 2-mm-long interferogram, the spectral resolution is 5 cm^{-1} and can not resolve

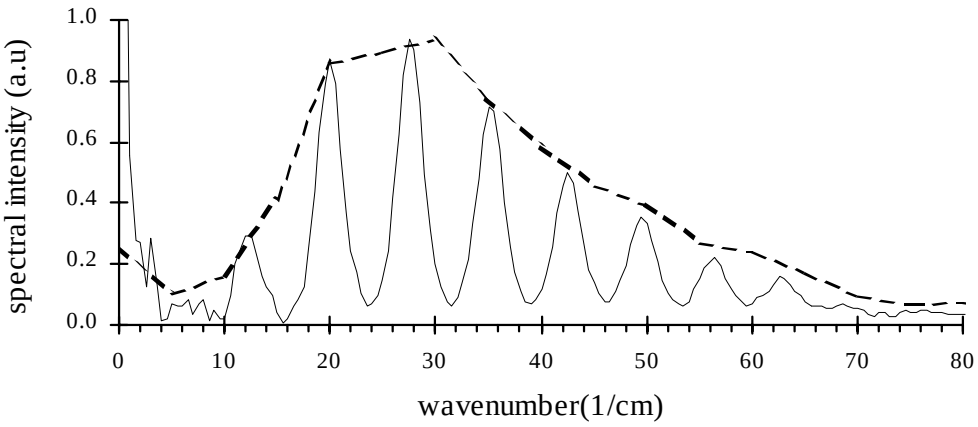

Figure 4.5: Coherent transition radiation spectrum and the spectrum without the detector interference effect (dashed-line).

the interferences of the pyroelectric detector. This spectral distribution therefore represents the emitted coherent transition radiation from the electron bunches. The radiation is a broadband spectrum reaching from microwaves to wavenumbers of 80 cm^{-1}. Since the radiation intensity collected in the Michelson interferometer depends on the beam splitter efficiency and other factors, the spectrum intensity have been presented in arbitrary units. The corrected spectrum, after applying the correction for beam splitter efficiency and mirror diffraction, is shown by a solid curve in Figure 4.6. The dashed-line represents the raw spectrum obtained from the in-vacuum Michelson interferometer. The dotted-sections in the corrected spectrum show sections which are near singularities in the beam splitter efficiency and thus are overcorrected. The corrected spectrum shows the spectral energy density available in an acceptance angle of ± 165 mrad which is equivalent to collecting 39% of the transition radiation generated from a 25 MeV beam.

4.3 Total Energy Measurement

The total radiation energy can be obtained by collecting the backward transition radiation over a large solid angle. A schematic diagram of the experimental setup for

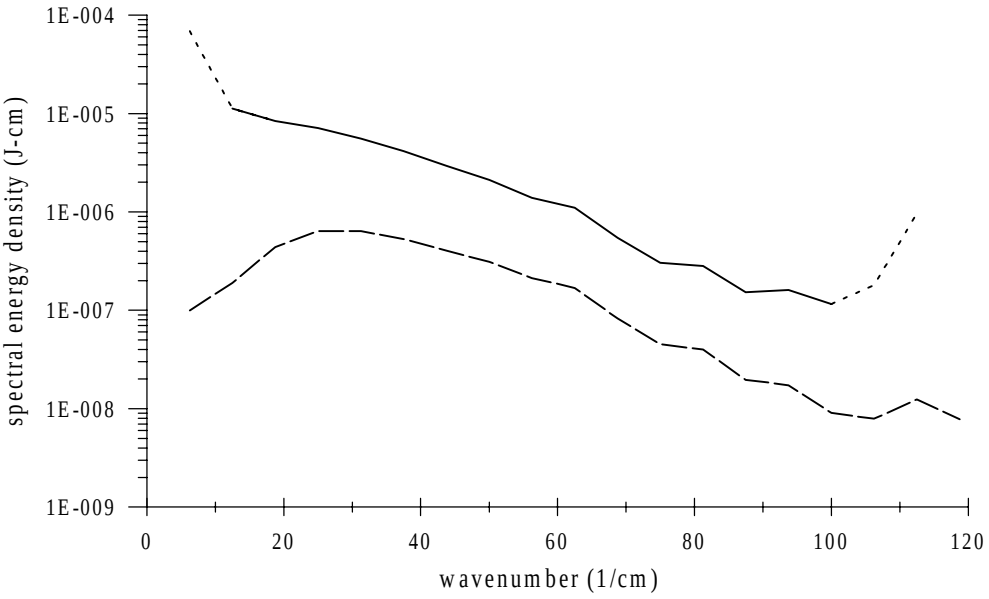

Figure 4.6: Coherent transition radiation raw-spectrum (dashed-line) and the corrected spectrum (solid line) after applying the correction for beam splitter effciency and mirror diffraction.

this measurement is shown in Figure 4.7. The backward transition radiation is generated as described in 3.2. A pyroelectric detector is moved across the photon beam in the xy-plane collecting the radiation coming form a 32 mm diameter polyethylene window. The detector is mounted on two orthogonal translation stages and the movement is controlled through a PC as described in Section 3.4. Through a computer interface under the LABVIEW environment, the detector can be moved in x or y direction with a selectable step size and the detector signal at each location is recorded. The scanning plane is 178 mm away from the center of the radiator. Scanning over an area of 55 mm $\times$ 55 mm, the total collected radiation is about 400 μJ per macropulse.

The expected value of radiation energy can be computed using (1.3), (1.4), and (2.13) assuming a Gaussian bunch with $\sigma_z = 40$ μm. With 87% transmission of the polyethylene window, the expected radiation energy is 745 μJ which is twice of the measured value. Most of the discrepancy is believed to be due to variation of the bunch length along a macropulse. Since optimum bunch compression works for a narrow range of central momentum, a macropulse with momentum variation will

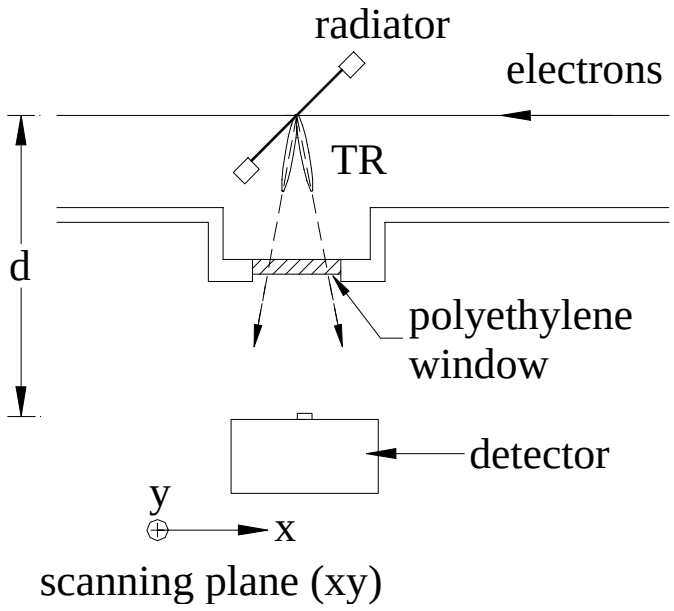

Figure 4.7: Experimental setup diagram for the total energy meaurement and for the radiation distribution measurement.

result in bunch length variation after compression. This variation of bunch length, in principle, can be derived through simulations of electron bunch generation [1]. Correction of the total radiation energy generated by a macropulse due to the bunch length variation is discussed in Refs. [16] and [1].

4.4 Spatial Distribution

The spatial distribution of transition radiation is obtained from the same setup and procedure described in the previous section. The center of horizontal scan is located at 90° with respect to the beam trajectory while that of the vertical scan is level with the beam trajectory. The center of the scanning plane is expected to be the center of the backward radiation cone emitted from 45° oblique incidence. A 2.5-mm-diameter iris has been placed in front of the pyroelectric sensor to provide higher resolution of the distribution from a scan. The detector and the iris are moved in steps across the transition radiation beam; and the radiation intensity at each position is

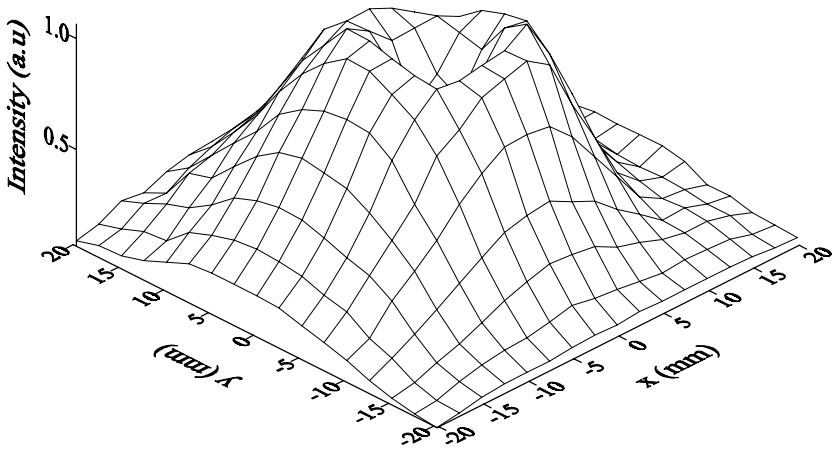

Figure 4.8: Radiation pattern obtained by scanning a detector in the XY-plane.

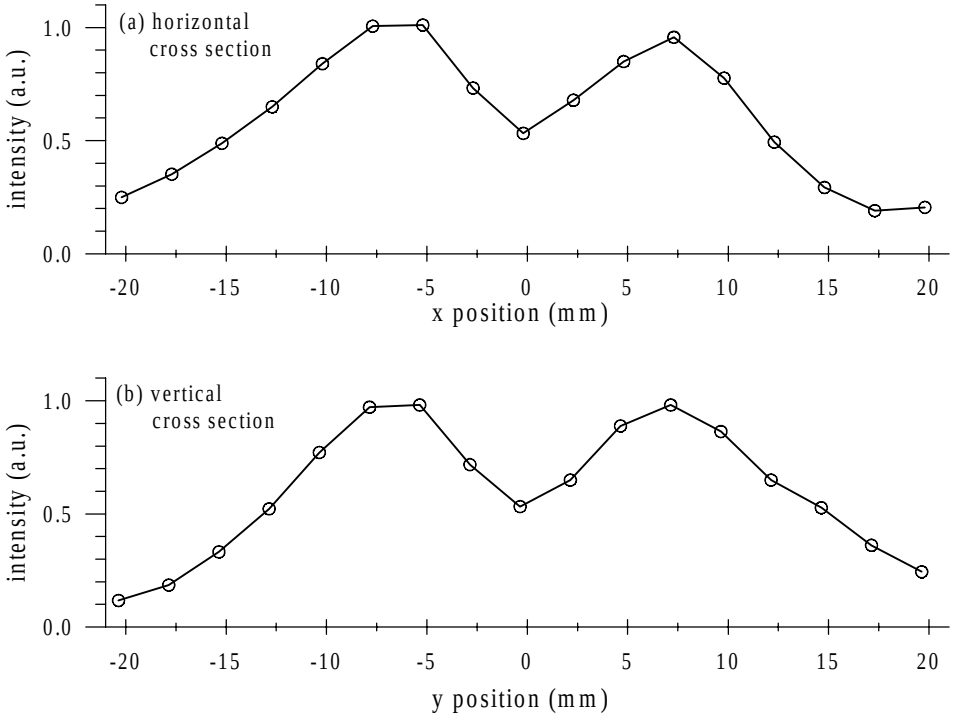

Figure 4.9: (a) horizontal cross-section and (b) vertical cross-section of the XY radiation distribution.

recorded. In the measurement, the scanning step is 2.5 mm for both direction. The radiation distribution, obtained from the measurement, is shown in Figure 4.8. The radiation pattern is similar to that shown in Chapter 1 where transition radiation properties were discussed. The distribution is hollow at the center of the radiation cone, reaching maximum at the distant around 6 mm from the center. Figure 4.9 shows the horizontal and vertical cross-sections of the radiation distribution which are easier to visualized. The circular marks show recorded intensity while the lines are just connecting them. The vertical cross section seem to be more symmetric than the horizontal cross section. Although one would expect an asymmetry only in the horizontal cross section for the transition radiation from 45° incidence in out setup, it is not clear that the asymmetry observed here is the result of the oblique incidence or others variation that might occur during the scan which took about 1 hour to complete. For a 26 MeV beam, the theoretical asymmetry is of the order of $10-15\%$ [Figure 1.7(a)].

From the radiation pattern, we found the maximum intensity at the position $6.5\pm$ 0.5 mm from the center of the radiation cone. According to the theory of transition radiation (using now TR from normal incidence for simplicity), its maximum intensity is located at $\theta \approx 1/\gamma$, where θ is the angle between the radiation direction and the center of the radiation cone. For a 26 MeV beam, which is the average energy of the beam in the measurement, this theoretical maximum intensity should be at 3.5 mm from the center of the radiation cone. Possible reasons for this large discrepancy are correction for oblique incidence, energy spread of the beam, interference of transition radiation generated from a beam with a finite beam size, a finite size of a radiator [25], and a finite absorption area of the detector. Estimate of all this effects can explain a widening of the distribution from having a maximum intensity at 3.5 mm to around 5 mm which is still smaller than the observation.

4.5 Polarization

The angular spectral intensity of transition radiation from normal and from oblique incidence, particularly for 45° incidence, are described in Chapter 1. For the case

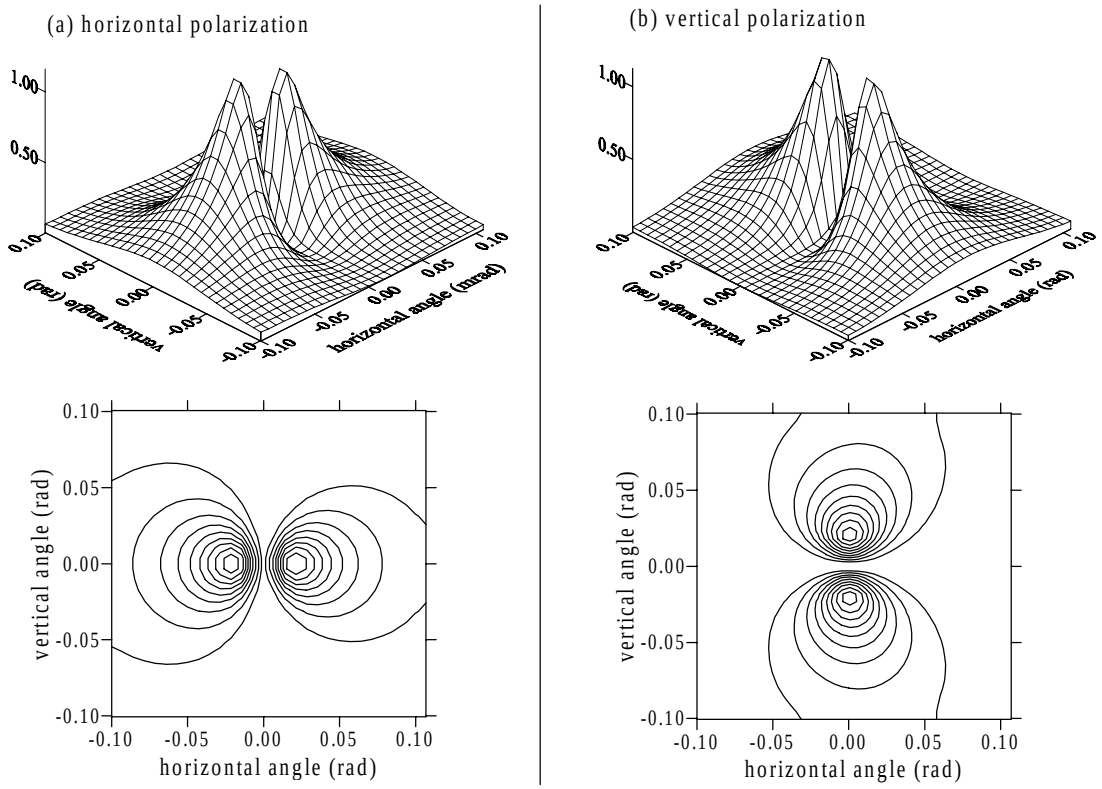

Figure 4.10: Horizontal and vertical polarization of the backward transition raditaion from a 26 MeV electron, 45° oblique incidence.

of normal incidence the radiation has only one component which is parallel to the radiation plane, defined as the plane containing radiation direction **k** and the direction normal to the interface. The whole radiation distribution is therefore radially polarized. Although the radiation from 45° incidence is composed of two components (parallel and perpendicular to the radiation plane the radiation), the distribution of transition radiation generated by a 26 MeV beam from 45° incidence is very similar to that from normal incidence. To analyze the radiation pattern for the geometry defined in Figure 4.7, we call for the distribution of horizontally polarized radiation (along the x axis) and the distribution of vertically polarized radiation (along the y axis). The horizontally and vertically polarized components can be obtained by decomposing the parallel and perpendicular components expressed in (1.8) and (1.9)

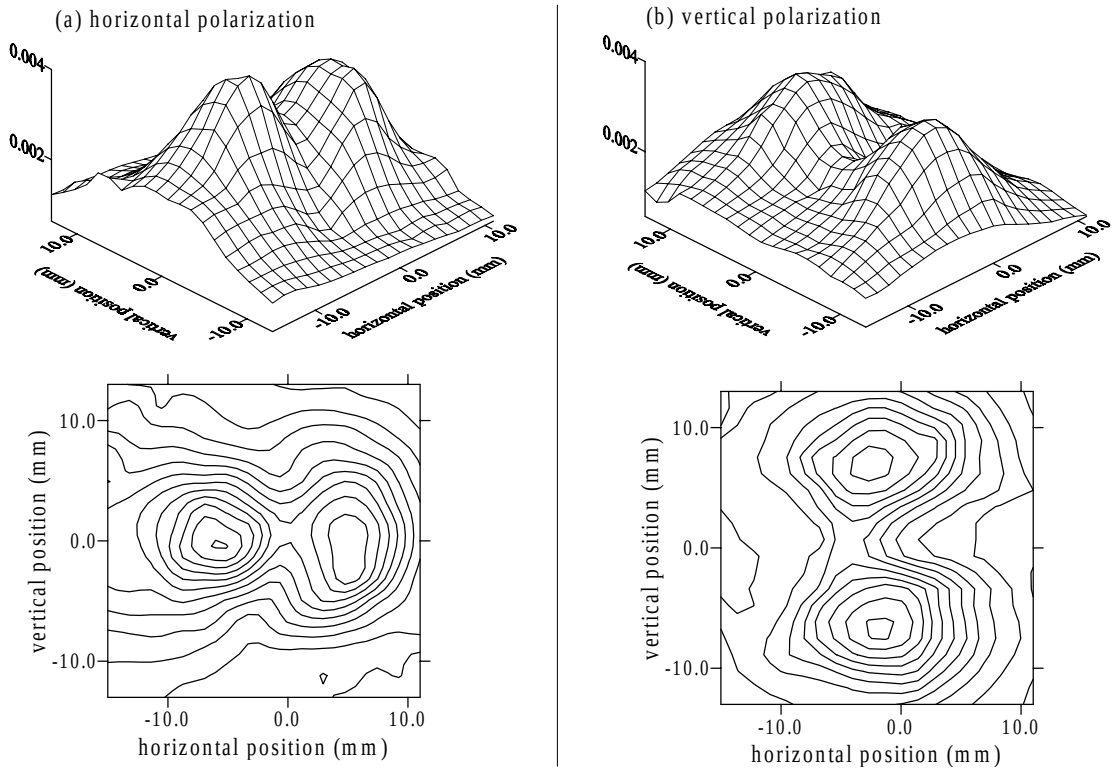

Figure 4.11: Horizontally and verticlaly polarized radiation components measured using a wire grid polarizer.

onto each axis. The radiation distributions for horizontal and vertical polarizations are illustrated in Figure 4.10, showing that the radiation is very close to be radially polarized.

The polarization of the transition radiation is measured using a wire-grid polarizer from Graseby-Spec (Model IGP223). The polarizer consisted of 4 μm wire-grid photo-lithed onto a polyethylene substrate. The spatial distribution is measured first with the polarizer oriented such that it allows the horizontally polarized radiation to pass, then measured with the polarizer rotated 90°, allowing the vertically polarized radiation to pass. Figure 4.11 shows the experimental results of the horizontal and vertical polarizations. It can be seen that the radiation distributions for the horizontal and vertical polarizations resemble those of the theoretical ones shown in Figure 4.10.

4.6 Effects of Beam Sizes

The spectral intensity of coherent transition radiation is determined by distribution of the electron bunches emitting the radiation. It is often evaluated by assuming that the contribution from transverse distribution is negligible so that the spectral intensity can be described only by the bunch longitudinal distribution. In general, minimizing the beam size will reduce transverse effects to coherent radiation properties as will be discussed in this section.

For a Gaussian bunch with the distribution as defined in (2.12) and (2.20), its form factor can be written as

$$f(\omega,\theta) = e^{-\left[(\omega\sigma_\rho \sin\theta/c)^2+(\omega\sigma_z \cos\theta/c)^2\right]}. \tag{4.4}$$

The transverse distribution can be neglected under the condition that

$$\sigma_z \cos\theta \gg \sigma_\rho \sin\theta \ , \tag{4.5}$$

where θ is the observation angle. This condition indicates that transverse effects can be reduced by a small transverse beam size at the radiation source and a small observation angle. Let us apply our experimental parameters, a typical bunch length of $\sigma_z = 40$ μm and a typical well-focussed beam size with $\sigma_\rho = 0.5$ mm, to the condition (4.5). If we choose to observe the radiation at $1/\gamma$ for the maximum intensity ($\theta = 1/\gamma = 20.4$ mrad for a 25 MeV beam), the right hand side of (4.5) becomes 10.2 μm while the left hand side yields 39.9 μm. Thus the condition in (4.5) is roughly valid for this case but it may not satisfy if the observation angle become larger.

Experiments to investigate the effects of the beam size on coherent transition radiation intensity have been conducted. The beam size is measured by taking an image of the beam on a fluorescent screen which is mounted behind the radiator. Details of the beam profile monitor and how to obtain the transverse beam profile are described in Chapter 3. In this experiment, electron beam sizes are varied using a pair of quadrupole magnets located 60 cm upstream from the radiator. The spectral distributions of coherent transition radiation generated from electron bunches with

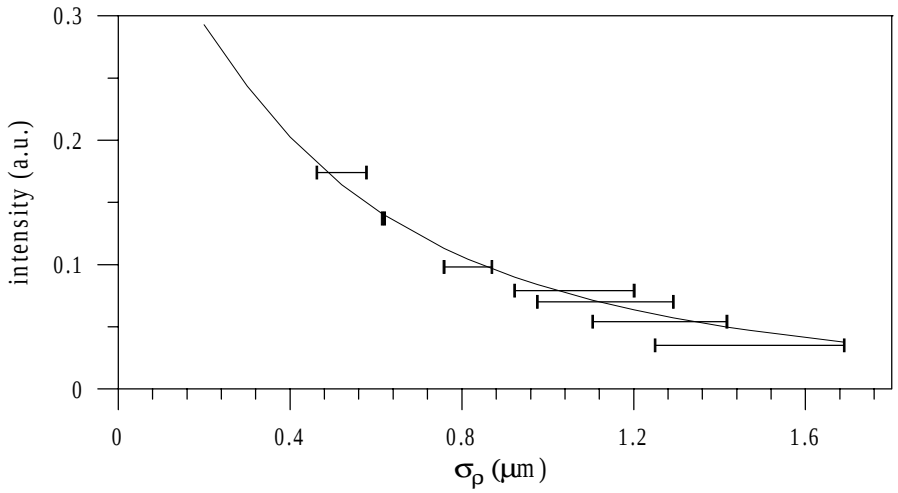

Figure 4.12: Coherent transition radiation intensity from various beam sizes (— : theoretical estimate).

different transverse beam sizes are recorded using the in-vacuum Michelson interferometer. To obtain the total intensity we integrate the radiation spectrum over all frequencies. The total intensity as a function of beam size is shown in Figure 4.12, where the effective beam radius σ_ρ is between the two limits discussed in Section 3.1.2. Evidently, the radiation intensity decreases as the beam size increases. The solid line in the figure represents the theoretical intensity obtained from the following calculation.

The theoretical intensity can be computed starting from the expression of coherent transition radiation intensity at an observation angle θ

$$I_{cTR}(\omega,\theta) = N_b N_e^2 I_{TR}(\omega,\theta)\, f(\omega,\theta)\,, \tag{4.6}$$

where N_b is the number of bunches, N_e is the number of electrons per bunch and $f(\omega)$ is the form factor (4.4) for a Gaussian bunch. For simplicity, $I_{TR}(\omega,\theta)$ is the transition radiation intensity generated by an electron from normal incidence on the interface between vacuum and perfect conductor which has no frequency dependence. The collected radiation within an acceptance angle of θ_a can be obtained by integrating

over the solid angle as

$$I_{cTR}\left(\omega,\theta_a\right)=N_bN_e^2\int_0^{2\pi}\int_0^{\theta_a}I_{TR}\left(\theta\right)f\left(\omega,\theta\right)\sin\theta\mathrm{d}\theta\mathrm{d}\phi. \tag{4.7}$$

Since the frequency response of the instruments impacts on the radiation intensity, it must be included in the estimation. This frequency response is due to the beam splitter efficiency $|R(\omega)T(\omega)|^2$, described in Section 3.5, and the transmission factor from the mirror diffraction $M\left(\omega\right)$, described in Section 4.2. The radiation intensity collected by the in-vacuum Michelson interferometer is then

$$\begin{aligned} I_{cTR}(\omega,\theta_a) &= N_bN_e^2\left|R(\omega)T(\omega)\right|^2M(\omega)\int_0^{2\pi}\int_0^{\theta_a}I_{TR}\left(\theta\right)f\left(\omega,\theta\right)\sin\theta\mathrm{d}\theta\mathrm{d}\phi \\ &\propto \left|R(\omega)T(\omega)\right|^2M(\omega)\int_0^{\theta_a}I_{TR}\left(\theta\right)e^{-\left[(\omega\sigma_\rho\sin\theta/c)^2+(\omega\sigma_z\cos\theta/c)^2\right]}\sin\theta\mathrm{d}\theta. \end{aligned} \tag{4.8}$$

The expression indicates that the contribution from the transverse distribution causes the coherent radiation spectrum to drop at lower frequencies as the beam size becomes larger. The radiation spectral width, thus, becomes narrower.

After the integration of (4.8) over all frequencies, the total intensity becomes

$$I_{cTR}\left(\theta_a\right)\propto\int_0^{\infty}\left|R(\omega)T(\omega)\right|^2M(\omega)\int_0^{\theta_a}I_{TR}\left(\theta\right)e^{-\left[(\omega\sigma_\rho\sin\theta/c)^2+(\omega\sigma_z\cos\theta/c)^2\right]}\sin\theta d\theta d\omega. \tag{4.9}$$

The expected intensity of various transverse beam sizes can now be computed using (4.9) , assuming a 25 MeV monochromatic beam and a Gaussian bunch of σ_z= 26 μm (refer to Section 5.5 for the estimation of σ_z). The Amplitudes of the expected intensity are scaled to the measurement by a constant factor obtained from a least squares fit to $\sigma_{\rho,\mathrm{CENTER}}$ which is the value of σ_ρ in the center between the two limits. The measurement agrees with theoretical expectation.

The spectral distribution associated with each beam size is shown in Figure 4.13. The measurement confirms that when the beam size increases, the radiation intensity

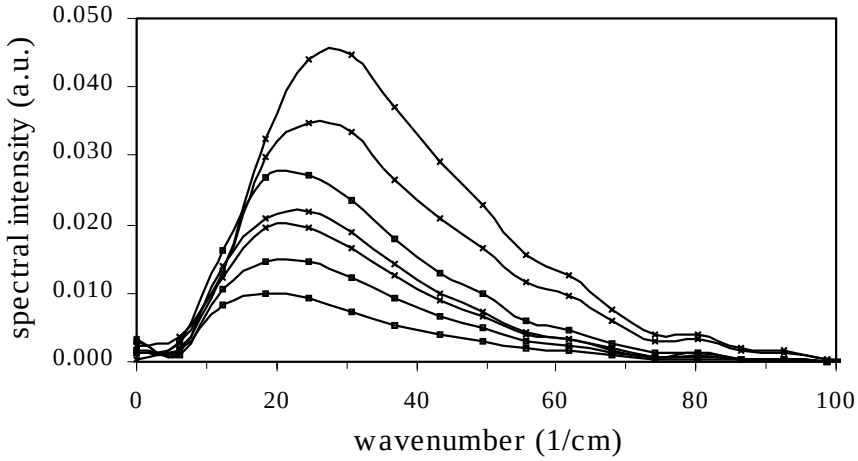

Figure 4.13: Spectral intensity of coherent transition radiation from the bunch with various beam sizes.

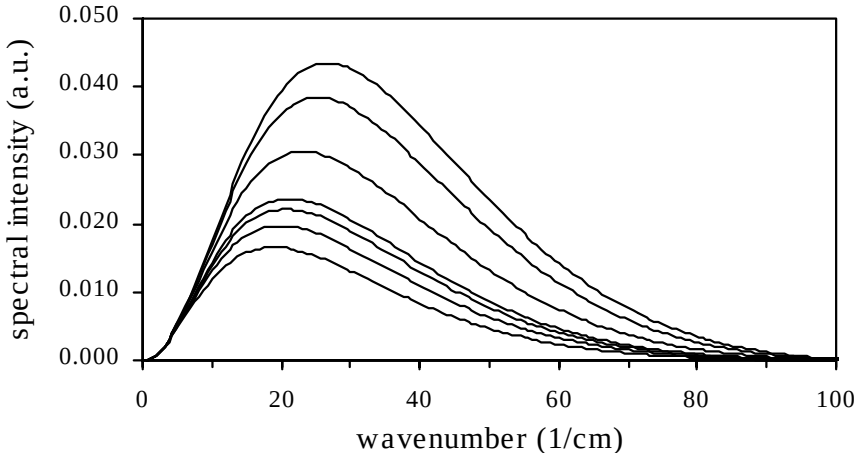

Figure 4.14: Calculated spectral intensity of coherent transition radiation from a Gaussian bunch with $\sigma_\rho = \sigma_{\rho,\mathrm{CENTER}}$.

decreases and the high frequency components of the radiation are more suppressed due to interference effects. The smallest beam size in the measurement gives the highest intensity and the broadest spectrum. For comparison, the spectral distributions of coherent transition radiation obtained from a Gaussian bunch are calculated using (4.8) and $\sigma_\rho = \sigma_{\rho,\text{CENTER}}$, using the same normalized factor obtained earlier from the least squares fit. The calculated spectra are shown in Figure 4.14. The decrease in intensity as well as the narrowing of the spectrum, as the beam size increases, in the measurement and in the calculation agree within the limits of the effective beam size.

Effects of the electron beam size to the coherent radiation intensity and spectrum have just been demonstrated experimentally as well as theoretically. For a Gaussian bunch distribution, the condition shown in (4.5) can be used to estimate how strong the contribution is from transverse distribution. In the following discussion, we look closely into the relationship between transverse beam sizes, bunch lengths, observation angles, and coherent radiation spectral width of a Gaussian bunch.

Define the critical frequency ω_c in a Gaussian form factor $f(\omega) = e^{-(\omega\sigma_z/c)^2}$ as

$$\omega_c^2 = \frac{c^2}{\sigma_z^2}, \tag{4.10}$$

which represents the frequency at which the form factor drops down to $1/e^2$ or 13.53% of the maximum. Note that the above is for the case of an infinitely thin beam $(\sigma_\rho = 0)$.

For a Gaussian bunch with $\sigma_\rho \neq 0$, its form factor is shown in (4.4) and the critical frequency for this case becomes

$$\omega_c^2 = \frac{c^2}{\sigma_z^2 \cos^2\theta + \sigma_\rho^2 \sin^2\theta}. \tag{4.11}$$

Since the transition radiation has its maximum intensity at $1/\gamma$ which is very small for relativistic electrons (even an observation angle of a few times $1/\gamma$ gamma is still

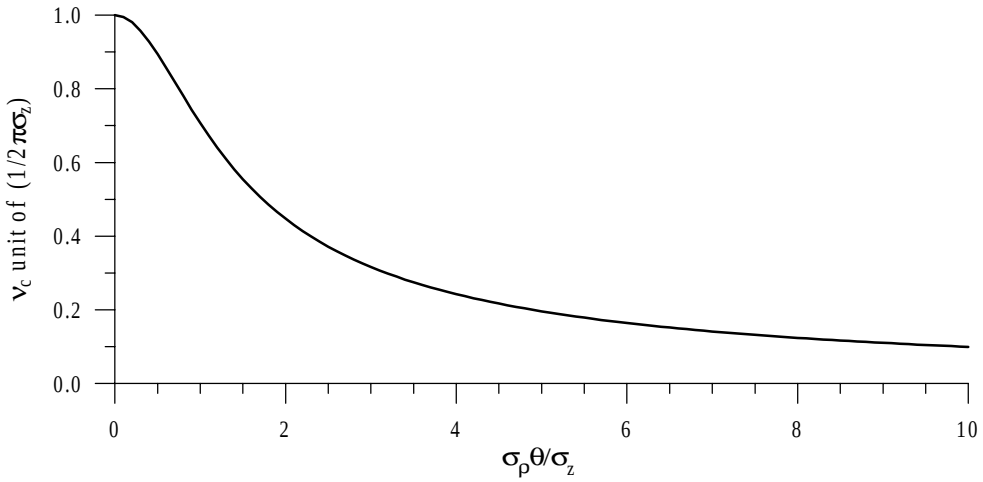

Figure 4.15: Normalized critical frequency as a function of $\sigma_\rho\theta/\sigma_z$.

considered small), the critical frequency in (4.11) can be simplified to

$$\omega_c^2 \approx \frac{c^2}{\sigma_z^2\left(1+\sigma_\rho^2\theta^2/\sigma_z^2\right)}. \tag{4.12}$$

Equation (4.12) shows effects of the beam size and the observation angle on the critical frequency of the coherent transition radiation. When $\sigma_\rho\theta \to 0$, the critical frequency is determined solely by σ_z. As $\sigma_\rho\theta$ is getting larger, the critical frequency becomes lower. Figure 4.15 shows the critical frequency $\nu_c = \omega_c/2\pi c$, normalized to that of an ideal case when $\sigma_\rho\theta = 0$, as a function of $\sigma_\rho\theta/\sigma_z$. One can see that the critical frequency is lower as $\sigma_\rho\theta$ becomes larger compared to σ_z. When $\sigma_\rho\theta/\sigma_z = 10$, for example, the critical frequency reduced to only 10% of the ideal case. Figure 4.16 displays coherent spectral distribution when $\sigma_\rho\theta/\sigma_z = 0.1$, 1, and 10. For a larger $\sigma_\rho\theta/\sigma_z$, the spectral width is narrower. To obtain the full coherent radiation spectrum which is bunch length limited, the electron beam size should be as small as possible. For the same reason, smaller angles would also be preferred. However limiting the acceptance angle to a small one will reduce the collected radiation intensity. The optimum choice therefore depends on the particular interest of either broad spectrum, high intensity or both.

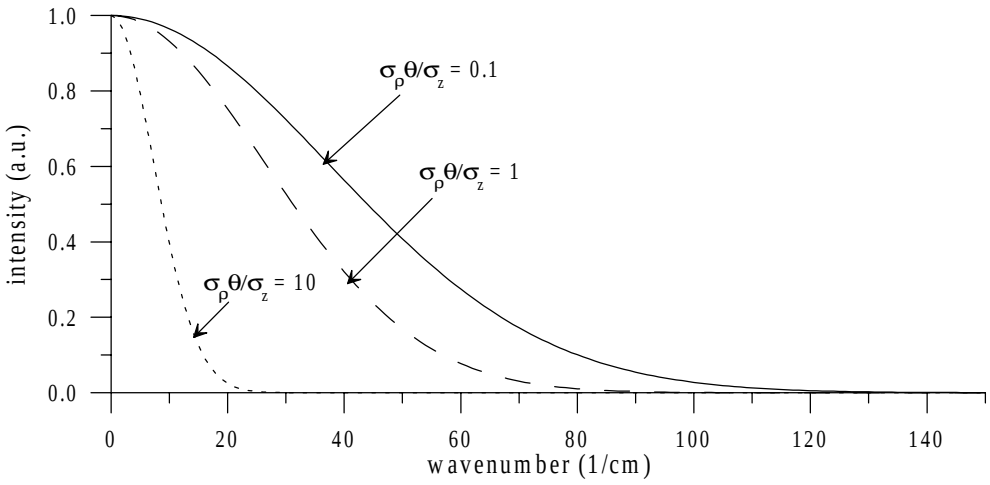

Figure 4.16: Coherent radiation spectral distribution for $\sigma_\rho\theta/\sigma_z = 0.1$ (solid), 1 (dashed-line), and 10 (dotted-line).

4.7 Coherent TR Summary

The measured properties of the coherent transition radiation generated at SUNSHINE is summarized and presented in Table 4.1. The radiation covers much of the far-infrared spectral range and high intensity radiation from millimeter waves up to 100 cm^{-1} can be detected with a room temperature detector. The radiation pulse duration (σ_z) is as short as 120 femtosecond which is equivalent to 35 μm. We observed the radiation energy of about 400 μJ per macropulse, containing about 3000 radiation pulses. The radiation is collected within an acceptance angle of 154 mrad which is equivalent to 38% collection efficiency for a 25 MeV electron beam. An average power about 4 mW is yielded when operate at 10 Hz repetition rate. The radiation radiance, estimated from the collected radiation within $\pm$154 mrad, is shown in Figure 4.17 and compared to black body radiation at 1000K and synchrotron radiation. The radiation radiance ($W/mr^2/mm^2/100\%BW$) is four to seven orders of magnitude above that of back body radiation and is at least three orders of magnitude above that of the synchrotron radiation estimated using parameters from a typical VUV ring (E = 800 MeV, I_b= 500 mA, and B =1.4 T). It is possible to extend the spectral range of coherent transition radiation further by using shorter electron bunches.

Parameter	value	unit
Spectral range	$5 - 100$	cm^{-1}
Energy per macropulse	400	μJ
(38% collection effeciency)		
polarization	radial	
Macropulse power	400	W
Microbunch power	440	kW
Average power (at 10 Hz rep. rate)	4.0	mW
Micropulse duration (σ_τ)	120	fs
Micropulse separation	350	ps
Macropulse duration	1	μs
Number of radiation pulses/macropulse	~ 3000	pulses

Table 4.1: Measured properties of coherent transition radiation generated at SUNSHINE.

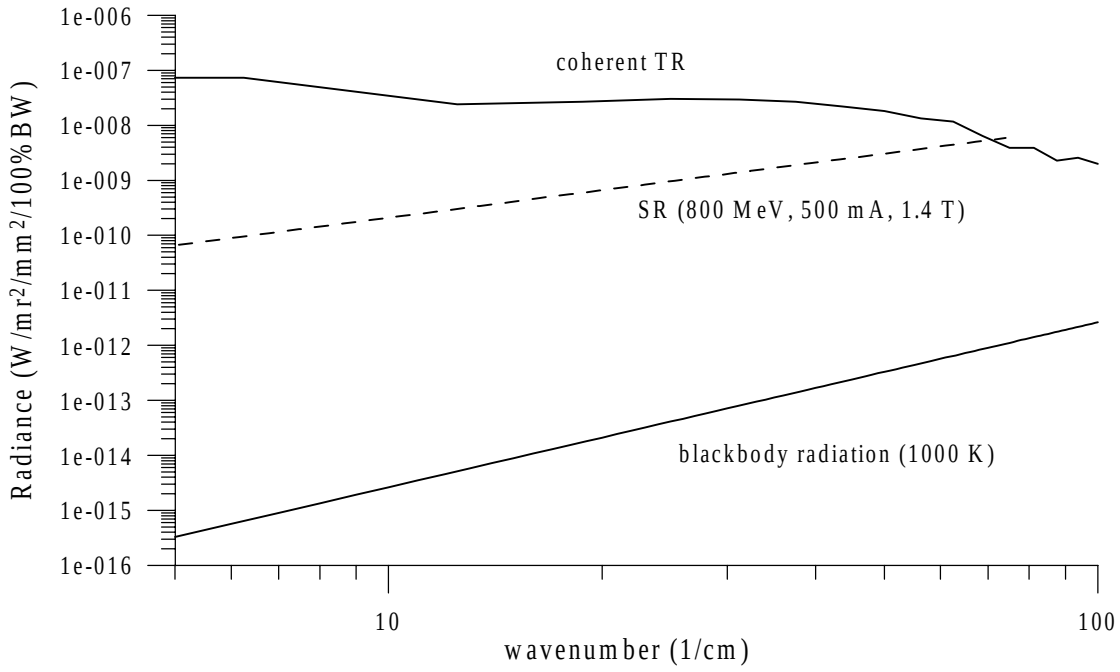

Figure 4.17: Far-infrared coherent transition radiation from femtosecond electron bunches compared to black body radiation and synchrotron radiation.

Chapter 5

Bunch Length Measurement

Coherent radiation is closely related to the bunch distribution since the Fourier transform of the particle distribution determines the spectrum of coherent radiation. Furthermore, the shorter the bunch length , the broader a coherent radiation spectrum is generated. At SUNSHINE, we measure bunch lengths using coherent transition radiation emitted at wavelengths longer than or equal to the bunch length. By analyzing the autocorrelation of coherent transition radiation, the bunch length can be determined [26]. The basic methods and experimental technique has been described elsewhere ([2],[3]) and are briefly repeated here. Some important issues regarding the technique and data analysis have been investigated in more detail during this thesis program. These issues include effects of the pyroelectric detector to the measurement, dispersion of the radiation pulse as it propagates through humid air, and effects of beam sizes to the measurement. Pulse reconstruction will also be discussed in this chapter.

5.1 Basic Principle

The coherent radiation spectrum is determined by the spectral distribution of the particular radiation emission process used and the bunch form factor. The spectral distribution of transition radiation, generated from a vacuum-metal interface, is considered to be frequency independent within the spectral range of our interest.

Therefore, the coherent transition radiation spectrum is determined solely by the bunch form factor. Since the bunch form factor relates to the particle distribution as its Fourier transformation squared, defined in (2.5), the coherent transition radiation spectrum relates directly to the particle distribution.

$$\begin{aligned} I_{cTR}(\omega) &= N_e^2 I_{TR} f(\omega) \\ &= N_e^2 I_{TR} \left| \int e^{ik\ \hat{n}\cdot\vec{r}} S(\vec{r}) d^3 r \right|^2 , \end{aligned} \tag{5.1}$$

where N_e is the number of electrons in the bunch and $S(r)$ is the particle distribution. A special case arises when the transverse distribution can be neglected,

$$\begin{aligned} I_{cTR}(\omega) &\approx N_e^2 I_{TR} f(\omega) \\ &= N_e^2 I_{TR} \left| \int e^{ikz} h(z) dz \right|^2 \\ &= N_e^2 I_{TR} |h(\omega)|^2 , \end{aligned} \tag{5.2}$$

where $h(z)$ is the longitudinal distribution of the bunch and $h(\omega)$ is its Fourier transform.

The coherent transition spectral distribution can be obtained using a Michelson interferometer. This has been described in Section 3.5 and the Fourier transform of the interferogram, which is the autocorrelation of the radiation pulse, is the radiation power spectrum.

$$\mathrm{FT}\{I(\delta)\} \propto \left| R(\omega) T(\omega) \tilde{E}(\omega) \right|^2 , \tag{5.3}$$

where

$$I(\delta) \propto 2\,\mathrm{Re} \int |RT|^2 E(t) E^*(t + \frac{\delta}{c}) \mathrm{d}t. \tag{5.4}$$

From (5.2) and (5.3), we can write

$$\mathrm{FT}\{I(\delta)\} \propto |h(\omega)|^2 . \tag{5.5}$$

Since the power spectrum of coherent transition radiation is the Fourier transform of the particle distribution squared, an interferogram directly represents the autocorrelation of the particle distribution. The bunch length can then be derived from the interferogram. For example, the interferogram of a rectangular pulse has a Full Width at Half Maximum (FWHM) equal to the pulse width and the interferogram of a Gaussian pulse has a FWHM equal to $4\sqrt{\ln 2}\sigma_z$ [3]. Since this method is based on optical principles, it works for any short bunch length for which optical elements are available.

5.2 Overview of the Technique

A schematic diagram of the bunch length measurement based on the coherent transition radiation autocorrelation technique is shown in Figure 5.1. Backward transition radiation is generated from a 45° tilted radiator. The radiation exits through a high density polyethylene window from the beam pipe and enters a Michelson interferometer. A typical interferogram obtained by scanning a movable mirror is also presented.

In order to analyze the interferogram efficiently, one must eliminate all effects that disturb the radiation spectrum and may therefore lead to erroneous bunch length measurements. The beam splitter has a particular spectral response, which comes from interferences of multiple reflections within the beam splitter. The spectral response can be calculated from optical constants of the material as discussed in section 3.5. The theoretical and experimental evaluations of beam splitter effects on the bunch length measurement have been reported in Refs. [2] and [3]. Corrections to this effects can be applied with the knowledge or assumption of the actual electron distribution. The studies in Ref. [3] show that the corrections are different for different particle distributions, for example, a Gaussian or a uniform distribution. For thick beam splitters, the bunch length can be obtained directly from the width of the interferogram measured in terms of optical path difference. Corrections must be applied if a thin beam splitter is used. The required correction becomes negligible if one uses a beam splitter which is thicker than about half the equivalent bunch length [3]. There is a similar concern related to water absorption for a bunch length measurement system

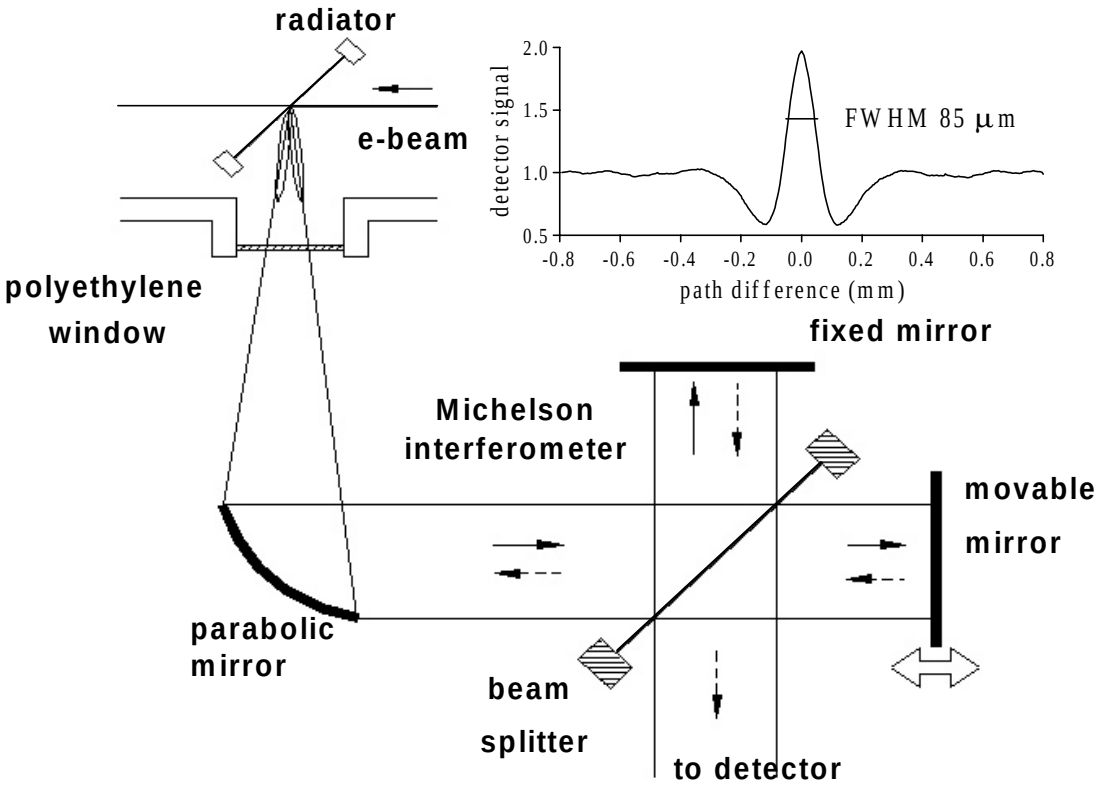

Figure 5.1: Michelson interferometer setup for bunch length measurements with a typical interferogram.

in ambient air. An interferogram and radiation spectrum obtained from the measurement in air is shown in Figure 3.13; many water absorption lines are visible in the spectrum. Although we believe that water absorption does not affect the overall shape of the spectrum, eliminating the effects will help us gain more information from the measurement. Not only do we obtain the bunch length from the interferogram and the radiation spectrum, but we also expect to get some information of the particle distribution. For this purpose, an in-vacuum Michelson interferometer has been assembled at SUNSHINE. The system in vacuum has allowed us to gain more information from the measurement and to study effects of ambient air on the bunch length measurement.

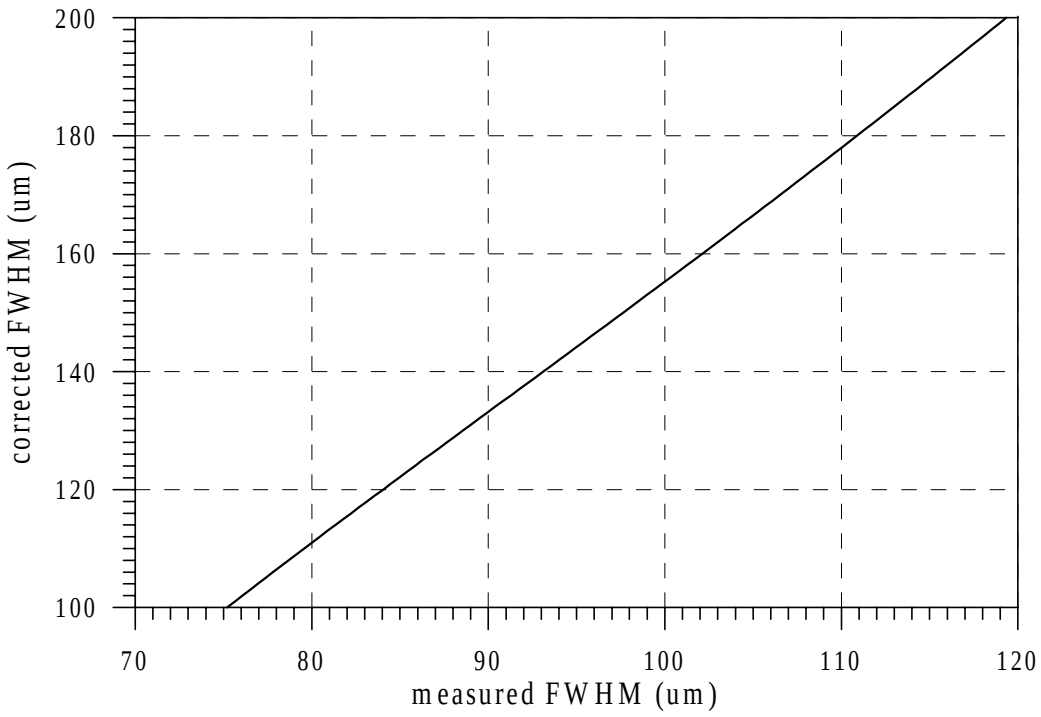

Figure 5.2: Corrected FWHM as a function of measured FWHM taken by the in-vacuum Michelson interferometer.

5.3 The In-vacuum System

The in-vacuum Michelson interferometer has been described in Section 3.6. In order to obtain an accurate result for a bunch length measurement, it is necessary to analyze some known impacts of the system on the measurement. In the in-vacuum Michelson interferometer, the radiation spectrum is perturbed by beam splitter efficiency and mirror diffraction. Since any perturbation to the radiation spectrum yields inaccurate bunch length measurements, we will first discuss effects of beam splitter response and mirror diffraction to bunch length measurement.

Low frequency suppression due to the beamsplitter interference is discussed in Section 3.6 and that due to the mirror diffraction in Section 4.2. Both effects cause the negative valleys to merge into the interferogram main peak similar to the effects of the beam splitter alone as demonstrated in Figure 3.11. As a consequence, the

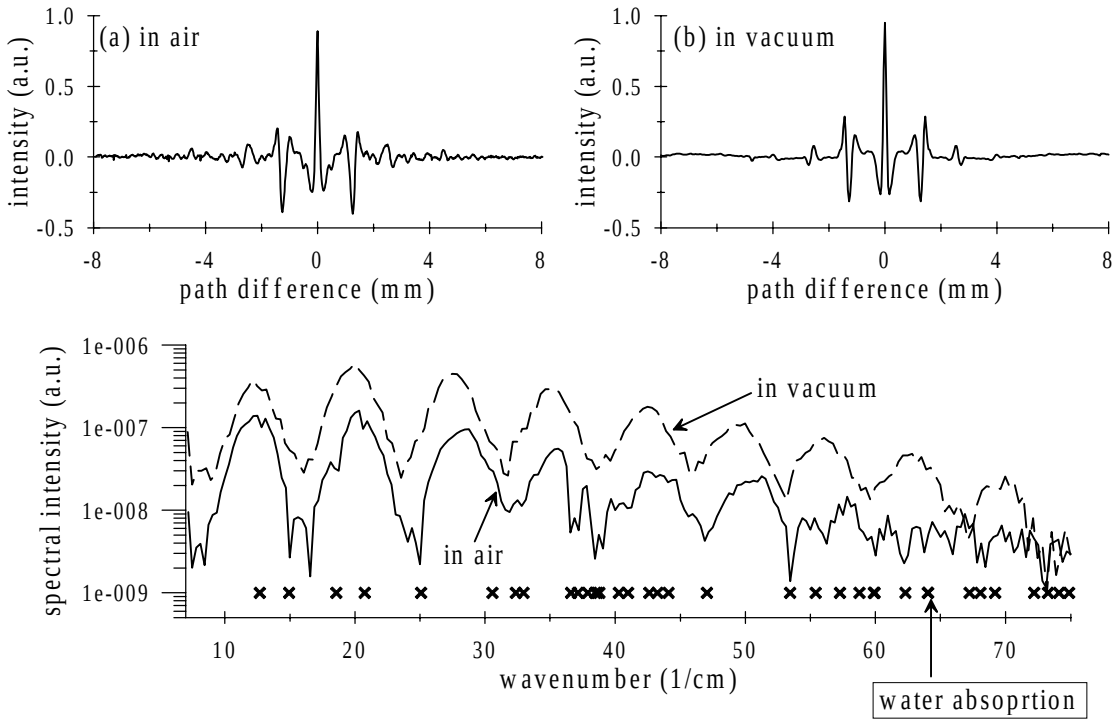

Figure 5.3: Interferograms and the radiation spectrums taken from the in-air interferometer and from the in-vacuum interferometer.

measured FWHMs will appear to be narrower than the real value. The correction can be obtained by considering the frequency response of the beam splitter and the low frequency suppression of the mirror diffraction. By applying both effects to the power spectrum of a Gaussian bunch, the corrected FWHM as a function of measured FWHM for a Gaussian bunch can then be obtained from simulated interferograms and is shown in Figure 5.2.

5.4 Bunch Length Measurement in Vacuum

Figure 5.3 shows interferograms and radiation spectra obtained from the in-air Michelson interferometer and the in-vacuum Michelson interferometer. Small oscillations in the interferogram from water absorption have vanished in the in-vacuum interferogram. The radiation spectrum taken in vacuum is also free from water absorption

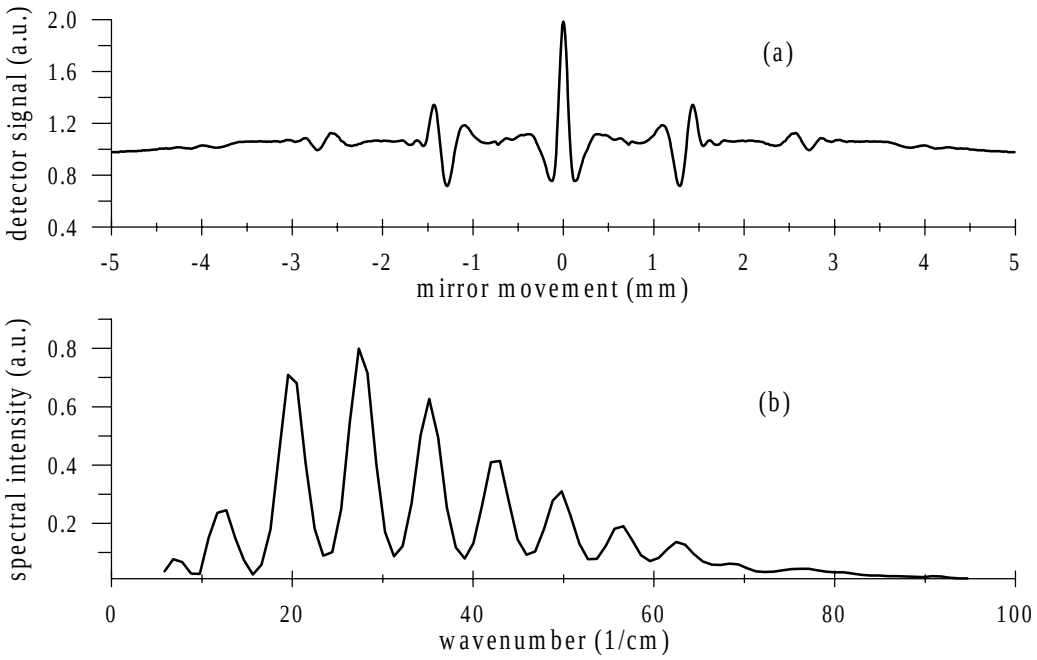

Figure 5.4: (a) interferogram and (b) radiation spectrum taken from the in-vacuum Michelson interferometer.

lines. The spectrum however is not smooth as we first expected. Instead, a strong feature in the radiation spectrum is now clearly visible. The feature has been observed in the radiation spectrum at all times but it was mistakenly identified as part of water absorption since the minima almost coincide with known strong water absorption lines. The periodic-like structures in the radiation spectrum become clear once the water absorption has been eliminated from the radiation spectrum and we can now understand the feature. An interferogram and the radiation spectrum taken from the in-vacuum Michelson interferometer are shown again in Figure 5.4. The spectrum clearly displays a periodic structure which could possibly be an outcome of interferences. The signatures in the interferogram also suggest that multiple reflections might occur. Since thin film interference of a 25-μm Kapton beam splitter features a zero efficiency at 112 cm^{-1}, the feature observed here does not result from the beam splitter. We believe that this feature is a result of the pyroelectric detector response.

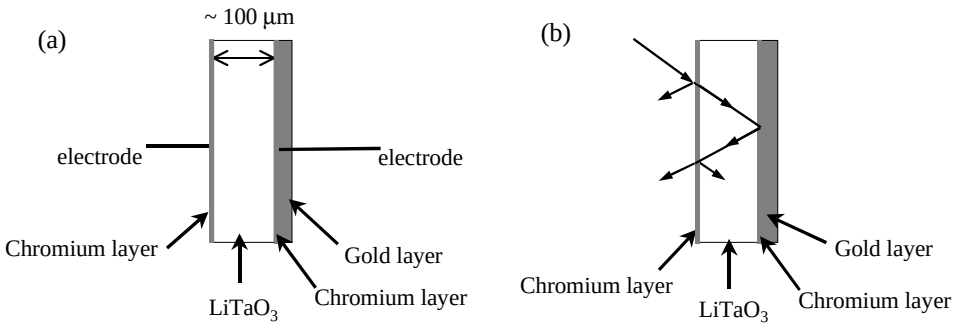

Figure 5.5: Scheamatic diagrams show structures of the pyroelectric sensor and the radiation absorption mechanism.

5.4.1 Internal Reflection in a Pyroelectric Crystal

The general description of the pyroelectric detector used in the interferometer has been described in Section 3.3. The sensor (Molectron P1-65) is made of a 100 μm thick $LiTaO_3$ pyroelectric crystal. The P1-65 has a metallic coating containing chromium applied to the front surface of the crystal to increase the response time. The metallic coating is partially reflecting, partially transmitting and partially absorbing over a broad spectral range from 0.1 to 1 μm [19]. Since the coating is metal and is in intimate contact with the crystal, heat transfer occurs on the order of picosecond. The rear surface is also coated with a chromium layer and a heavy layer of gold which absorbs radiation through the visible region to 1 μm [27]. The schematic diagram in Figure 5.5(a) shows the structures of the pyroelectric sensor.

For far-infrared radiation, such as our radiation pulses, a fraction of radiation at the front surface is either reflected, absorbed, or preferably transmitted through the chromium coating. Part of the transmitted radiation may later be reflected by the gold layer at the rear surface. The schematic diagram in Figure 5.5(b) illustrates the absorption and reflection mechanism. At unequal optical path lengths in the interferometer, part of the radiation from one arm is reflected on the rear surface of the crystal and travels toward the front surface. This reflected radiation can interfere with the radiation coming later from the longer arm of the interferometer. This leads to either an increased or decreased signal at the detector as evident from the

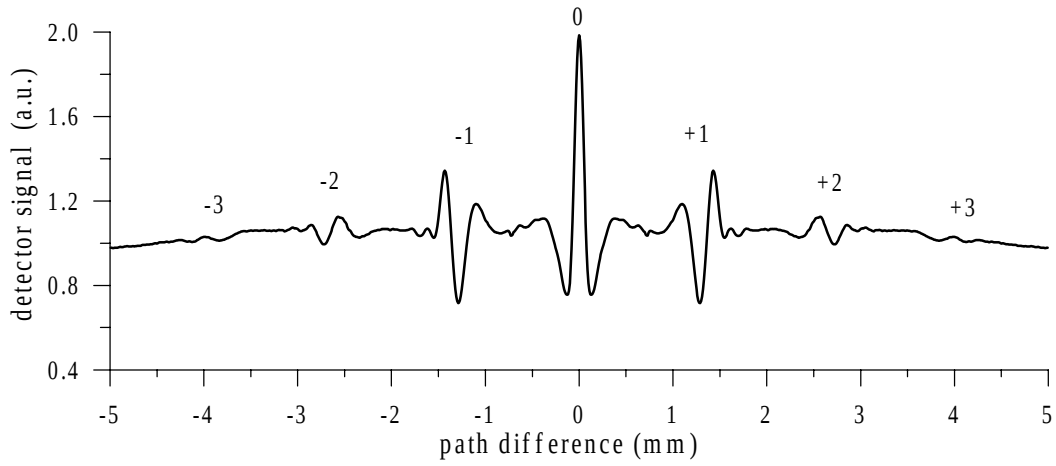

Figure 5.6: The interferogram showing multiple reflections in the pyroelectric sensor.

signatures in the interferogram. The following along with Figure 5.6 and Figure 5.7 will describe these signatures.

In Figure 5.6, the main peak (signature 0) is the result of the autocorrelation of the radiation pulse while the other signatures are cross-correlations of the radiation pulse and reflected pulses. The schematic diagram in Figure 5.7 shows how these signatures occur. The diagram in Figure 5.7(a) demonstrates a situation for zero path difference giving an autocorrelation as a consequence. Cross-correlation can occurs when a radiation pulse from one arm is reflected on the rear surface of the sensor and then interferes with the radiation pulse coming from the longer arm. The signature +1 and the signature -1 illustrate the cross-correlation. Figure 5.7(b) shows cross-correlation of the reflected radiation from the movable mirror yielding the signature +1. Similarly, Figure 5.7(c) shows cross-correlation of the reflected radiation from the fixed mirror causing the signature -1. Evidence of the signature +2 , signature +3, signature -2, and signature -3 confirm that multiple reflections within the detector crystal can occur.

The locations of the signatures in the interferogram depend on the thickness and the refractive index of the pyroelectric crystal. The centers of the signatures +1 and -1 are located at the distance $d = 2t\ \bar{n}$ from the main peak, where t is the thickness of the crystal and $\bar{n}$ is the average refractive index. From the interferogram,

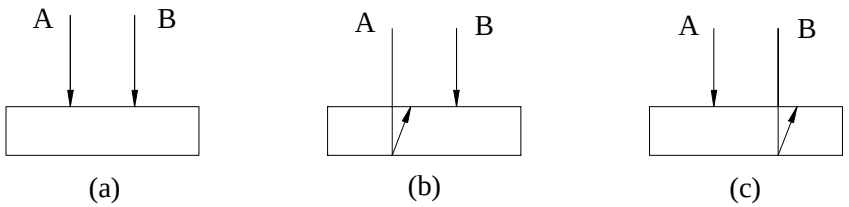

Figure 5.7: Demonstration for the signatures in the interferogram: (a) autocorrelation, (b) cross-correlation of the reflected pulse from the movable mirror, and (c) cross-correlation of the reflected pulse from the fixed mirror.

we find $d = 1.37$ mm given an average refractive index of the $LiTaO_3$ crystal $\bar{n} = 6.85$. Similar estimations can be made using the other signatures with the proper travelling distances. Alternatively, the average refractive index can be estimated from the spectral response. The period of the spectral response (Figure 5.4) averaged over 8 minima is 7.35 cm^{-1} suggesting that the average refractive index of the detector crystal is 6.80. The feature in the frequency response, however, is not perfectly periodic with a constant frequency interval which indicates a small dispersion in the crystal. By further analyzing the interferogram signatures, it is possible for us to calculate the refractive index of the detector crystal as a function of frequency using the Dispersive Fourier Transform Spectroscopy (DFTS) technique. More details of this study will be present in Chapter 8.

To support the above model of multiple reflections in the detector crystal, we compare the interferogram taken by a Molectron P1-62 which is constructed in a similar way as the Molectron P1-65 but the pyroelectric crystal is only 25 μm thick. This P1-62 sensor has an absorption area of 2 mm diameter and is manufactured as a test version by the manufacturer. Due to some alignment difficulty, this measurement is performed in a Michelson interferometer set up in air. The interferograms taken from both detector are compared in Figure 5.8 while their spectra are shown in Figure 5.9. The signature +1 and -1, which are the cross-correlation of the reflected radiation pulses, move closer to the main peak when using the P1-62 sensor. This is as expected

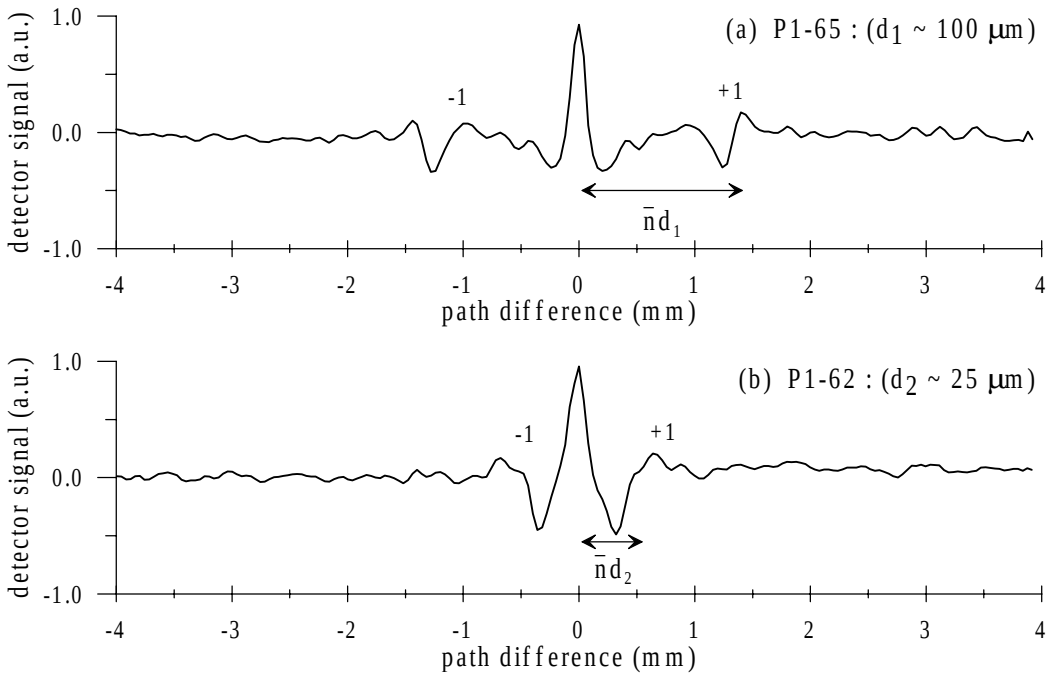

Figure 5.8: Interferograms taken by (a) P1-65 detector with a 100 μm thick pyroelectric crystal and (b) P1-62 with a 25 μm thick pyroelectric crystal.

when a thinner detector crystal is used since the reflected radiation pulses travel a smaller distance in the crystal. From the thicknesses of both detector crystals, the distance between the signature +1 and the main peak in the interferogram taken by the detector P1-62 should be a quarter of that observed with the detector P1-65 (if the thickness specification is precise). Note that many ripples shown in the baselines of both interferogram are the outcome of water vapor absorption. As for the spectrums, the frequency interval in the frequency response for P1-62 is larger than that of P1-65. Some water absorption lines are observable in the spectrums. Since the resolution of the spectrums are limited by the total length of the interferogram, the absorption lines visible here are not as clear.

Multiple reflections in the pyroelectric detector crystal results in signatures of cross-correlation in the interferogram. As long as the cross-correlation signatures do not merge into the main peak, the pyroelectric detector, such as the P1-65 detector, can be used for the autocorrelation bunch length measurement. It is also clear that

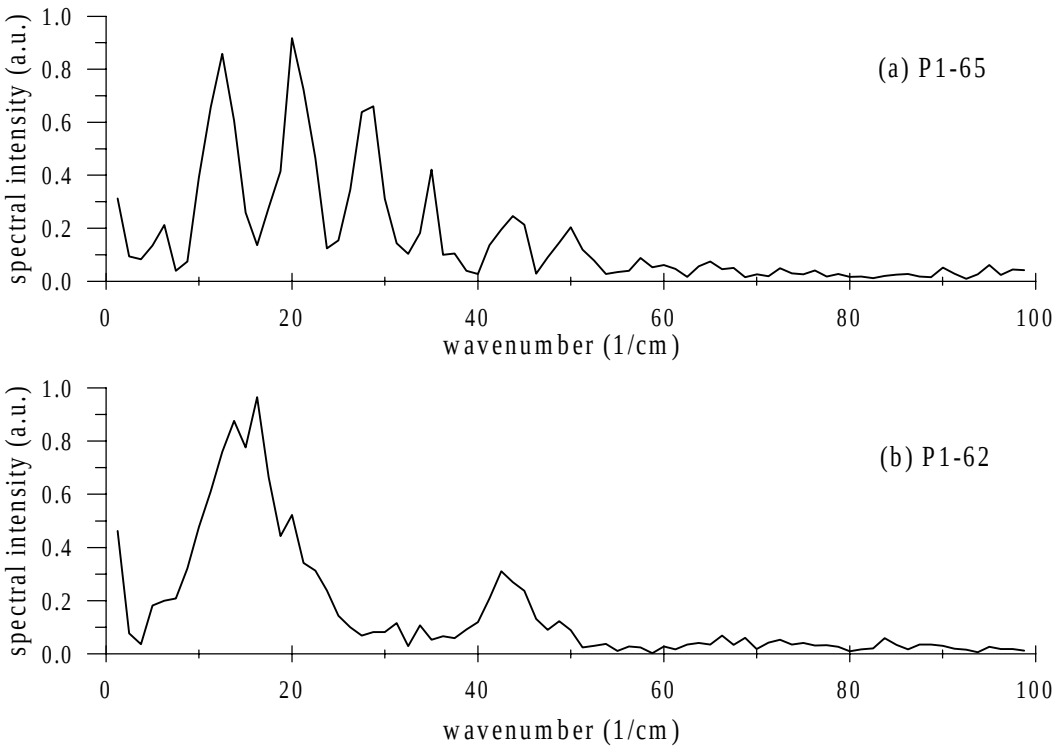

Figure 5.9: Spectral intensity obtained from (a) P1-65 and (b) P1-62 detector.

the bunch length information is contained in the main peak of the interferogram which is an autocorrelation of the coherent transition radiation. Therefore a short interferogram including only the main peak and the clear base-line level gives sufficient information for bunch length measurements.

5.4.2 Dispersion in Humid Air

To study effects of humidity in ambient air on the bunch length measurement, we compare interferograms taken in air and in vacuum. After taking bunch length measurements in vacuum, the interferometer is opened up to the atmospheric environment. The measurements in air are then taken. Interferograms for both cases are shown in Figure 5.10, displaying the increase of the interferogram width for the measurement in the air. The average FWHM of the interferograms measured in vacuum

measurement	**FWHM** (μm)	**corrected FWHM** (μm)
in vacuum	87 ± 2	126 ± 4
in ambient air	101 ± 3	158 ± 6

Table 5.1: The average FWHMs of the interferograms taken in vacuum and in ambient air with and without corrections for 1 mil beam splitter and mirror diffraction .

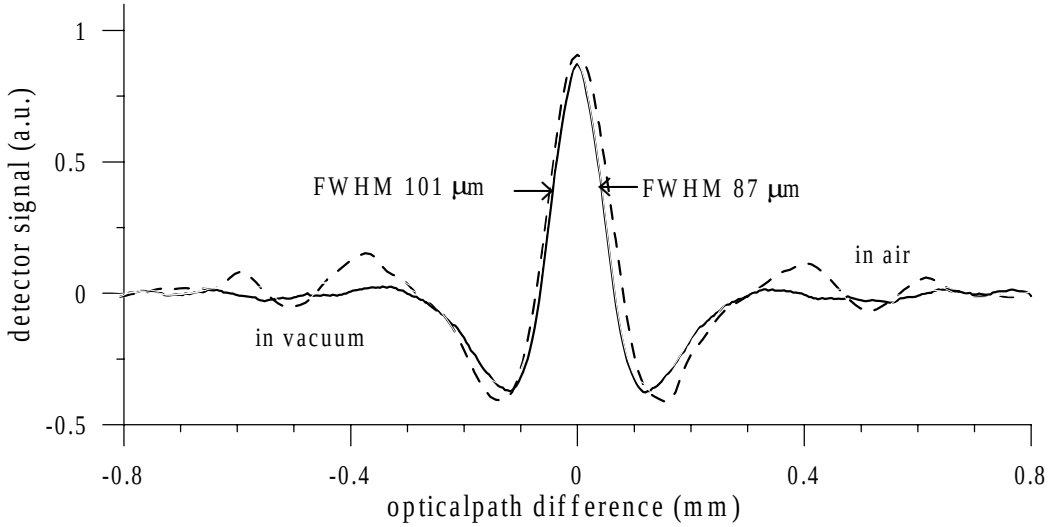

Figure 5.10: Comparison of the interferograms taken in vacuum (solid) and in humid air (dash-line).

is 87 ± 2 μm while the measurements in the air give an average FWHM of 101 ± 3 μm. Note that the deviations shown here are due to statistical errors. In general, the resolution of the bunch length measurement is determined by the step size which is 5 μm in this measurement. Applying the correction from low frequency suppression discussed in Section 5.3, the corrected bunch lengths for both measurements can be obtained and are shown in Table 5.1. The corrected FWHM for the measurement in vacuum is 126 μm, while that of the measurement in the air is 158 mm, which is 32 μm larger than that taken in vacuum. This broadening can be explained by dispersion due to water vapor in humid air. Since the refractive index of humid air is not constant over the far-infrared regime, different frequencies propagate with different

velocities. Consequently, the radiation pulse is spreading, as it travels through the air.

Variation of propagation velocities and pulse spreading can be related by

$$\frac{\Delta v_g}{\langle v_g \rangle} = \frac{\Delta l}{s}, \tag{5.6}$$

where Δl is the increase of the pulse length as the radiation pulse is travelling a distance s in air, Δv_g is the variation of the group velocity, and $\langle v_g \rangle$ is the average group velocity within the radiation spectral range. From the measurement, the pulse spreads from 126 μm to 158

μm after travelling 80 cm in humid air. Approximated by (5.6), the variation of group velocity contributed to the spreading should be in the order of

$$\frac{\Delta v_g}{\langle v_g \rangle} = \frac{\Delta l}{s} = \frac{(158 - 126)\ \mu\text{m}}{80\ \text{cm}} = 4 \times 10^{-5}.$$

To estimate the variation of the group velocity, we first consider the group velocity $v_g = \mathrm{d}\omega/\mathrm{d}k$ which can be written as [28]

$$v_g = \frac{c}{n(\omega)} \left[1 + \frac{\omega}{n(\omega)} \frac{\mathrm{d}n}{\mathrm{d}\omega} \right]^{-1}, \tag{5.7}$$

where $n(\omega)$ is the refractive index of humid air and c is the speed of light in vacuum. The real refractive index of humid air at room temperature and 1.5 Torr partial pressure reproduced from [29] is shown in Figure 5.11. By knowing the refractive index of the air, the group velocity can now be estimated using (5.7) and is shown in Figure 5.12. Note that the variation of group velocity between the two dashed-lines is $\Delta v_g = 4 \times 10^{-5}$.

The variation of the group velocity in air (ignoring narrow absorption bands) is contained within the two-dashed lines, indicating that it is reasonable to describe the observed pulse spreading by dispersion in humid air. It is worth noticing that the pulse spreading depends on the radiation spectral range. For example, a long bunch generating coherent radiation within 17 cm^{-1} wavenumber will not be vulnerable to

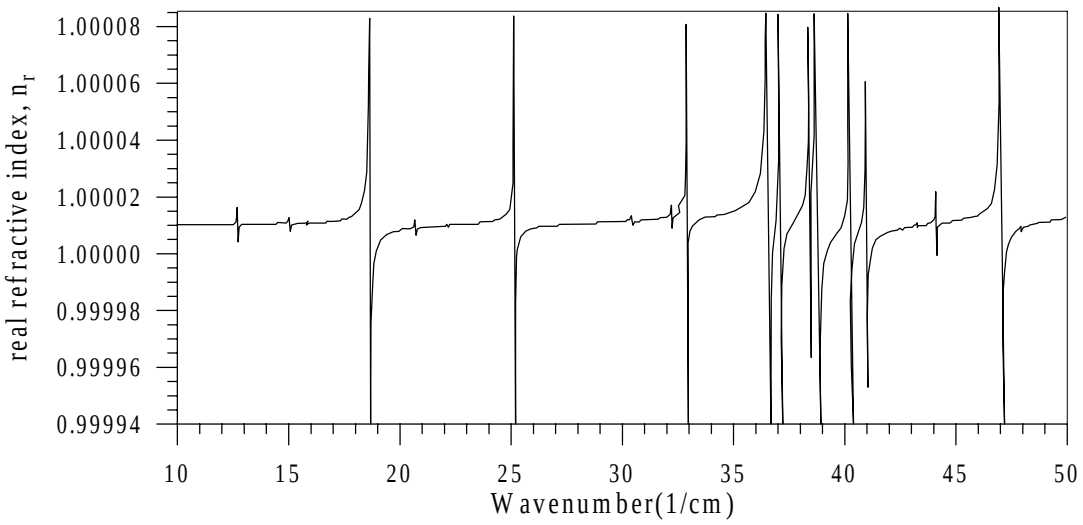

Figure 5.11: The real refractive index of air at room temperature and 1.5 Torr partial pressure [29] for the spectral range 10-50 cm^{-1}wavenumber.

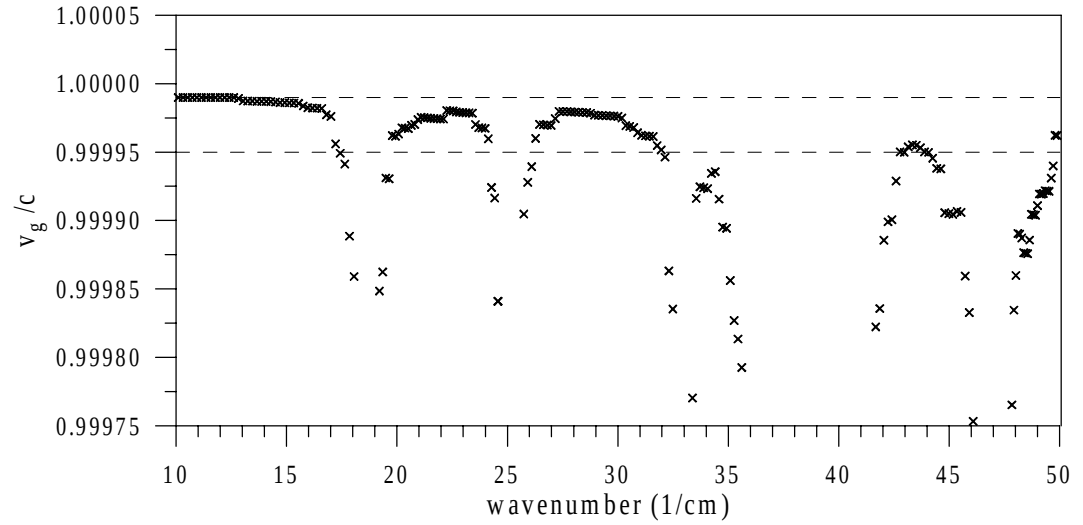

Figure 5.12: Group velocity v_g (unit of c) in humid air.

the dispersion since the group velocity variation within the radiation spectral range is very small. A very short bunch, on the other hand, generates a broad spectrum and is subjected to large pulse spreading when it traverses the humid air. In any case, to avoid the pulse spreading and for precise bunch length measurements, either the interferometer must be placed under vacuum or corrections must be applied.

5.5 Effects of Beam Size

The principle of the autocorrelation bunch length measurement is based on extracting the frequency information from the coherent radiation. Perturbations to the coherent radiation spectrum from the transverse distribution, therefore, disturbs the bunch length measurement. The effects of the beam size on the coherent radiation spectrum have been discussed in Section 4.7. In general, it is important to minimize the contribution of transverse distribution to fully obtain the coherent spectrum that is determined solely by the longitudinal particle distribution.

The experiment to investigate effects of the beam size on the bunch length measurement has been conducted in a similar way as the study of the beam size and coherent radiation properties (Section 4.7). In this experiment, the bunch lengths are measured as a function of the beam size. The beam size is varied using a pair of quadrupole magnets located 60 cm upstream from the radiator and is measured by analyzing an image of the beam on the fluorescent screen mounted behind the radiator. The image of the beam is analyzed to give horizontal and vertical beam profiles. Details of the beam profile monitor setup and its analysis are described in section 3.1.2. Interferograms of the coherent transition radiation, generated from the electron beams focused to different beam sizes, are recorded using the in-vacuum Michelson interferometer. The FWHM of each interferogram gives us a measured value σ_m associated with each beam size in the measurement. The beam size is represented by the effective beam width σ_ρ where $\frac{1}{2}(\sigma_x + \sigma_y) < \sigma_\rho < \sigma_y$ as discussed in Section 3.1.2.

The experimental results are shown in Figure 5.13 with the effective beam sizes bound between the two limits and the measured bunch lengths σ_m are within $\triangle\sigma_m \approx 3$

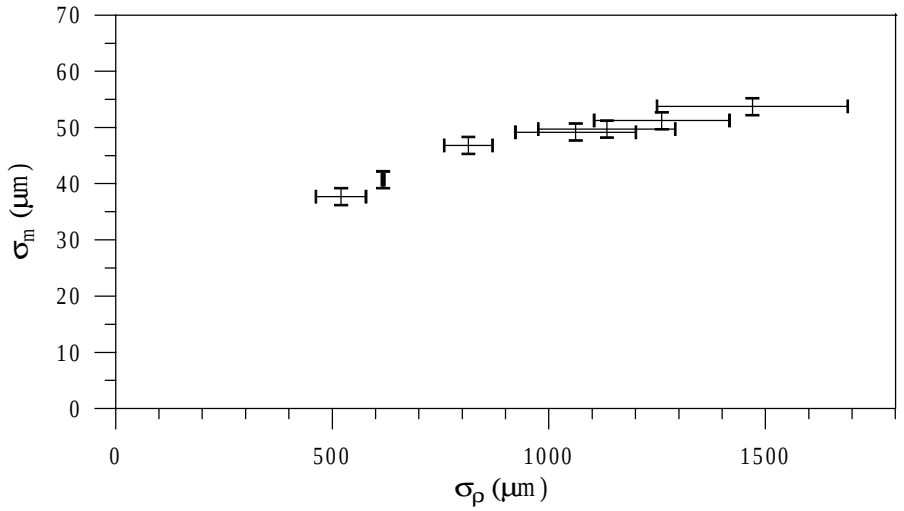

Figure 5.13: Measured bunch length σ_m as a function of beam size.

μm. As a beam size decreases, the measured bunch length becomes smaller. The measured values should approach the real bunch length when the beam size is small enough so that the contribution of the transverse distribution becomes negligible compared to that of the longitudinal distribution. The condition for this particular case for a Gaussian bunch is shown in (4.5) and has been discussed in Section 4.6. In our measurement, the beam sizes can not be focussed small enough to be in that regime. This focussing limitation is due to the energy droop along a macropulse, i.e. the beam size varies along the macropulse.

A theoretical comparison of the beam size effect can be obtained from the following consideration. The form factor of a Gaussian bunch, given in (4.4), yields the measured bunch length $\sigma_m(\theta)$ of

$$\sigma_m^2(\theta) = \sigma_z^2 \cos^2\theta + \sigma_\rho^2 \sin^2\theta, \tag{5.8}$$

where θ is the observation angle. In the measurement, the radiation is collected over the acceptance angle θ_a and thus the measured bunch length σ_m is the average over

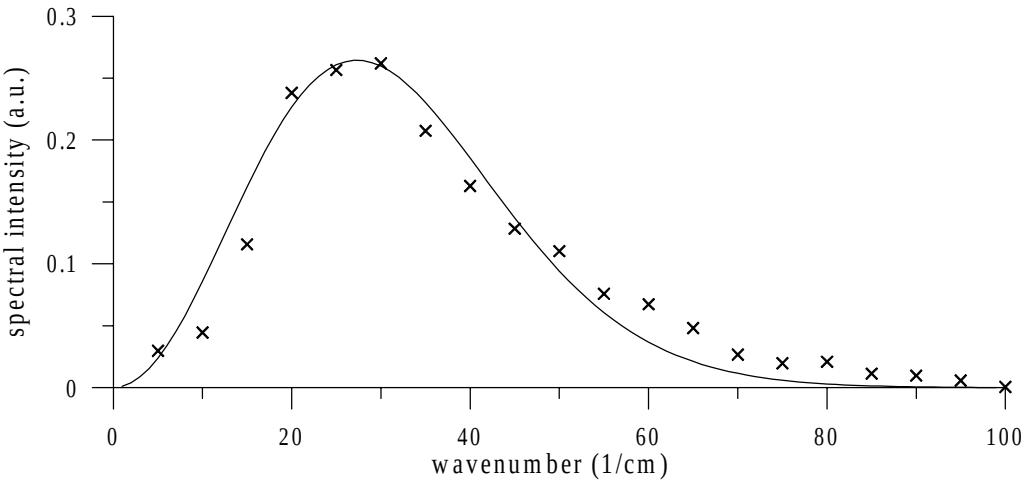

Figure 5.14: A simplified representation of the low frequency suppression by representing the spectral distribution with the function $\left[1-e^{-(2\pi p\nu)^2}\right]\left[e^{-(2\pi\sigma_z\nu)^2}\right]$ with $p = 50\ \mu$m (— : the function with $\sigma_z = 30\ \mu$m and $\times$: measured radiation spectrum).

all angles from zero to θ_a.

$$\sigma_m = \langle \sigma_m(\theta) \rangle_{\theta_a} = \frac{\int_0^{\theta_a} I_{cTR}(\theta)\,\sigma_m(\theta)\sin\theta \mathrm{d}\theta}{\int_0^{\theta_a} I_{cTR}(\theta)\sin\theta \mathrm{d}\theta}, \tag{5.9}$$

where $I_{cTR}(\theta)$ is the coherent transition radiation intensity observed at θ.

$$I_{cTR}(\theta) \propto \int_0^{\infty} |R(\omega)T(\omega)|^2\, M(\omega) e^{-(\omega\sigma_\rho \sin\theta/c)^2} e^{-(\omega\sigma_z\cos\theta/c)^2} \frac{\sin^2\theta}{(1-\beta^2\cos^2\theta)^2} d\omega. \tag{5.10}$$

The function $|R(\omega)T(\omega)|^2$ and $M(\omega)$ describe the low frequency suppression of the beam splitter and of the mirror diffraction in the Michelson interferometer. For simplicity, we fit the low frequency spectrum to the function $\left[1-e^{-(p\omega/c)^2}\right]$ where p is the fitting parameter. Figure 5.14 shows the function $\left[1-e^{-(2\pi p\nu)^2}\right]\left[e^{-(2\pi\sigma_z\nu)^2}\right]$, where $\nu = \omega/2\pi c$, fitted to a measured radiation spectrum obtained from the in-vacuum Michelson interferometer. The best fit for the low frequency suppression can be achieved with the fitting parameter $p = 50\ \mu$m. The high frequency roll

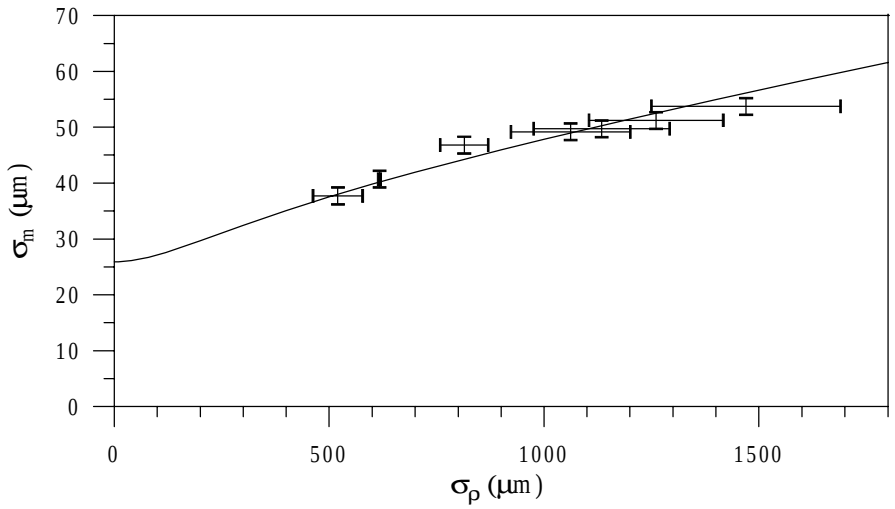

Figure 5.15: Bunch length σ_m as a function of beam size (— : theoretical estimate) .

off associated with the form factor is not of concern at this point since it will be determined by the measurement parameters. A more practical expression of (5.10) becomes

$$\begin{aligned} I_{cTR}(\theta) &= \int_0^\infty \left[1 - e^{-(\omega p/c)^2}\right] e^{-(\omega\sigma_\rho \sin\theta/c)^2} e^{-(\omega\sigma_z \cos\theta/c)^2} \frac{\sin^2\theta}{(1-\beta^2\cos^2\theta)^2} d\omega \\ &= \frac{c\sqrt{\pi}}{2} \frac{\sin^2\theta}{(1-\beta^2\cos^2\theta)^2} \left[\frac{1}{y} - \frac{1}{\sqrt{p^2+y^2}}\right], \end{aligned} \tag{5.11}$$

where $y^2 = \sigma_\rho^2 \sin^2\theta + \sigma_z^2 \cos^2\theta$. The $\langle\sigma_m(\theta)\rangle$ in (5.9) can now be evaluated.

The value of $\sigma_m = \langle\sigma_m(\theta)\rangle_{\theta_a}$ as a function of σ_ρ is evaluated for the transition radiation generated by a 26 MeV monochromatic beam, collected over the acceptance angle of ± 160 mrad. The calculation is fitted to the measurement and both results are shown in Figure 5.15. The trend in the experimental results and the calculation suggest that the bunch length σ_z is about 26 μm. For a precise bunch length measurement, it is important to focus the beam well to achieve a small beam size at the radiator so that the transverse distribution is negligible. Bunch length measurement as a function of beam size, similar to what has been done in this experiment, can be

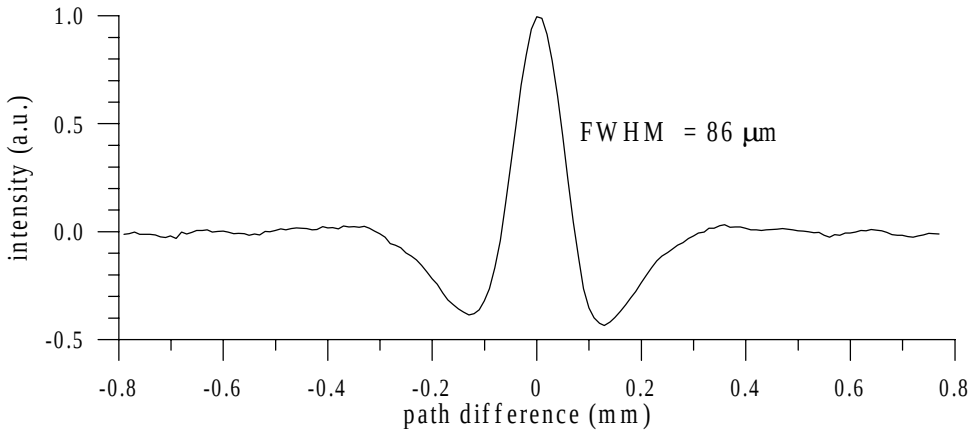

Figure 5.16: A measured interferogram for bunch length measurement.

used to separate longitudinal and transverse contribution for more accurate estimate of the bunch length.

5.6 Pulse Reconstruction

The width of the interferogram peak resembles the bunch length, yet, the particle distribution is not well defined in this frequency domain observation. However, particular features of an interferogram correlate with features of the particle distribution. For example, a triangular interferogram is expected from an autocorrelation of a rectangular pulse and a Gaussian interferogram corresponds to a Gaussian pulse. This gives us some indications about the particle distribution. More information of the distribution can be obtained by fitting the measured radiation spectrum to that of a known distribution.

Figure 5.16 shows a measured interferogram with a FWHM of 86 μm. From the interferogram, the bunch distribution is unlikely to be a rectangular bunch since the interferogram differs from triangular which is that expected from a rectangular bunch. After applying corrections for the low frequency suppression from the beam splitter and mirror diffraction, the corrected FWHM of the interferogram is 126 μm for a Gaussian bunch. To obtain more information on the bunch distribution we fit the

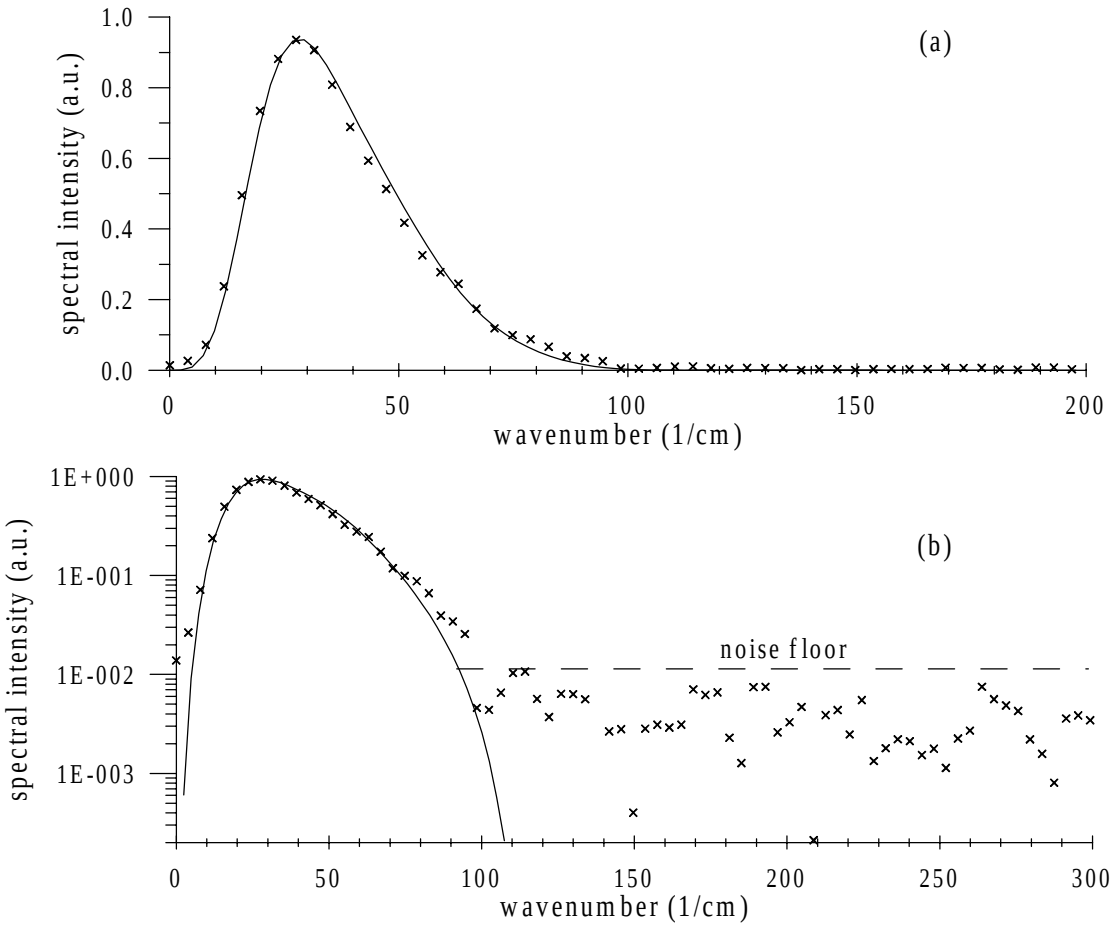

Figure 5.17: Measured power spectrum (a) in linear scale and (b) in logarithmic scale together with power spectrum of a Gaussain pulse ($\sigma_z = 38$ μm) shown in solid.

radiation power spectrum to the spectrum of a Gaussian bunch. Figure 5.17 shows the spectrum fitting in both linear and semilogarithmic scales. The best fit is achieved with a Gaussian distribution bunch with $\sigma_z = 38$ μm giving $4\sqrt{\ln 2}\sigma_z = 126.5$ which agrees with the corrected FWHM from the interferogram. Note that the calculated spectrum includes the beam splitter interferences and the mirror diffraction. The spectrum plotted on a linear scale shows the over all fit of the spectrum while that shown on a semilog scale gives a clearer image of the spectral distribution when the radiation intensity falls off. In Figure 5.17(b), the power spectrum at the detectable level covers two order of magnitude in the intensity. The noise floor is also shown

in the figure. The spectrum fit displayed on the semilog scale show some deviations from being a pure Gaussian bunch.

It is important to point out that in the autocorrelation bunch length measurement technique, the interferogram is the average results for all microbunches in many macropulses. This is so because of the long time constant (ms) of the detector system and because a full auto correlation scan continues over a time span of minutes. Therefore, the measured bunch length is an average bunch length. Since we know that the bunch length varies due to the energy droop along the macropulse, we cannot be certain that the radiation spectrum represents the particle distribution of a single microbunch.

5.6.1 Kramers-Kronig Pulse Reconstruction

Pulse reconstruction can be carried out using Kramers-Kronig analysis [30]. An asymmetry in the particle distribution is included by expressing the Fourier spectrum of a general distribution as

$$\tilde{E}(\omega) = A(\omega)\, e^{i\phi(\omega)}. \tag{5.12}$$

While the phase $\phi(\omega)$ is lost in autocorrelation, it may be calculated from Kramers-Kronig relation.

$$\phi(\omega) = \frac{-2\omega}{\pi} \int_0^\infty \frac{\ln\left[A(\omega')/A(\omega)\right]}{\omega'^2 - \omega^2} \mathrm{d}\omega', \tag{5.13}$$

where the amplitude of Fourier spectrum $A(\omega)$ is obtained from the measured radiation power spectrum

$$A(\omega) = \sqrt{I_{cTR}(\omega)}. \tag{5.14}$$

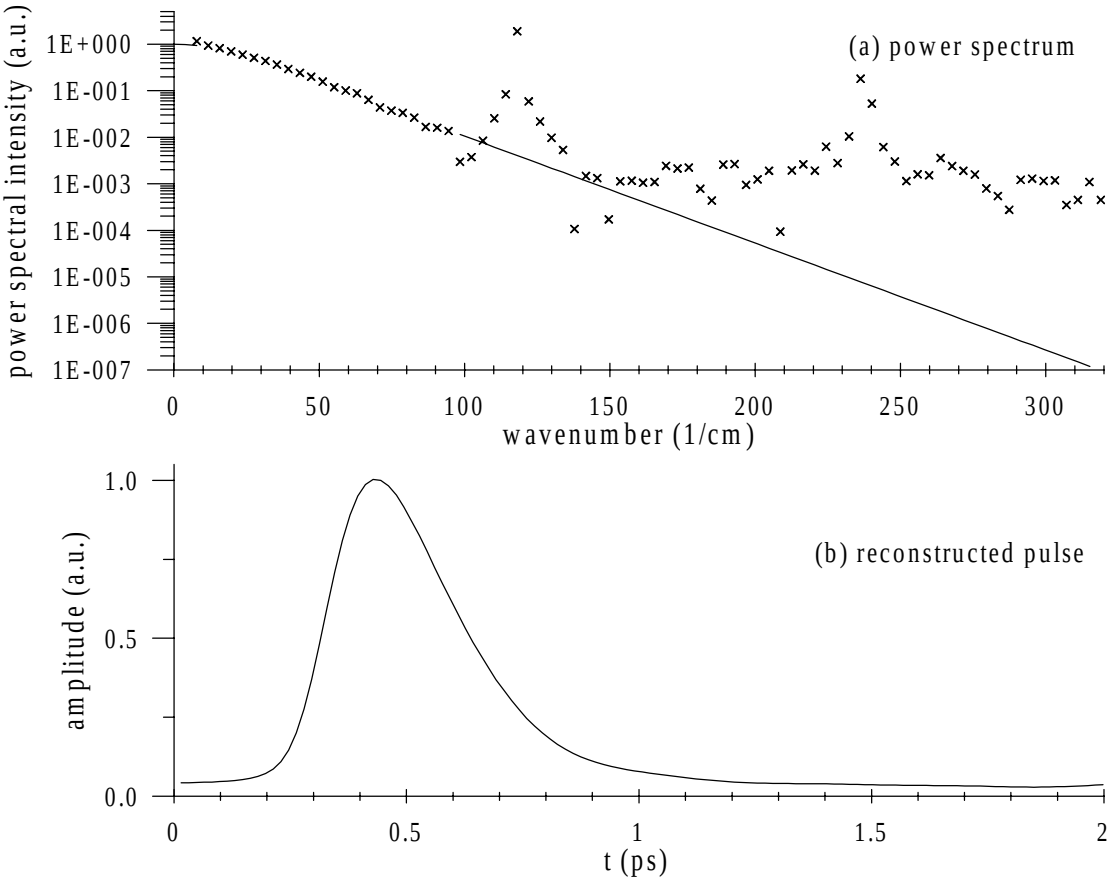

Figure 5.18: (a) corrected power spectrum and exponential extrapolation to high frequencies; and (b) Kramers-Kronig reconstructed pulse.

Here the radiation power spectrum $I_{cTR}(\omega)$ is just the Fourier transform of the measured interferogram. The particle distribution can then be reconstructed by

$$h(z) = \frac{1}{\pi c} \int_0^\infty A(\omega) \cos[\phi(\omega) - \omega z/c] \, d\omega. \tag{5.15}$$

Kramers-Kronig Reconstructed Pulse

In principle, the Kramers-Kronig analysis requires a known radiation spectrum from zero to infinite which is practically impossible. However, for femtosecond bunches at SUNSHINE the coherent spectrum covers quite a broad range and thus make

it possible for us to extrapolate the spectrum to zero and to high frequency with some confidence. Figure 5.18(a) shows the corrected spectrum and high frequency extrapolation using the exponential function. The reconstructed pulse is computed by (5.13) − (5.15) and is shown in Figure 5.18(b) suggesting an asymmetric pulse with a tail. However, we believe Kramers-Kronig analysis can only unambiguously reconstruct certain classes of distribution from the power spectrum. Therefore, the result shown in 5.18(b) is, therefore, just one possibility of the pulse shape. Pulse reconstruction simulations using Kramers-Kronig analysis for some pulse distributions will be discussed in the next section demonstrating the limitations of the Kramers-Kronig analysis.

Pulse Reconstruction Simulation

The following are results of pulse reconstruction simulations using the algorithm based on the Kramers-Kronig analysis with some pulse distributions constructed from two Gaussian pulses.

Simulation #1 The original pulse is composed of two Gaussian pulses with the same width, different amplitudes, and different centroids with the larger pulse ahead. The longitudinal pulse distribution can be expressed as

$$f(z) = e^{-\frac{1}{2}\left(\frac{z}{\sigma_1}\right)^2} + \frac{1}{2}e^{-\frac{1}{2}\left(\frac{z-2.5\sigma_1}{\sigma_1}\right)^2},$$

where $\sigma_1 = 30$ μm. The pulse shape, simulated interferogram, power spectrum and the reconstruction pulse are shown in Figure 5.19. The reconstruction successfully recovers the original pulse shape.

Simulation #2 The original pulse is composed of two Gaussian pulses with the same width, different amplitudes, but now the weaker Gaussian leads (Figure 5.20(a)). The longitudinal pulse distribution can be expressed as

$$f(z) = e^{-\frac{1}{2}\left(\frac{z}{\sigma_1}\right)^2} + \frac{1}{2}e^{-\frac{1}{2}\left(\frac{z+2.5\sigma_1}{\sigma_1}\right)^2},$$

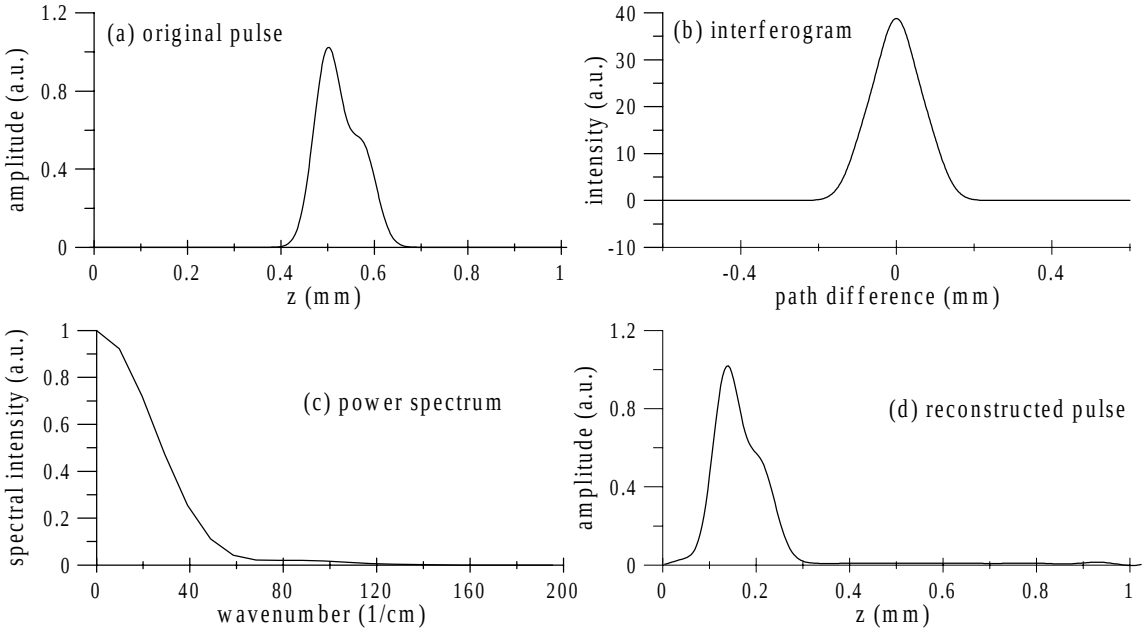

Figure 5.19: Pulse reconstruction simulation #1.

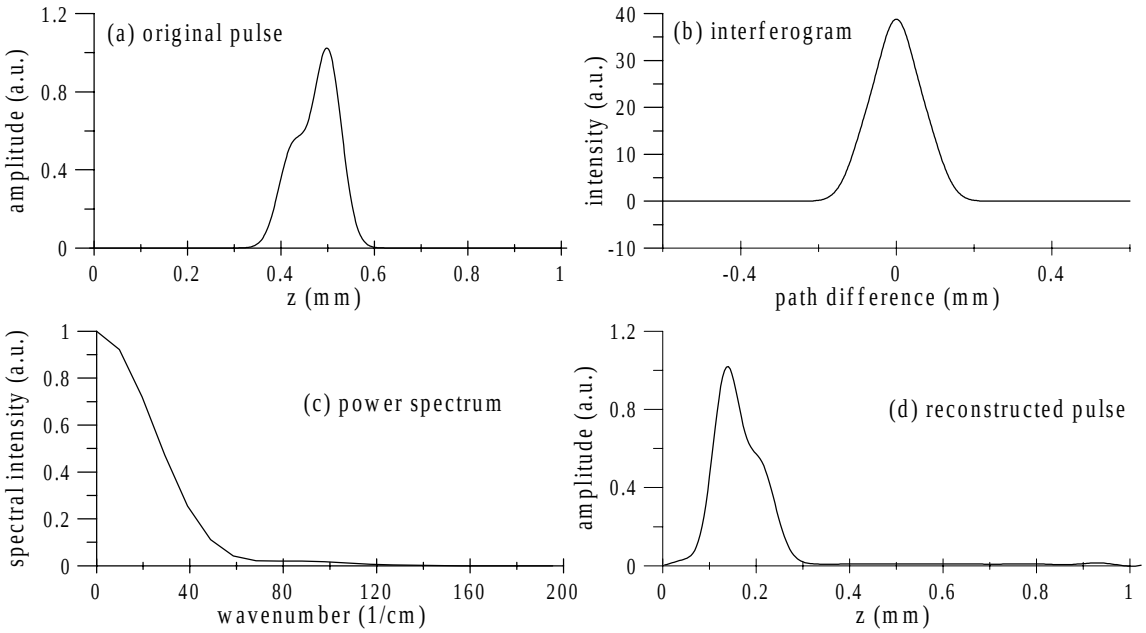

Figure 5.20: Pulse reconstruction simulation #2.

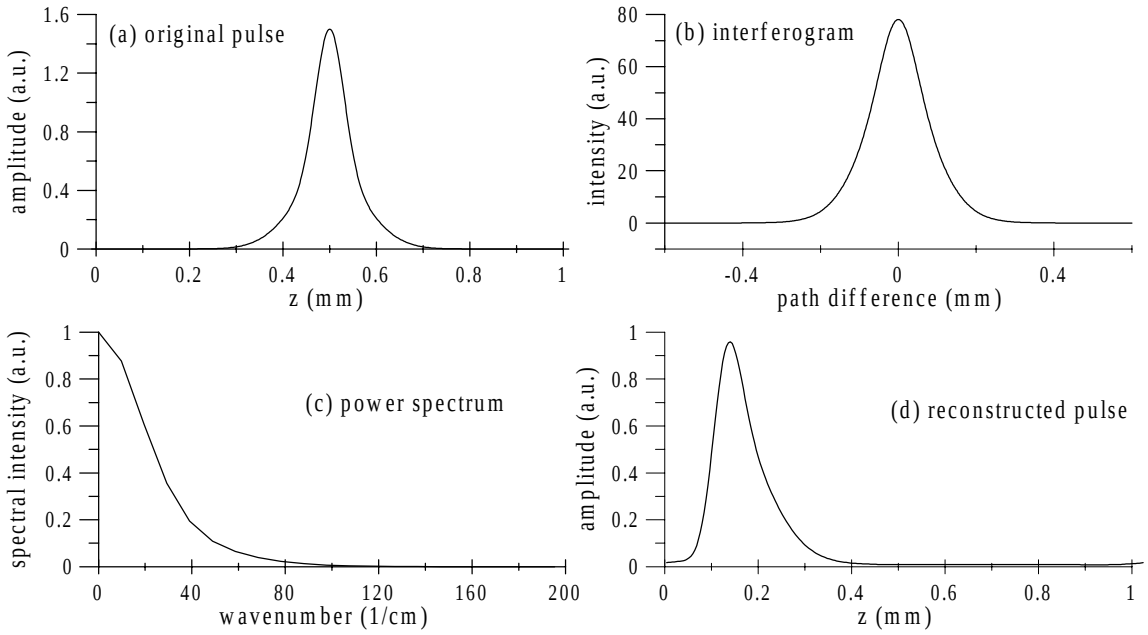

Figure 5.21: Pulse reconstruction simulation #3.

where $\sigma_1 = 30$ μm. The original pulse in this case is just a mirror image of the previous simulation. The original pulse distribution and simulated results are shown in Figure 5.20. The reconstructed pulse features the stronger Gaussian leading which is completely the opposite of the original pulse.

Simulation #3 The original pulse is composed of two Gaussian pulses with the different widths, different amplitudes, but the same center position. The longitudinal pulse distribution can be expressed as

$$f(z) = e^{-\frac{1}{2}\left(\frac{z}{\sigma_1}\right)^2} + \frac{1}{2}e^{-\frac{1}{2}\left(\frac{z}{2\sigma_1}\right)^2},$$

where $\sigma_1 = 30$ μm. This original pulse distribution is in fact a symmetric one. The reconstruction simulation shown in Figure 5.21, however, retrieves an asymmetric pulse featuring a tail structure.

The simulations show that unique pulse reconstruction based on Kramers-Kronig analysis is not possible. The analysis preferably retrieves an asymmetric pulse having

a leading higher amplitude followed by a tail. This analysis, therefore, cannot fully retrieve the phase nor reconstruct the pulse with out any ambiguity.

5.6.2 Other Phase-retrieval Methods

There are other techniques that have been developed to resolve the actual shape of ultrashort pulses. The goal of these techniques is to extract the phase information that cannot be obtained from autocorrelation measurement. Phase information can be obtained from two or more measurements, of which one is the autocorrelation measurement and the others are cross-correlation of a pulse after propagating through known dispersive mediums [31, 32, 33]. More sophisticated techniques which can determine amplitude and phase of a pulse without significant ambiguity are, for example, Frequency Domain Phase Measurement (FDPM) [34] and Frequency Resolved Optical Gating (FROG) [35]. FDPM employs a spectral filter technique and cross-correlation to obtain phase information of a particular frequency component of a pulse. FROG measures the spectrum of a particular temporal component of the pulse through a nonlinear-optical effect. In general, these methods require the availability of dispersive materials or nonlinear effects in the frequency range of interest. To implement such phase-retrieval methods for the bunch length measurement based on coherent transition radiation in far-infrared, suitable dispersive materials must be available. So far no such materials could be identified.

Chapter 6

Coherent Diffraction Radiation (DR)

Diffraction radiation (DR) is emitted when a charged particle travels in the neighborhood of some inhomogeneity. Specifically, the radiation can be generated when an electron travels past a metallic structure such as a transition in beam line cross sections. The theory of diffraction radiation was developed in the late 1950's [36, 37, 38, 11], examining charged particles passing through simple structures including circular apertures and slits. In 1995, Ref. [39] reported the first observation of coherent diffraction radiation in the millimeter and submillimeter wave region. The diffraction radiation was generated from a 150 MeV beam passing through a circular opening or iris. The experiment was set to observe the forward diffraction radiation and used a mirror to deflect the diffraction radiation to the observer. The mirror was in the path of the electron beam and acted as a radiator of transition radiation. The observed radiation was then the superposition of diffraction radiation and transition radiation.

In our experiments, we use backward radiation to avoid this superposition. The backward diffraction radiation from a circular opening can be observed by rotating the iris 45° with respect to the beam trajectory. Since the electron trajectories are not disturbed passing through the opening, it is then possible to generate diffraction radiation at several experimental stations as the beam is travelling along the beam line. This makes coherent diffraction radiation of great interest for nondestructive

bunch length measurements using the autocorrelation technique. In this chapter, we present the observation of coherent diffraction radiation at SUNSHINE and discuss the autocorrelation bunch length measurement based on coherent diffraction radiation.

6.1 DR from a Circular Aperture

The radiation intensity emitted from an electron moving with velocity $\mathbf{v}$ passing through a circular aperture radius r in an ideal conducting screen can be expressed as [39]

$$I_{DR}(\omega) = I_{TR}(\omega) D(\omega), \tag{6.1}$$

where $I_{TR}(\omega)$ is the spectral intensity of transition radiation and $D(\omega)$ is the correction for diffraction radiation.

$$D(\omega) = \left[\mathrm{J}_0\left(\frac{\omega r}{c}\sin\theta\right) \left(\frac{\omega r}{c\beta\gamma}\right) \mathrm{K}_1\left(\frac{\omega r}{c\beta\gamma}\right) \right]^2. \tag{6.2}$$

Here, θ is the observation angle with respect to the beam axis, $\boldsymbol{\beta} = \mathbf{v}/c$, γ is the Lorentz factor, J_0 is the Bessel function of the zeroth order and K_1 is the modified Bessel function of the first order. For the backward diffraction radiation the angle θ is the angle between the radiation direction and $-\mathbf{v}$. The radiated intensity approaches that of the transition radiation when the aperture decreases ($r \to 0$).

6.2 Coherent DR at SUNSHINE

The diffraction radiation is generated by a 26 MeV electron beam moving past a circular aperture in a 1.5 mm thick aluminum plate. The schematic diagram of the setup is illustrated in Figure 6.1. Three aperture sizes, 1.5 mm, 3 mm and 5 mm in diameter, are available. The aperture size can be selected by moving the plate vertically to center the selected aperture on the beam trajectory. The Al-plate is

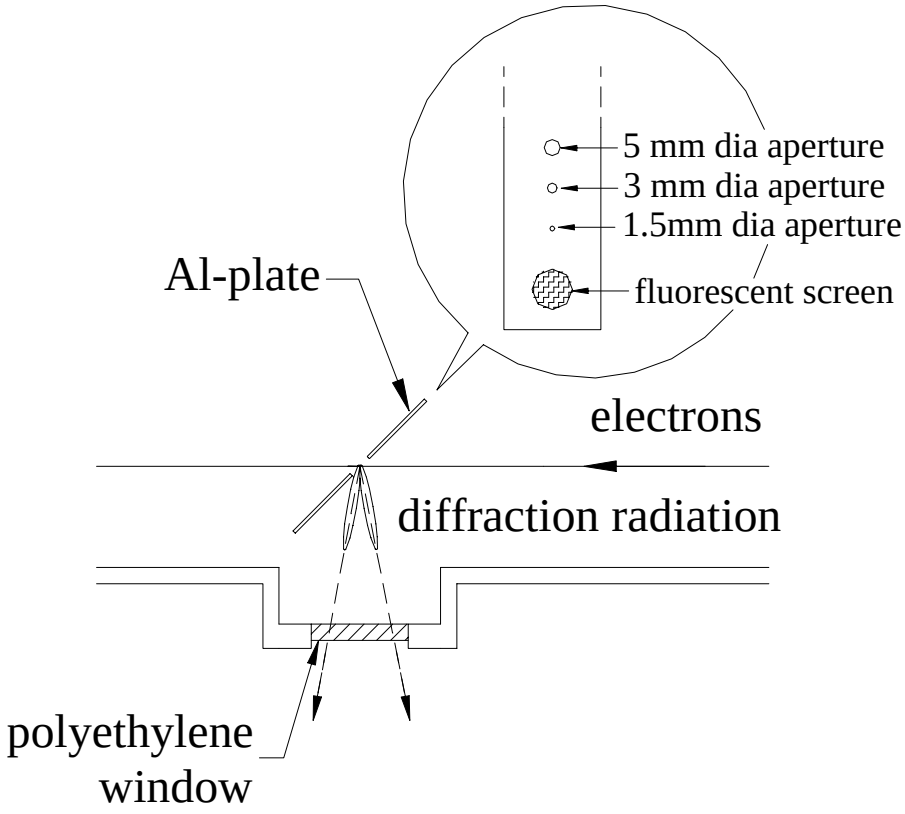

Figure 6.1: Schematic diagram of the setup to generate diffraction radiation. The target plate can be moved in the direction normal to the plane of the figure to selected different apertures.

tilted by 45° with respect to the beam path and the backward diffraction radiation, emitted at 90°, exits through a 19-mm-diameter and 1.25-mm-thick polyethylene window. Also available on the Al-plate is a fluorescent screen which can be selected to monitor the beam position. The beam profile is observed through a CCD camera (not being shown in the diagram) located on the opposite side of the polyethylene window. The beam is adjusted to pass through to the center of the screen by upstream steering magnets.

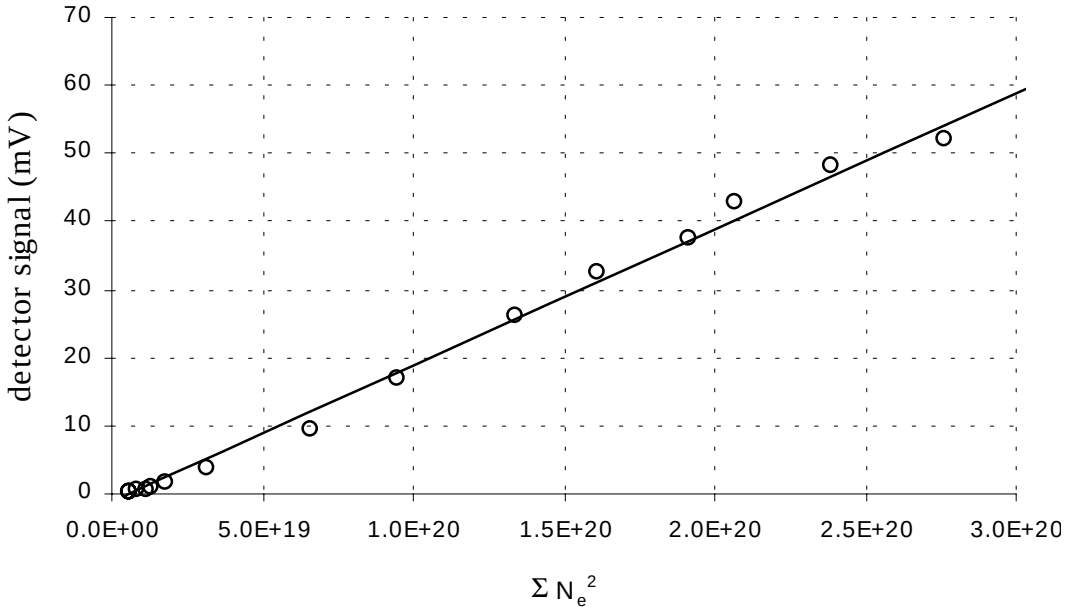

Figure 6.2: Diffraction radiation intensity as a function of the sum of number of electrons in each microbunch squared. The circular marks represent the measurement and the solid line represents a linear fit.

6.2.1 Coherent DR Intensity

Similar to the coherent transition radiation intensity, the intensity of coherent diffraction radiation is expected to scale with the square of the number of electrons. To verify the coherence of diffraction radiation generated at SUNSHINE, measurements have been conducted in a similar manner as described in Section 4.1. The diffraction radiation is generated using the 5-mm-diameter aperture which is the largest one available in the setup. Backward diffraction radiation is collected by a copper cone, with an acceptance angle of ± 120 mrad limited by the size of the window. The radiation intensity as a function of beam current is measured. The beam current is measured through toroid4 (T4) located just after the diffraction radiation experimental station. By closing the high energy slit in the alpha-magnet to scrape off some electrons, the beam current can be varied. The sum of the number of electrons squared $\sum N_e^2$ is determined using the method described in Section 4.1. The result

aperture diameter (mm)	normalized intensity	$\mathbf{T4}_{peak}$**(mA)**
0 (Al plate)	1	108
1.5	0.92	169
3.0	0.75	218
5.0	0.61	220
open	N/A	220

Table 6.1: Relative intensity of coherent transition radiation and coherent diffraction radiation form 1.5 mm, 3.0 mm, and 5.0 mm diameter apertures.

is shown in Figure 6.2 in which the radiation intensity scaling with $\sum N_e^2$ confirms the coherence of the diffraction radiation.

6.2.2 Intensity and Aperture Size

Using the same setup as shown in Figure 6.2, we investigate the diffraction radiation intensity generated from different aperture sizes. The radiation is collected over ± 120 mrad acceptance angle. Table 6.1 shows the intensity normalized to that of transition radiation for the radiation generated by different aperture sizes. The beam currents are recorded by T3 at the upstream location and by T4 located after the experimental station. The amount of beam current passing through T3 and T4 allows us to monitor whether parts of the electron beam have been intercepted by the Al-plate. The peak current at T3 is 259 mA while the peak current passing through T4 without any obstacle is 221 mA. The peak currents at T4 are also shown in the table to indicate whether the electron beam is intercepted by the apertures. For the case of 5-mm aperture, the electron beam passes through the aperture without significant interception. This is still true for the case of 3-mm aperture. However, the 1.5-mm aperture seems to intercept some of the electron beam.

The measurement shows that the collected radiation intensity decreases as the aperture size increases. To compute the theoretical intensity, we use (6.1) and the coherent radiation intensity shown in (2.4). For simplicity, we use the expression for transition radiation generated from normal incidence on a vacuum and perfect

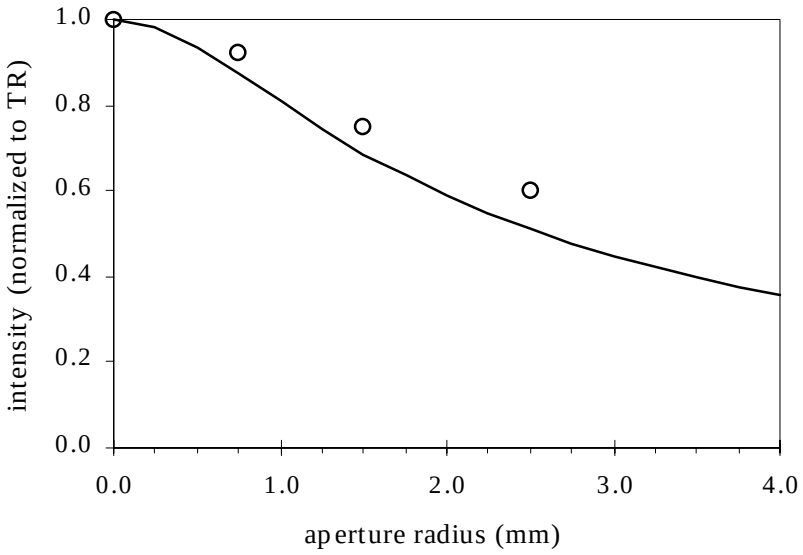

Figure 6.3: Normalized diffraction radiation intensity as a function of aperture radius (o : measurement and — : calculation).

conductor interface. The coherent diffraction radiation intensity can be expressed as

$$I_{cDR}(\omega,\theta) = N_b N_e^2 I_{DR}(\omega,\theta) f(\omega), \tag{6.3}$$

where N_b is the number of bunches, N_e is the number of electrons in each bunch, $I_{DR}(\omega)$ is diffraction radiation intensity defined in (6.1) , and $f(\omega)$ is the form factor which depends on the electron bunch distribution. The collected radiation within an observation angle θ_a can be obtained by integrating over the solid angle as

$$I_{cDR}(\omega,\theta_a) = N_b N_e^2 \int_0^{2\pi}\int_0^{\theta_a} \frac{e^2\beta^2\sin^2\theta}{\pi^2 c(1-\beta^2\cos^2\theta)^2} D(\omega) f(\omega)\sin\theta \mathrm{d}\theta\mathrm{d}\phi. \tag{6.4}$$

In the calculation, we use a monochromatic beam of 26 MeV with a Gaussian longitudinal distribution of $\sigma_z = 80$ μm. The parameter is obtained from the autocorrelation bunch length measurement. This measured bunch length is in fact the result of both longitudinal and transverse distribution which was described in Chapter 5. We

do not have enough information to separate the longitudinal and transverse distributions in this case. The calculation is therefore performed using only the longitudinal form factor with σ_z approximated from the bunch length measurement representing an effective bunch length. Note also that the bunch at the diffraction radiation experimental station is generally longer than the one at the transition radiation station since it is located further downstream in the beam line. With the limitation of our beam line transport system, it is turned out to be difficult to preserve the short bunch along a long beam line. The results of the calculation, normalized to those obtained for $D(\omega) = 1$, are shown in Figure 6.3 along with the measured values obtained for $D(\omega) = 1$. The measured intensity appears to be higher than the calculation. This discrepancy comes from the finite beam size. Even though the transverse distribution has been included in the form factor, the effects of a finite beam size has not been included in the distribution of diffraction radiation. The expression of $D(\omega)$ in (6.2) is valid for electrons moving past the center of the circular aperture. In reality, the electron beam has a finite width and some electrons are closer to the metallic boundary than the aperture radius as theoretically assumed.

6.2.3 Spectral Distribution

The frequency dependence of diffraction radiation intensity is shown in (6.1) and (6.2). The radiation intensity normalized to that of transition radiation is just the function $D(\omega)$ shown in (6.2). The spectral distributions of diffraction radiation for a 26 MeV beam at the observation angle $1/\gamma$, generated by 1 mm, 3 mm, and 5 mm diameter apertures, are presented in Figure 6.4. The high frequency components are suppressed by interference as the aperture size increases. It can be seen in the figure how the spectral distribution of diffraction radiation from a 26 MeV beam suffers from the high frequency suppression. This spectral distribution will limit the spectral range of coherent diffraction radiation that can be generated. The spectral distribution of a higher energy beam will be discussed later in this chapter.

The spectral distribution of coherent diffraction radiation generated by a 26 MeV beam at SUNSHINE is measured with a Michelson interferometer and is shown in

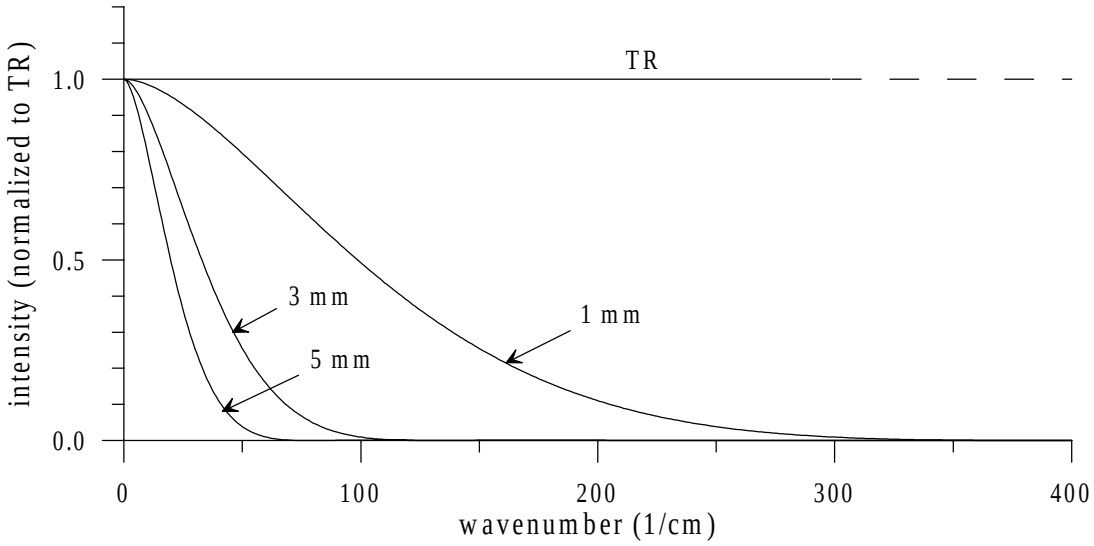

Figure 6.4: Normalized spectral intensity of diffraction radiation generated by a 26 MeV beam at 1.0 mm, 3.0 mm, and 5.0 mm apertures.

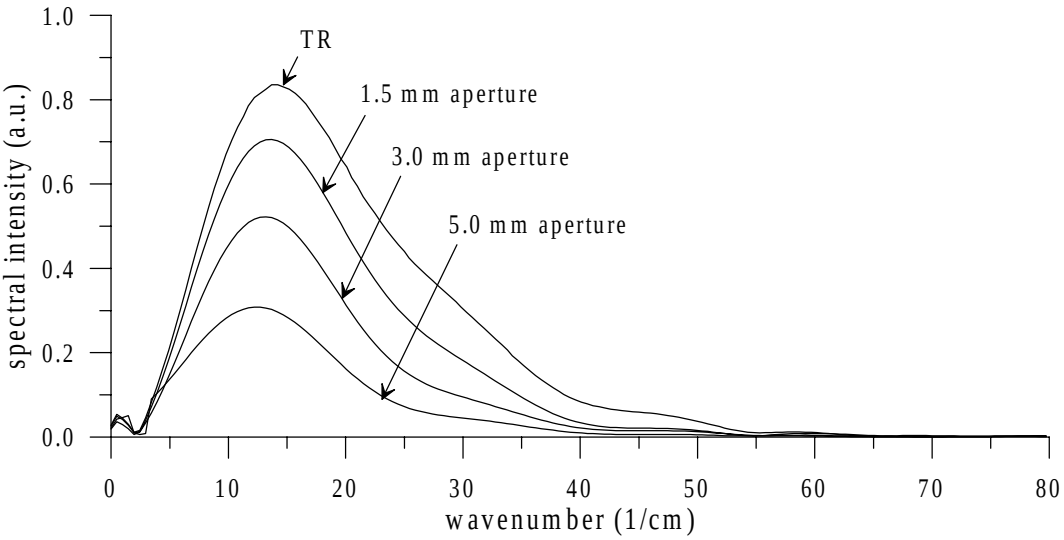

Figure 6.5: Spectal distribution of coherent transition radiation and coherent diffraction radiation generated by a 26 MeV beam st SUNSHINE.

Figure 6.5. The backward diffraction radiation is generated by the 1.5 mm, 3.0 mm, and 5.0 mm diameter apertures on an Al-plate while the backward transition radiation is generated by the vacuum-aluminum interface. The low frequency suppression in the spectrum is due to thin film interference effect in the 25-μm Kapton beam splitter which has been discussed in Chapter 3. The high frequency suppression is caused by the diffraction radiation spectral distribution expressed in (6.2) and it becomes more severe as the aperture size increases.

6.3 Bunch Length Measurement Using Coherent DR

The autocorrelation bunch length measurement technique, described in Chapter 5, retrieves frequency information of the bunch from the spectrum of coherent transition radiation. The coherent diffraction radiation generated by the electron bunch also carries such frequency information. Moreover, generation of coherent diffraction radiation can be done in a nondestructive way which is not possible for ordinary transition radiation. Desirable beam characteristics, like bunch length, are preserved and therefore the beam can be used again further downstream.

The spectral distribution of diffraction radiation, however, has a frequency dependence even for the case of an aperture in a perfect conductor. As shown in (6.1), the spectral distribution of diffraction radiation from a circular aperture depends on the aperture sizes and beam energy. To use coherent diffraction radiation in an autocorrelation bunch length measurement, we must consider this frequency dependence carefully.

The effects of the diffraction radiation spectral distribution on the interferograms can be demonstrated by simulations. We apply diffraction radiation spectral distribution to the power spectrum of a known bunch distribution and use inverse Fourier transformation to retrieve a simulated interferogram of diffraction radiation. Simulated interferograms of diffraction radiation from various aperture sizes are shown in Figure 6.6. The simulations are based on a Gaussian bunch of 26 MeV beam and

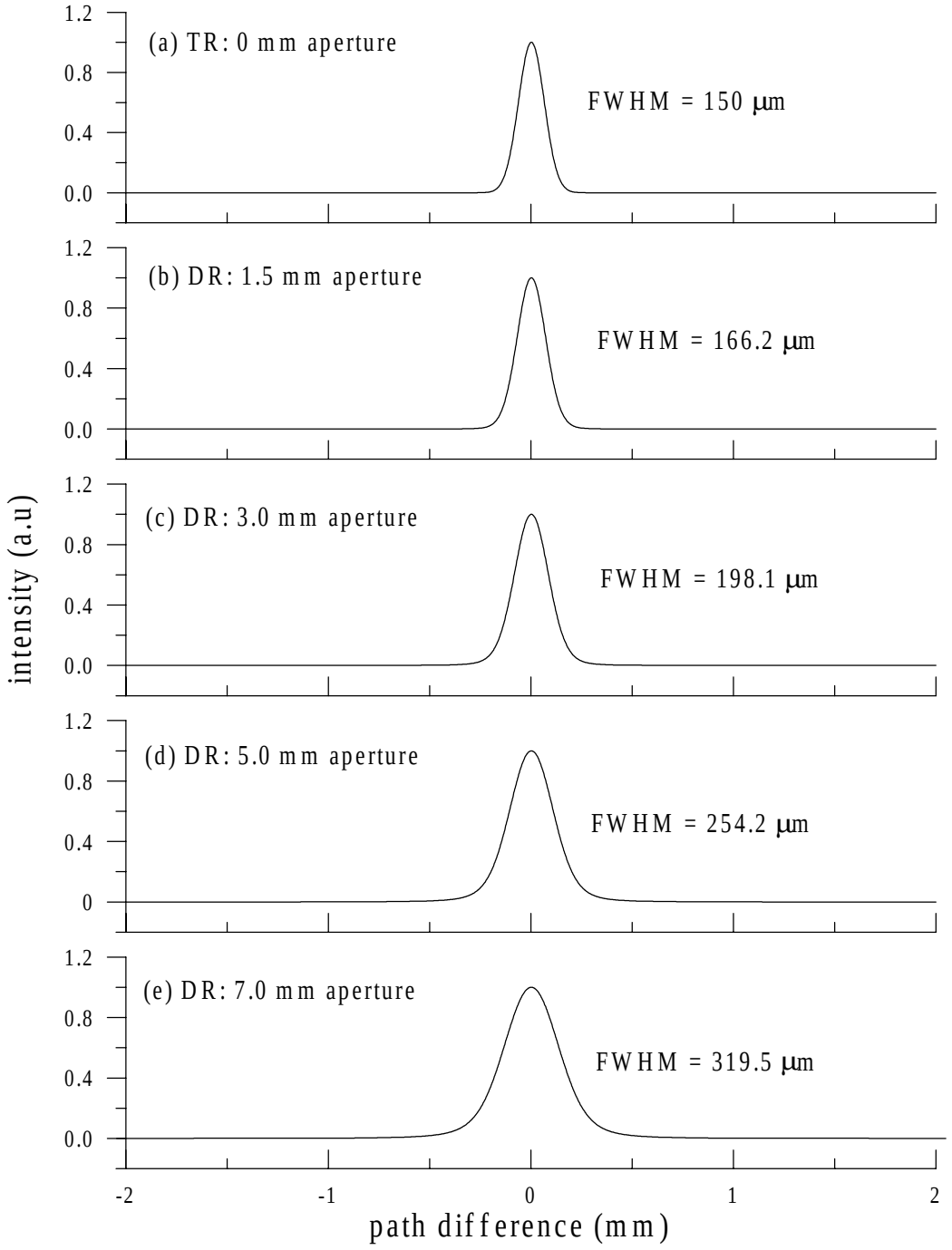

Figure 6.6: Simulated interferograms of a Gaussian bunch for (a) coherent transition radiation; and coherent diffraction radiation generated from (b) 1.5 mm, (c) 3.0 mm, (d) 5.0 mm, and (e) 7.0 mm diameter apertures.

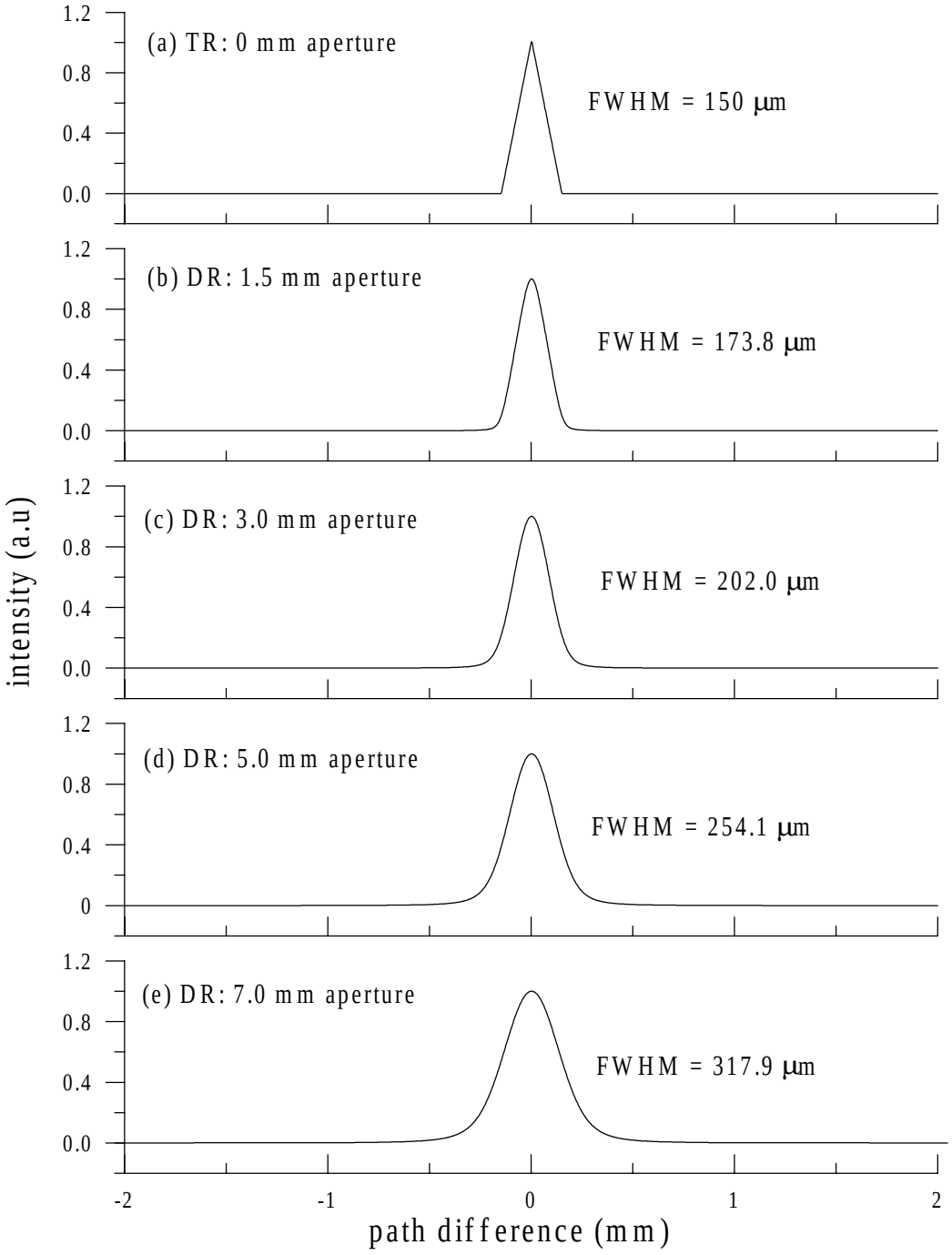

Figure 6.7: Simulated interferograms of a rectangular bunch for (a) coherent transition radiation; and coherent diffraction radiation generated from (b) 1.5 mm, (c) 3.0 mm, (d) 5.0 mm, and (e) 7.0 mm diameter apertures.

Radiation source	Measured FWHM (μm)
TR: 0 mm aperture	164
DR: 1.5 mm aperture	176
DR: 3.0 mm aperture	189
DR: 5.0 mm aperture	209

Table 6.2: Results of autocorrelation bunch length measurements with coherent transition radiation and with coherent diifraction radiation.

are using an observation angle of $1/\gamma$. An ideal interferogram would be the same as the case obtained by coherent transition radiation [Figure 6.6(a)]. As the aperture size becomes larger, the FWHM of simulated interferograms increases. An explanation for this is that high frequency components of the diffraction radiation spectrum are suppressed by interference as the aperture size increases (demonstrated in Figure 6.4). The suppression of high frequency components results in a seemingly broader pulse in time domain. The effect is similar in case of a uniform distribution. An ideal interferogram would be as the one in Figure 6.7(a) for a rectangular bunch while interferograms in Figure 6.7(b-e) are those include diffraction radiation spectral distribution. Again, the width of the interferogram increases as the aperture size increases.

6.3.1 Experimental Investigation

To investigate the lengthening of measured bunch lengths in the autocorrelation technique based on coherent diffraction radiation, we measure the bunch length using coherent diffraction radiation generated in the experimental setup shown in Figure 6.1. Interferograms have been taken with a Michelson interferometer in ambient air equipped with a 25.4-μm-Kapton beam splitter. Interferograms obtained from the radiation generated are displayed in Figure 6.8. The results are also summarized in Table 6.2 displaying the lengthening of measured bunch length as the aperture size increases. The bunch length measured by transition radiation is the most precise among all measurements since all the high frequency components of the coherent radiation spectrum are preserved (neglecting the transverse effect discussed in Chapter 5).

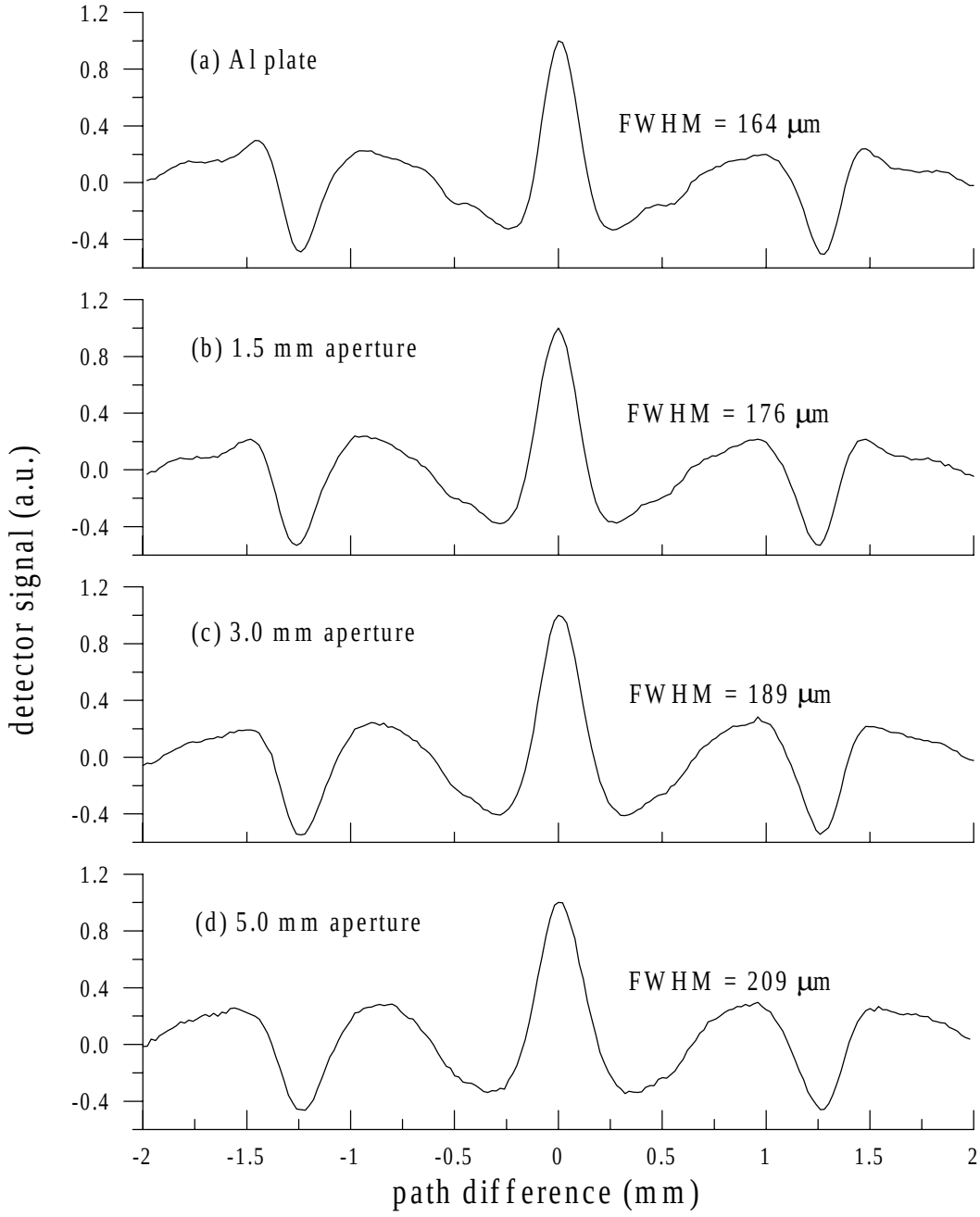

Figure 6.8: Measured interferograms from (a) coherent transition radiation generated from Al-plate; and from coherent diffraction radiation generated from (b) 1.5 mm, (c) 3.0 mm, and (d) 5.0 mm diameter apertures on the Al-plate.

The theoretical value of the FWHM for each measurement can be estimated, however it is not straightforward. Since the spectral distribution depends on the observation angle, interferograms taken at different observation angles feature different widths. In our experiments, we collect the radiation over the acceptance angle of $\theta_a = 120$ mrad. Therefore, the FWHM must be averaged over the acceptance angle after being folded by the angular spectral distribution of coherent diffraction radiation intensity.

$$\langle \mathrm{FWHM} \rangle = \frac{\int_0^{\theta_a} \mathrm{FWHM}\left(\theta\right) \int_0^{\infty} I_{cDR}\left(\omega, \theta\right) \left|R\left(\omega\right) T\left(\omega\right)\right|^2 \mathrm{d}\omega \mathrm{d}\theta}{\int_0^{\theta_a} \int_0^{\infty} I_{cDR}\left(\omega, \theta\right) \left|R\left(\omega\right) T\left(\omega\right)\right|^2 \mathrm{d}\omega \mathrm{d}\theta}, \tag{6.5}$$

where FWHM(θ) is the FWHM at an observation angle θ, $I_{cDR}\left(\omega\right)$ is angular spectral intensity of coherent diffraction radiation defined in (6.3) and $\left|R\left(\omega\right) T\left(\omega\right)\right|^2$ is the beam splitter efficiency. The FWHM as a function of observation angle for a Gaussian bunch can be obtained by simulations described earlier. The σ_z of the Gaussian bunch is chosen such that an ideal interferogram features a similar width as that of the measurement with coherent transition radiation. Theoretical estimates of FWHM are shown in Table 6.3 along with the measured values. Although the angular spectral distribution of diffraction radiation used in the model is valid for an infinitely thin beam passing through the center of a circular aperture, the theoretical and measured FWHMs show good agreement. The measured FWHM increases with a slower rate because some electrons in a finite beam width appear closer to the metallic boundary than the aperture radius and thus reducing the high frequency suppression.

It has been shown that the accuracy of autocorrelation bunch length measurement based on coherent diffraction radiation depends greatly on preservation of high frequency components in the radiation spectrum. Diffraction radiation spectral distribution, determined by aperture sizes and beam energy, must be taken into account for the bunch length measurement. Limitations regarding the accuracy of the measurement will be developed in the next section.

radiation source	Measured FWHM (μm)	Theoretical FWHM (μm)
TR: 0 mm aperture	164	164
DR: 1.5 mm aperture	176	179
DR: 3.0 mm aperture	189	194
DR: 5.0 mm aperture	209	219

Table 6.3: Measured FWHM and theoretical estimate of FWHM for autocorrelation bunch length measurements with coherent transition radiation and coherent diifraction radiation.

6.3.2 Limitations

Incoherent transition radiation has no frequency dependence in its spectral distribution over the far-infrared and infrared regime while the spectral distribution of the coherent transition radiation generated from short electron bunches is determined by the form factor. Therefore, the coherent transition radiation is perfect to use for autocorrelation bunch length measurement. Unlike transition radiation, diffraction radiation spectral distribution expressed by (6.1) and (6.2) features a frequency dependence. The spectral distribution depends on aperture sizes and beam energy; and that of a 26 MeV is shown is Figure 6.4. To determine whether the diffraction radiation can be used effectively for bunch length measurement, its spectral distribution should be considered together with the bunch form factor. The spectral distribution of diffraction radiation from a 26 MeV beam is shown again in Figure 6.9(a) along with that from a 100 MeV beam in Figure 6.9(b). In comparison, the form factor of a Gaussian bunch with $\sigma_z = 50$ μm is displayed in Figure 6.9(c). It is assumed here that only the longitudinal distribution contributes to the form factor. Coherent diffraction radiation intensity can be expressed by (6.1) and (6.3) as

$$\begin{aligned} I_{cDR}(\omega) &= N_b N_e^2 I_{TR} D(\omega) f(\omega) \\ &\propto D(\omega) f(\omega), \end{aligned} \tag{6.6}$$

where $f(\omega)$ is the form factor defined in (2.9), and $D(\omega)$ is defined in (6.1). Interferogram broadening discussed in the previous section can be avoided when the diffraction radiation spectrum, determined by the function $D(\omega)$, approaches unity

over the range of coherent radiation. In other words, $D(\omega) f(\omega)$ should be as close as possible to $f(\omega)$ to preserve the frequency information especially high frequency components in the coherent radiation spectrum. It can be seen from Figure 6.9 that the high frequency components of the coherent spectrum are suppressed for the case of coherent diffraction radiation generated by a 26 MeV beam from a 3-mm-aperture and a 5-mm-aperture. As a consequence, the bunch length measured with this setup can not be obtained directly without large corrections. On the other hand, the coherent diffraction radiation generated by a 100 MeV or higher energy beam suffers less from high frequency suppression of $D(\omega)$, especially with a 1-mm-diameter aperture (Figure 6.9(b)). The bunch length measurement for this case is, therefore, more reasonable.

In general, the beam energy and bunch length are given for a particular system but an aperture size is a more flexible parameter. To investigate a feasibility of using autocorrelation bunch length measurement based on coherent diffraction radiation in terms of beam parameters and aperture sizes, we analyze the form factor and function $D(\omega)$ qualitatively.

If observing the radiation at $1/\gamma$ and considering a relativistic beam with $\sin 1/\gamma \approx 1/\gamma$ and $\beta \to 1$, the function $D(\omega)$ in (6.2) can be simplified to

$$D(\omega) = \left[\mathrm{J}_0\left(\frac{\omega r}{c\gamma}\right)\left(\frac{\omega r}{c\gamma}\right)\mathrm{K}_1\left(\frac{\omega r}{c\gamma}\right)\right]^2. \tag{6.7}$$

For a precise bunch length measurement, $D(\omega)$ should be close to unity over the entire range of coherent radiation spectrum. Let us use the cut-off frequency of a Gaussian form factor $\omega_c = c/\sigma_z$, defined in (4.10), to represent the range of coherent radiation spectrum. Applying the condition that $D(\omega)$ at the cut-off frequency ω_c should be at least 90% of the maximum so that $D(\omega)$ causes only small perturbation to coherent radiation spectrum and to the bunch length measurement. The condition leads to

$$\left[\mathrm{J}_0\left(\frac{\omega_c r}{c\gamma}\right)\left(\frac{\omega_c r}{c\gamma}\right)\mathrm{K}_1\left(\frac{\omega_c r}{c\gamma}\right)\right]^2 \geqslant 0.9. \tag{6.8}$$

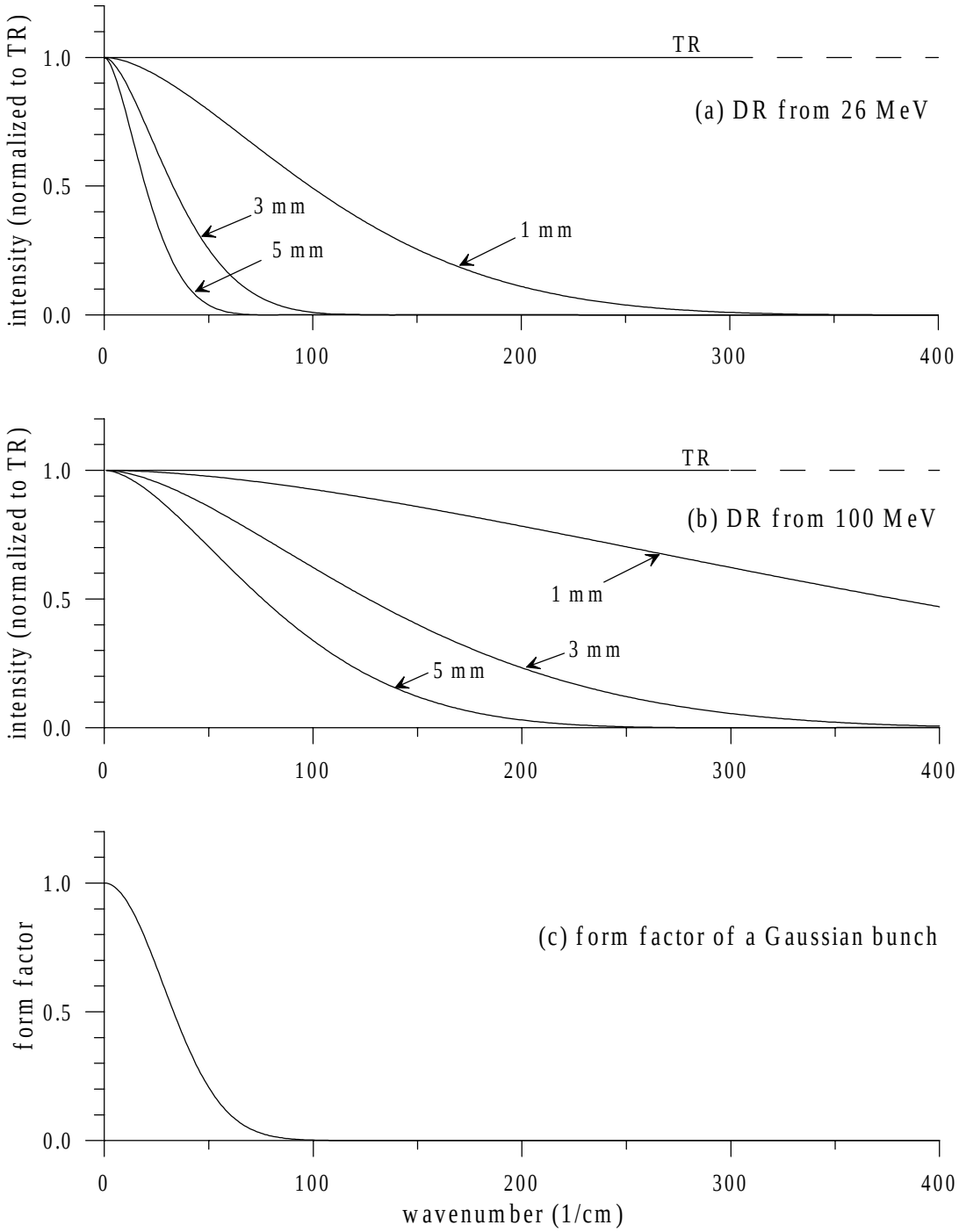

Figure 6.9: Spectral distribution of diffraction radiation generated by different aperture sizes for (a) 26 MeV beam and (b) 100 MeV beam. The form factor of a Gaussian bunch with $\sigma_z = 40\ \mu m$ is shown in (c).

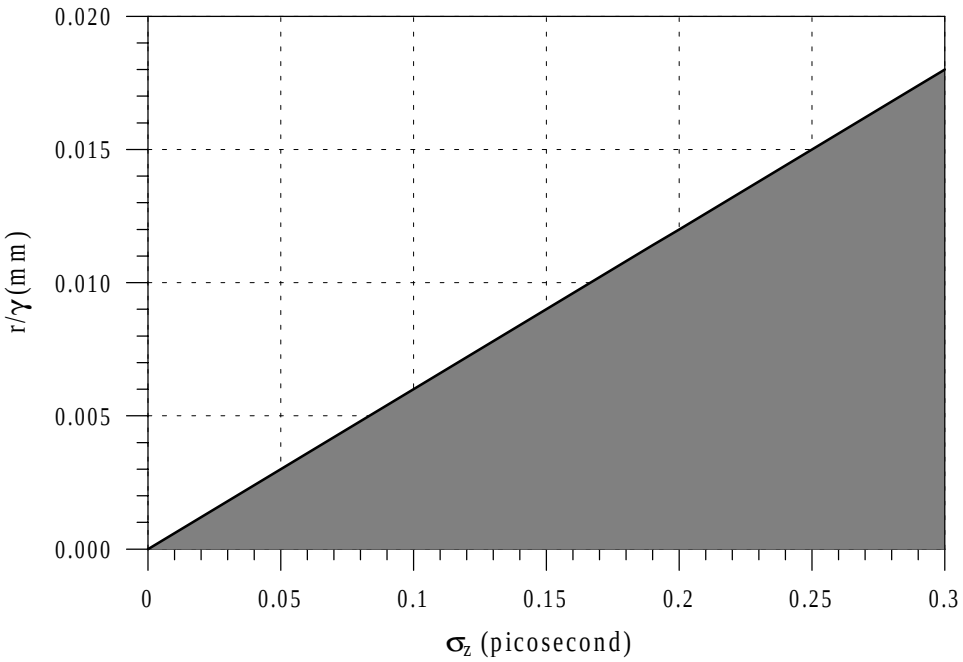

Figure 6.10: Bunch length, aperture radius and beam energy in autocorrelation bunch length measurement based on coherent diffraction radiation. On the curve, a measurement results in 5% longer than the measurement taken by coherent transition radiation.

The solution for (6.8) is

$$\frac{\omega_c r}{c\gamma} = \frac{r}{\sigma_z \gamma} \leqslant 0.2 \tag{6.9}$$

and Figure 6.10 expresses σ_z and r/γ under this condition. The shade area below the curve $r/\sigma_z\gamma = 0.2$ satisfies the condition in (6.9) . Simulations show that along this curve, the error in the bunch length measurement by autocorrelation of coherent diffraction radiation is +5% and less than that below the curve. Measurements aiming for higher accuracy should stay below the curve as much as possible. It is recommended that the bunch length is first measured using coherent transition radiation to calibrate the coherent diffraction radiation bunch length measurement system.

Chapter 7

Stimulated Transition Radiation

Coherent transition radiation from femtosecond electron bunches is a very promising high intensity source in the far-infrared spectral range. The radiation intensity is far greater than that of available conventional sources. In order to further increase the radiation intensity, a new method has been studied at SUNSHINE. This method combines the emission of coherent transition radiation from electron bunches with the stimulation of such radiation by an external field. With an optical cavity, we can use the radiation emitted by an earlier electron bunch as the source of the external field. The principle of stimulated transition radiation (STR) has been demonstrated in Refs. [3] and [40]. In this chapter, we describe further studies on this subject. The studies intend to investigate the generation of stimulation transition radiation in more detail with a goal of maximizing the radiation intensity from the stimulation.

7.1 Working Principle

One possible way to further increase the intensity of the coherent far-infrared transition radiation is to stimulate the emission process with an external electromagnetic field [12],[3]. To obtain stimulated transition radiation, we recycle the transition radiation generated from an electron bunch such that the radiation pulse arrives back at the radiator at the same time another electron bunch arrives there. The recycled radiation pulse serves now as an external stimulating field. In case of perfect temporal

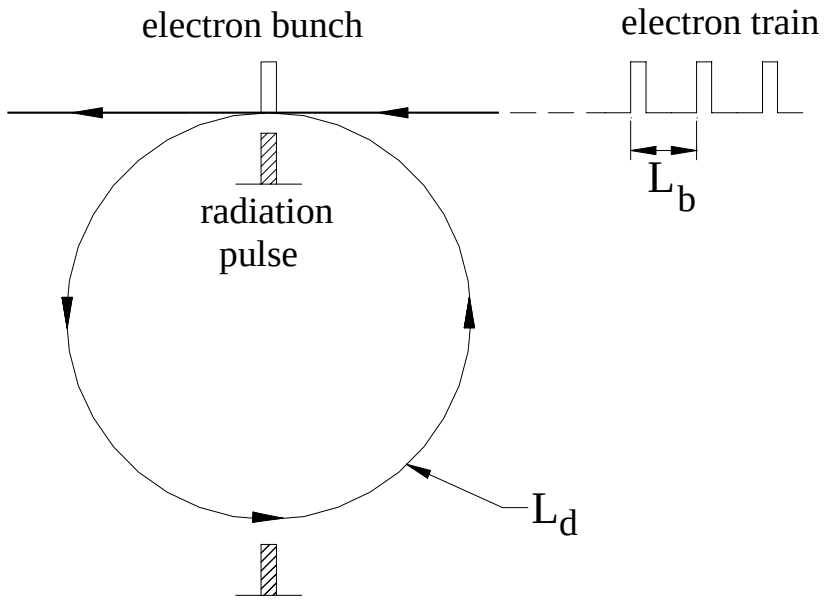

Figure 7.1: The stimulation using the radiation from a previous electron bunch as an external field.

coincidence between the external field and an in-coming electron bunch, this external field acts on the electrons to radiate extra energy. This extra energy is the stimulated radiation due to the work done by the external field on the electrons.

The schematic diagram in Figure 7.1 illustrates stimulation using the radiation from a previous electron bunch as an external field. We start with a train of electron bunches, in which the distance between two adjacent bunches is L_b. An electron bunch generates transition radiation, which is then recycled in a optical cavity with a total path length L_d. By adjusting the path length such that the recycled radiation pulse coincides with an in-coming electron bunch, stimulation can occur. The resonance condition for this stimulation can be expressed as

$$nT_r = mT_e \tag{7.1}$$

where T_r is the time that the radiation pulse takes to complete one passage through the optical cavity, T_e is the time interval between the two adjacent electron bunches

and parameters m and n are integers. This condition states that when a radiation pulse has travelled n times through the cavity, it will coincide with the m^{th} incoming electron bunch. Assuming that the electrons move with a velocity which is close to the speed of light, the expression can be written in term of distances instead of time as

$$nL_d = mL_{b,} \tag{7.2}$$

where L_d is the length of a round trip through the optical cavity and L_b is the distance between two adjacent electron bunches.

The frequency content of the stimulated transition radiation will be the harmonics of the revolution frequency. In other words, the cavity length must be an integer multiple of the radiation wavelength. The resulting spectrum of stimulated transition radiation therefore is a line spectrum with rather narrow spacing between lines.

7.2 Energy in the cavity

Stimulation can occur once the resonance condition is met. This section describes how the energy builds up in the cavity under such a condition. At the radiator, an electron bunch radiates a transition radiation field $\mathbf{E}_{TR}$. In the presence of electric field in the cavity $\mathbf{E}_{cav}$, the bunch radiates extra energy of $\mathbf{E}_{STR}$ which depends on the electric field in the cavity. This radiation field from stimulation can be expressed as $\mathbf{E}_{STR} = a\mathbf{E}_{cav}$, where a is the stimulation factor. The radiation field in the cavity after each bunch has passed is the total field that builds up in the cavity before a new bunch arrives. This total radiation field is, however, subjected to losses in the cavity as it circulates back to the radiator. We define the factor $d < 1$ to represent the remaining fraction of the radiation field after one circulation in the cavity.

We first consider a cavity with a length equal to the distance between two adjacent electron bunches ($L_d = L_b$). An electron bunch generates transition radiation energy which is proportional to $|\mathbf{E}_{TR}|^2$. The radiation is guided to circulate in the cavity and is subjected to some losses. The cavity field ($d\mathbf{E}_{TR}$) coincides with an in-coming

electron bunch, thus, stimulating the electrons in the bunch to radiate extra energy (adE_{TR}). At this point, the total radiation intensity

$$\varepsilon_{tot} = |\mathbf{E}_{tot}|^2 = |\mathbf{E}_{TR} + d(1+a)\mathbf{E}_{TR}|^2 \tag{7.3}$$

and continue circulating in the cavity. Defining b as

$$b = d\,(1+a)\,. \tag{7.4}$$

The radiation intensity after the i^{th} electron bunch has arrived can be expressed as

$$\begin{aligned} \varepsilon_{tot,i} &= |\mathbf{E}_{TR} + b\mathbf{E}_{TR} + b^2\mathbf{E}_{TR} + b^3\mathbf{E}_{TR} + ... + b^{i-1}\mathbf{E}_{TR}|^2 \\ &= |\mathbf{E}_{TR}|^2 \left(1 + b + b^2 + b^3 + ... + b^{i-1}\right)^2 \\ &= |\mathbf{E}_{TR}|^2 \left(\sum_{j=0}^{i-1} b^j\right)^2 . \end{aligned} \tag{7.5}$$

The expression can be simplified to

$$\varepsilon_{tot,i} = |\mathbf{E}_{TR}|^2 \left(\frac{1-b^i}{1-b}\right)^2 . \tag{7.6}$$

where $|\mathbf{E}_{TR}|^2$ is the transition radiation intensity from one electron bunch and b is defined in(7.4) which depends on stimulation and cavity losses.

For a cavity with $L_d = mL_b$, where m is an integer, the energy increases with the arrival of every m^{th} bunch and the cavity therefore contains m independent radiation pulses. The energy in the cavity after the i^{th} bunch has passed is

$$\begin{aligned} \varepsilon_{tot,i} &= m|\mathbf{E}_{TR}|^2 \left(\sum_{i=0}^{\lfloor i/m \rfloor - 1} b^i\right)^2 \\ &= m|\mathbf{E}_{TR}|^2 \left(\frac{1-b^{\lfloor i/m \rfloor}}{1-b}\right)^2 . \end{aligned} \tag{7.7}$$

Here, $\lfloor i/m \rfloor$ denotes the floor function which round off the value of i/m to the nearest

lower integer.

In most cases, a macropulse consists of a finite number of electron bunches depending on the macropulse length and the rf-wavelength. After the last electron bunch in the macropulse arrived, no more radiation can be generated and thus the radiation energy in the cavity starts to decay while continuing to circulate in the cavity. The energy in the cavity during the decay phase is thus the energy after the last $\left(N^{th}\right)$electron bunch that gets attenuated to the factor d during each pass. The expression can be written as

$$\begin{aligned} \varepsilon_{tot,i} &= \varepsilon_{tot,N}\left(d^{\lfloor i/m \rfloor - \lfloor N/m \rfloor}\right)^2 \\ &= m|\mathbf{E}_{TR}|^2\left(\frac{1-b^{\lfloor N/m \rfloor}}{1-b}d^{\lfloor i/m \rfloor - \lfloor N/m \rfloor}\right)^2, \quad i > N. \end{aligned} \tag{7.8}$$

The parameter i here is starting from $N+1$ since it is in the decay phase.

7.3 Stimulated Transition Radiation cavity

Stimulation of transition radiation emission can be achieved by using the radiation emitted from a previous electron bunch as an external field to stimulate the radiation emission of the next electron bunch. This section will describe the design of a cavity for generating stimulated transition radiation.

7.3.1 Conceptual design

A cavity as shown in Figure 7.2 can be used to generate stimulated transition radiation. It consists of a radiator (R), two off-axis parabolic reflectors (P1 and P2) and a plane reflector (M). The focal points of P1 and P2 are aligned on the radiator at point A and on the plane reflector at point B, respectively. P1 converts the divergent transition radiation emitted from point A to become parallel. P2 focuses the parallel light onto a point at B. The radiation is then reflected on M and transported back to P2, P1 and R at point A.

When the loop length starting from the radiator and back to the radiator (e.g.,

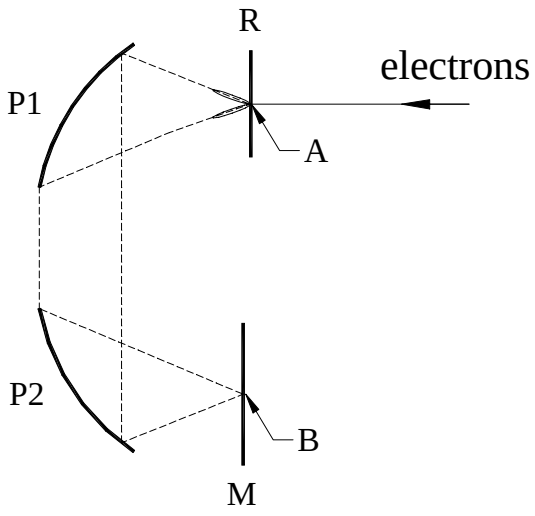

Figure 7.2: Conceptual design of a stimulated transition radiation cavity

A →P1 →P2 →B →P2 →P1 →A) is equal to the distance between two adjacent bunches in a train of equidistant electron bunches, stimulation will occur.

7.3.2 Polarization in the cavity

Not only does the radiation in the cavity have to arrive at radiator simultaneously with another in-coming electron bunch, but also its polarization must have proper direction to fulfil the stimulation conditions. The external radiation which can be used for stimulation should have the same polarization as that of the radiation emitted from the incoming electron bunch. While the timing condition can be accomplished by adjusting the cavity loop length, the polarization condition requires a specific arrangement of the cavity components. As the radiation pulse travels through the cavity whose design is discussed in the previous section, it polarization condition is traced and shown in Figure 7.3. The polarization of the radiation in the upper half of the radiation cone is shown in Figure 7.3(a) while that of the lower half is shown in Figure 7.3(b). The radiation polarization after one round trip travelling through the cavity has the same direction as that of the radiation emitted from an incoming electron bunch. That would not be the case if we would use a much simpler cavity

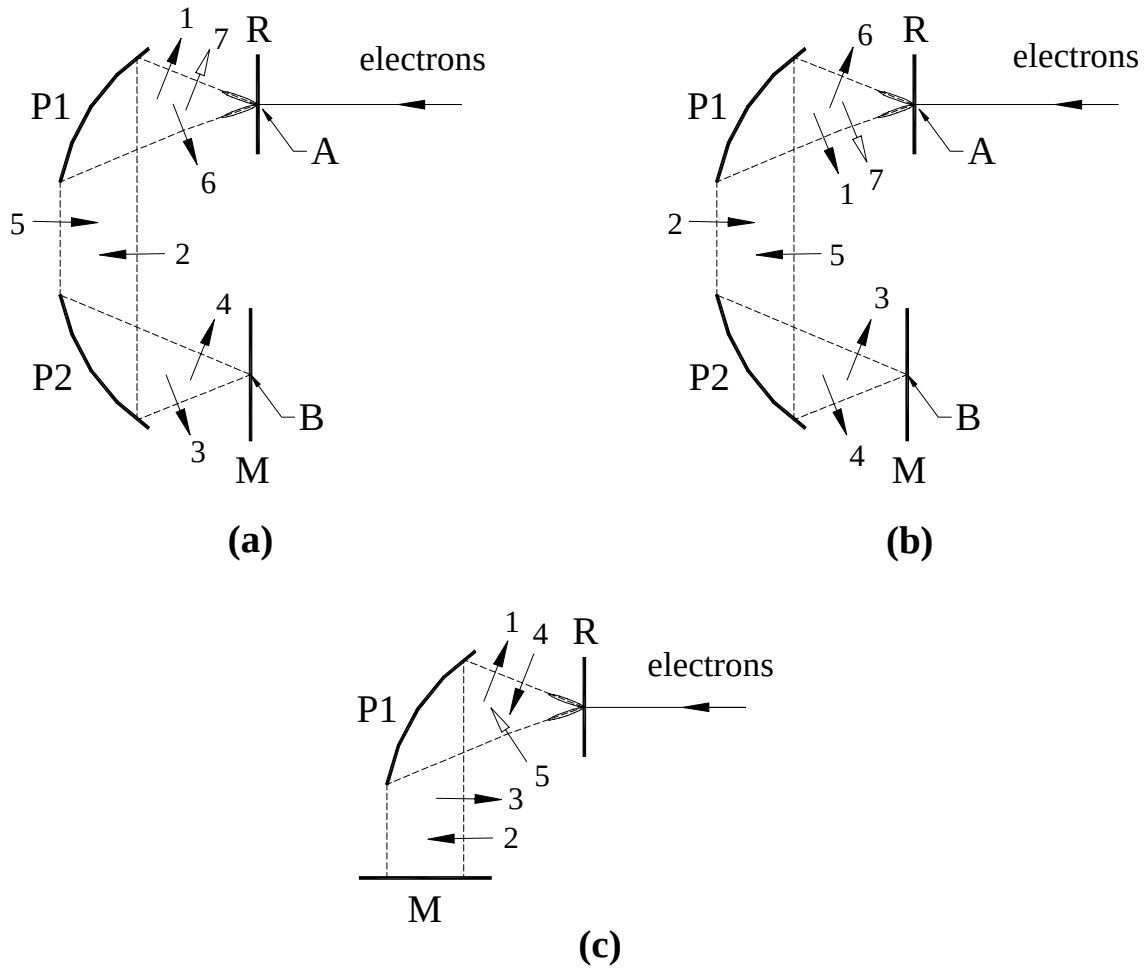

Figure 7.3: Radiation polarization in the cavity as the radiation travels through all components: (a) the upper half of the radiation cone and (b) the lower half of the radiation cone. The numbers indicate chronological events. For example, the polarization marked number 1 is the polarization of the transition radiation just emitted from electrons and the polarization marked number 7 (shown by an unfilled head arrow) is the radiation after one circulation in the cavity. The diagram in (c) shows a setup that does not meet the required polarization condition.

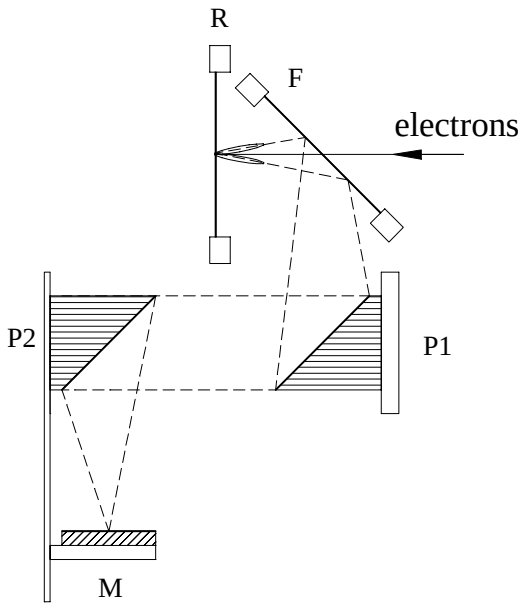

Figure 7.4: A schematic layout of the stimulated transition radiation cavity.

with a flat reflector between P1 and P2 [Figure 7.3(c)].

7.4 The cavity setup

Following the conceptual design of the cavity in Figure 7.2, a realistic layout is shown schematically in Figure 7.4 and is used for the stimulated transition radiation studies reported here. It consists of a radiator (R), a foil reflector (F), two off-axis parabolic mirrors (P1 and P2) and a flat mirror (M). The radiator and the foil reflector (R and F) are made of 20-μm-thick aluminum foils supported by an aluminum ring using the drumhead stretching principle. All mirrors are gold-coated first surface mirror. The foil reflector (F) is tilted 45° with respect to the beam axis to separate the transition radiation generated at R from the electron beam. After being deflected at F, the radiation is transported to P1 and the rest of the cavity. The effective focal length of P1 and P2 are 150 mm and 100 mm, respectively. The focal point of P1 is aligned on the center of R, while the focal point of P2 is aligned on the center of M. The parabolic mirror P2 and the flat mirror F are mounted on a remote-controlled linear

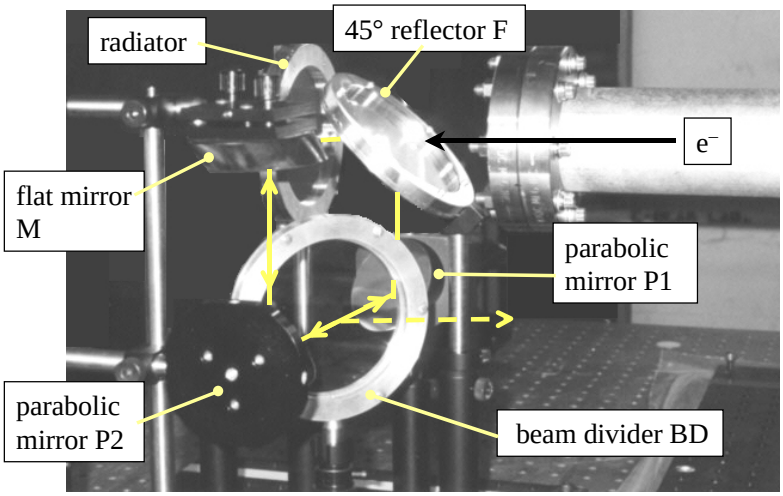

Figure 7.5: Setup of the stimulated transition raditaion cavity at the end of the beam line.

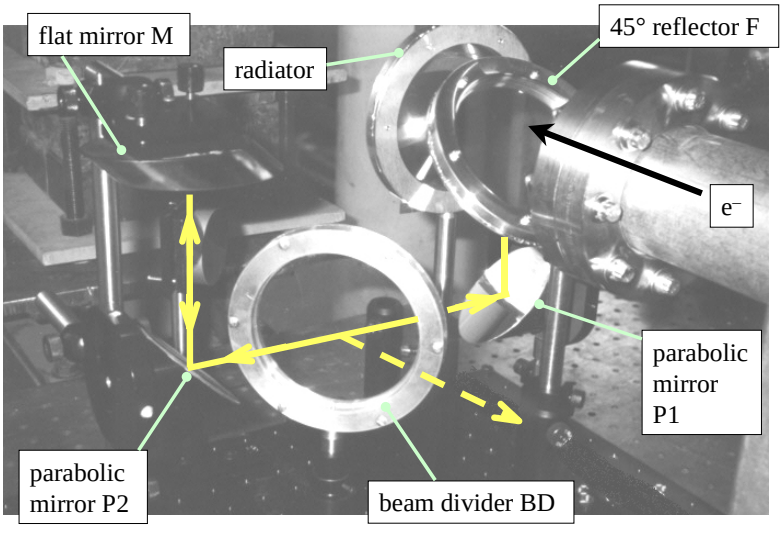

Figure 7.6: Another view of the stimulated transition radiation cavity.

translation stage. This allows us to change the cavity path length without affecting the alignment of the cavity.

Figure 7.5 and 7.6 show pictures of the actual experimental setup of a stimulated transition radiation cavity. A beam divider (BD) is used to couple out the some of radiation energy from the cavity. Part of the radiation is deflected by this beam divider and is extracted out of the cavity for monitoring, while the rest of the radiation is transmitted through the beam divider and remains in the cavity. The radiation extraction contributes a cavity loss, which must be chosen carefully to optimize the stimulation.

As a train of N electron bunches enters the cavity, the radiation energy builds up while the beam divider is extracting part of the radiation out of the cavity. The extracted energy after the i^{th} electron bunch is proportional to the energy in the cavity at that moment. This extracted energy is determined by the a reflection coefficient R or a reflectance $|R|^2$ of the beam divider and is written as

$$\varepsilon_{out,i} = d_o^2 |R|^2 \varepsilon_{tot,i} \tag{7.9}$$

where $\varepsilon_{tot,i}$ is defined in (7.7) for $i \leq N$ and in (7.8) for $i > N$; and d_o is the remaining fraction of the radiation field as radiation travels from the radiator to the beam divider. The total extracted radiation energy from this stimulated transition radiation is the combination of these extracted energies while the radiation energy builds up and decays.

7.5 Cavity scan

With a beam divider in the cavity, the radiation energy is coupled out at all times and the extracted energy is proportional to the energy in the cavity. If we look at this extracted energy, we can monitor the radiation energy in the cavity.

By monitoring the cavity energy as a function of the cavity loop length, called a cavity scan, we can observe the stimulation. In a cavity scan, we expect a stimulation

when the cavity loop length fulfills the resonance condition $L_d = \frac{m}{n}L_b$. The on-resonance output energy is shown in (7.9) and the off-resonance output energy when no stimulation occurs is

$$\varepsilon_{off} = N d_o^2 |R|^2 |\mathbf{E}_{TR}|^2 \sum_i^{\infty} d^{2(i-1)} \tag{7.10}$$

Stimulation enhancement G_s can be obtained from the stimulated transition radiation intensity normalized to the off-resonance intensity. For an integer resonance, G_s can be expressed as

$$G_s = \frac{m}{N\sum_i^{\infty} d^{2(i-1)}} \left[\begin{array}{c} \sum_{i=1}^{\lfloor N/m \rfloor} \left(\frac{1-b^{\lfloor i/m \rfloor + 1}}{1-b} \right)^2 + \\ \sum_{i=\lfloor N/m \rfloor + 1}^{\infty} \left(\frac{1-b^{\lfloor N/m \rfloor}}{1-b} d^{\lfloor i/m \rfloor - \lfloor N/m \rfloor} \right)^2 \end{array} \right] \tag{7.11}$$

Similarly, for the n^{th} order resonance,

$$G_s = \frac{nm}{N\sum_i^{\infty} d^{2(i-1)}} \left[\begin{array}{c} \sum_{i=1}^{\lfloor N/nm \rfloor} \left(\frac{1-b^{\lfloor i/m \rfloor + n}}{1-b^n} \right)^2 + \\ \sum_{i=\lfloor N/nm \rfloor + 1}^{\infty} \left(\frac{1-b^{\lfloor N/m \rfloor}}{1-b^n} d^{\lfloor i/m \rfloor - \lfloor N/m \rfloor} \right)^2 \end{array} \right] \tag{7.12}$$

7.6 Experimental Results and Analysis

The cavity whose the structures have been described in Section 7.4, is used to observe stimulated transition radiation at the SUNSHINE facility. The whole cavity is placed at the end of the beam line after a 75-μm-thick stainless steel window, which separates the evacuated beam line and the ambient air. Electrons pass through the stainless steel window and enter the cavity. At the radiator, the electrons generate transition radiation, which is then recycled in the cavity to start the stimulation. Part of the radiation is extracted from the cavity through a 127-μm-thick polyimide (Kapton) beam divider. This radiation is detected by a room-temperature pyroelectric detector. The detector signal indicates the output radiation energy, which is proportional to the energy stored in the cavity, and by monitoring this output signal we can observe

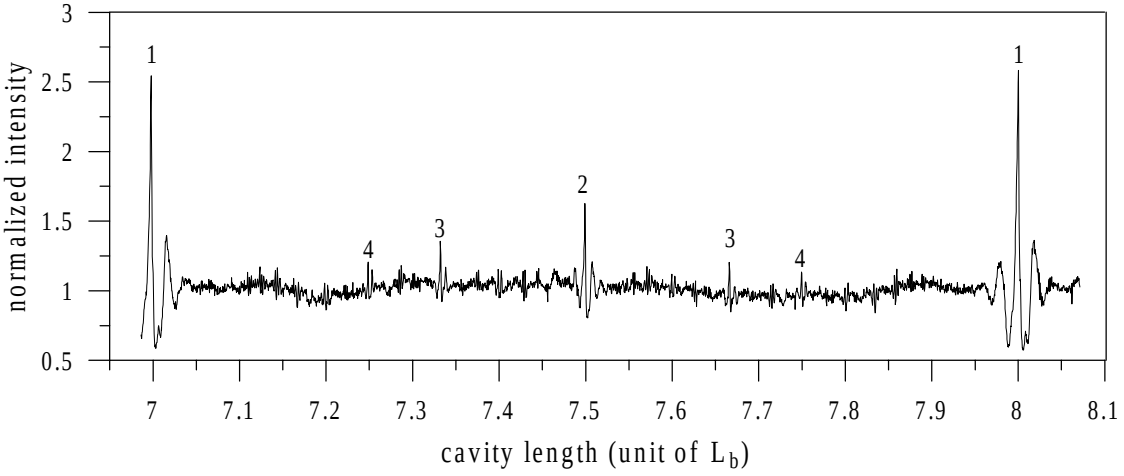

Figure 7.7: The cavity scan within $7L_b$ and $8L_b$.

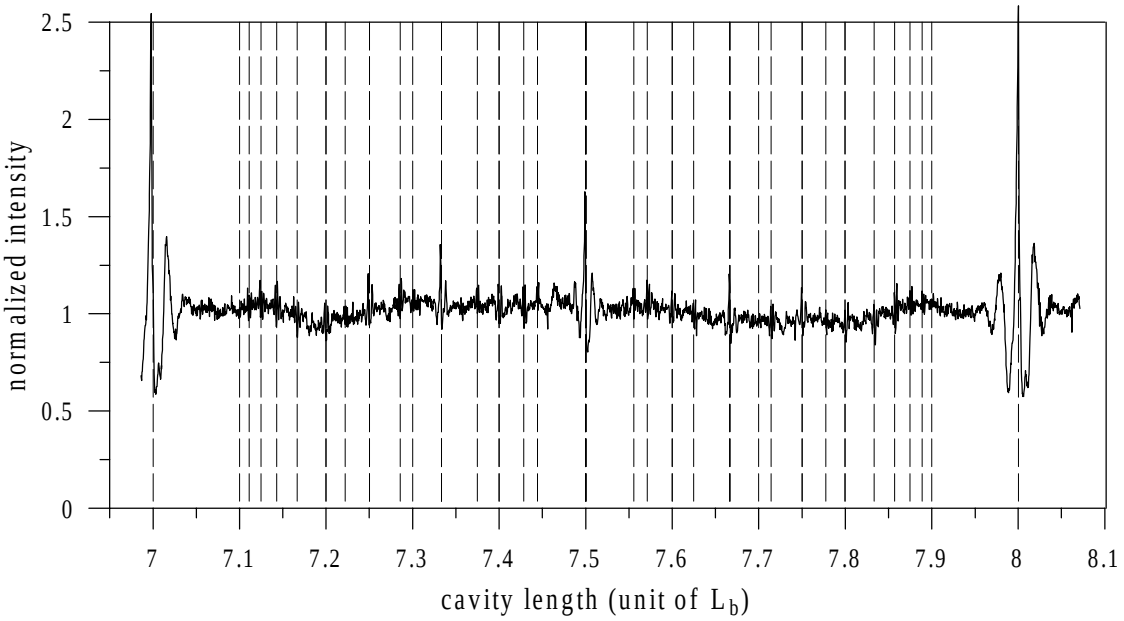

Figure 7.8: The cavity scan within $7L_b$ and $8L_b$ together with the locations (indicated by dashed-lines) where resonances up to the 10^{th} order are expected.

the stimulation.

The path length through the cavity is about $7L_b$ to $8L_b$. By varying the cavity length between $7L_b$ and $8L_b$, stimulation at different resonances can be observed. The cavity scan is shown in Figure 7.7. The numbers in the figure indicate the order of resonance; for example, the peak labelled "1" is the first order resonance (integer resonance or $n = 1$) and the peak marked by "2" is the second order resonance (half integer resonance or $n = 2$). In Figure 7.8, we show the same scan together with the locations where we expect stimulation up to the 10^{th} order resonance to occur. The scan confirms the occurrence of stimulated transition radiation. The stimulation enhancement at an integer resonance for this setup is $G_s = 2.5$. This enhancement factor is directly related to how the energy builds up in the cavity. In other words, this stimulation enhancement is a function of the parameter $b = d\,(1 + a)$, defined in (7.4). While the stimulation factor a is undetermined at this point, the remaining factor d depends greatly on the cavity losses.

To demonstrate the impact of losses in the cavity, the stimulation enhancement was measured for different thicknesses of Kapton beam dividers. The extracted energy depends on the reflection coefficient R or the reflectance $|R|^2$ of the beam divider which varies with frequency due to thin film interference effects. Therefore, the thickness of the beam divider determines its reflectance and thus the extraction of energy in the stimulated transition radiation cavity. The coherent transition radiation spectrum at the stimulated transition radiation experimental station is contained within 20 cm^{-1} because of the high frequency suppression from the transverse effect of a large beam size, after the beam scatters through the stainless steel window. In this frequency range, the average reflectance of a Kapton film beam divider decreases with the thickness. Therefore, decreasing the thickness of the beam divider results in a reduction of extracted energy thus reducing cavity losses. Table 7.1 shows the stimulation enhancement for 127 μm, 76.2 μm, 50.8 μm, and 25.4 μm beam divider. As expected, when using thinner beam dividers to extract less radiation out of the cavity, the cavity losses are reduced, and thus the stimulation increases.

So far the maximum stimulation enhancement at an integer resonance is achieved by using a 25 μm Kapton beam divider. Figure 7.9 shows a cavity scan near an integer

beam divider thickness (μm)	**stimulation enhancement G_s**
127	2.6 ± 0.1
76.2	3.6 ± 0.1
50.8	4.7 ± 0.2
25.4	8.2 ± 0.6

Table 7.1: Stimulation enhancement with different beam divider thicknesses.

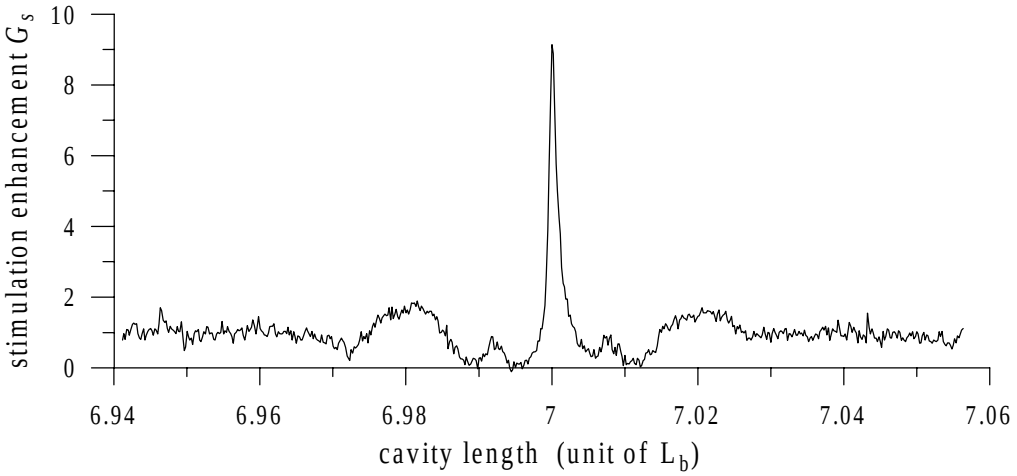

Figure 7.9: Maximum stimulation enhancement G_s when a 25-μm-thick beam divider is used in the cavity.

resonance from this setup demonstrating the stimulation enhancement around nine.

7.7 Conclusion

Stimulated coherent transition radiation by the transition radiation emitted by previous electron bunches is observed. The radiation pulse emitted from these previous bunches are cycled in an optical cavity. By adjusting the cavity length such that the radiation pulse coincides at the radiator with an incoming electron bunch, it can stimulate more radiation emission from the electrons. The optical cavity, consisting of metallic mirrors and reflectors, is arranged such that the circulated radiation

pulses arrive with the proper polarization for the stimulation. Measuring the radiation intensity extracted from the cavity while adjusting the cavity length, we observed stimulated transition radiation up to the 9^{th} order resonance. With a 25-μm-thick Kapton beam divider, we can obtain a factor of nine increase of the on-resonance radiation intensity over the off-resonance intensity. The cavity, however, still has high losses, including those from absorption in humid air, from non-perfect reflection , from mirror diffraction, and from radiation extraction. To improve the cavity performance for high radiation intensity, a better designed and engineered cavity must be considered. Such a design will have to include optical as well as microwave design features to properly treat electromagnetic radiation in this transition between both regimes.

Chapter 8

Far-infrared Spectroscopy

The coherent transition radiation generated from femtosecond electron bunches covers much of the far-infrared spectral range and the radiation intensity is far greater than that of conventional sources available. Therefore far-infrared spectroscopy can be done easily using such a high intensity source and a Michelson interferometer. In addition, the high intensity of the radiation source makes it possible for the system to use a room temperature detector which is simple and convenient.

The far-infrared spectroscopy can be done using a technique called Fourier Transform Spectroscopy (FTS) which measures power transmission or power absorption of a sample. Figure 8.1 shows a schematic diagram of a FTS setup, in which a sample is placed between the radiation source and a Michelson interferometer. The water absorption spectrum shown earlier is an example of this kind of spectroscopy. Although phase information has been lost in the measurement, optical constants of the sample can be obtained by some modelling or Kramers-Kronig calculation [20].

Dispersive Fourier Transform Spectroscopy (DFTS) is a technique that allows direct determination of optical constants of a sample. The technique has also been known as asymmetric Fourier transform spectroscopy. In a DFTS setup, a sample is inserted in one arm of the interferometer, causing attenuation and dispersion of the radiation pulse. The attenuated and dispersed pulse can be recorded and its attenuation factor and phase shift can then be recovered. The attenuation and dispersion

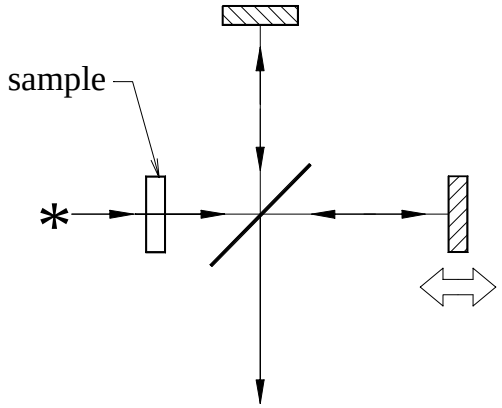

Figure 8.1: Schematic diagram of Fourier Transform Spectroscopy (FTS).

can be related to optical constants of the sample depending on the optical configuration of the measurements. With the DFTS technique, the phase information can be recovered in measurements using a Michelson interferometer.

In this chapter, the general theory of DFTS will be described, followed by the refractive index measurement of silicon obtained from two different measurement configurations. This technique and the recognition of the multiple reflections in the pyroelectric detector crystal (described in Chapter 5) also allow us to calculate the refractive index of the detector crystal. These refractive index measurements demonstrate far-infrared spectroscopy using coherent transition radiation. More detail of DFTS can be found in Ref. [41] and the references there in.

8.1 General Theory of DFTS

In order to measure optical properties of a sample, the sample must be introduced in the beam path. This can be done in many different ways. Although there are some details that are different in these setups depending on their configurations, DFTS can be described for a generalized sample as the following (modified from [41]).

An interferogram of the original radiation obtained in a sample-free interferometer is called the radiation interferogram $I_0(\delta)$ and it relates to the radiation power

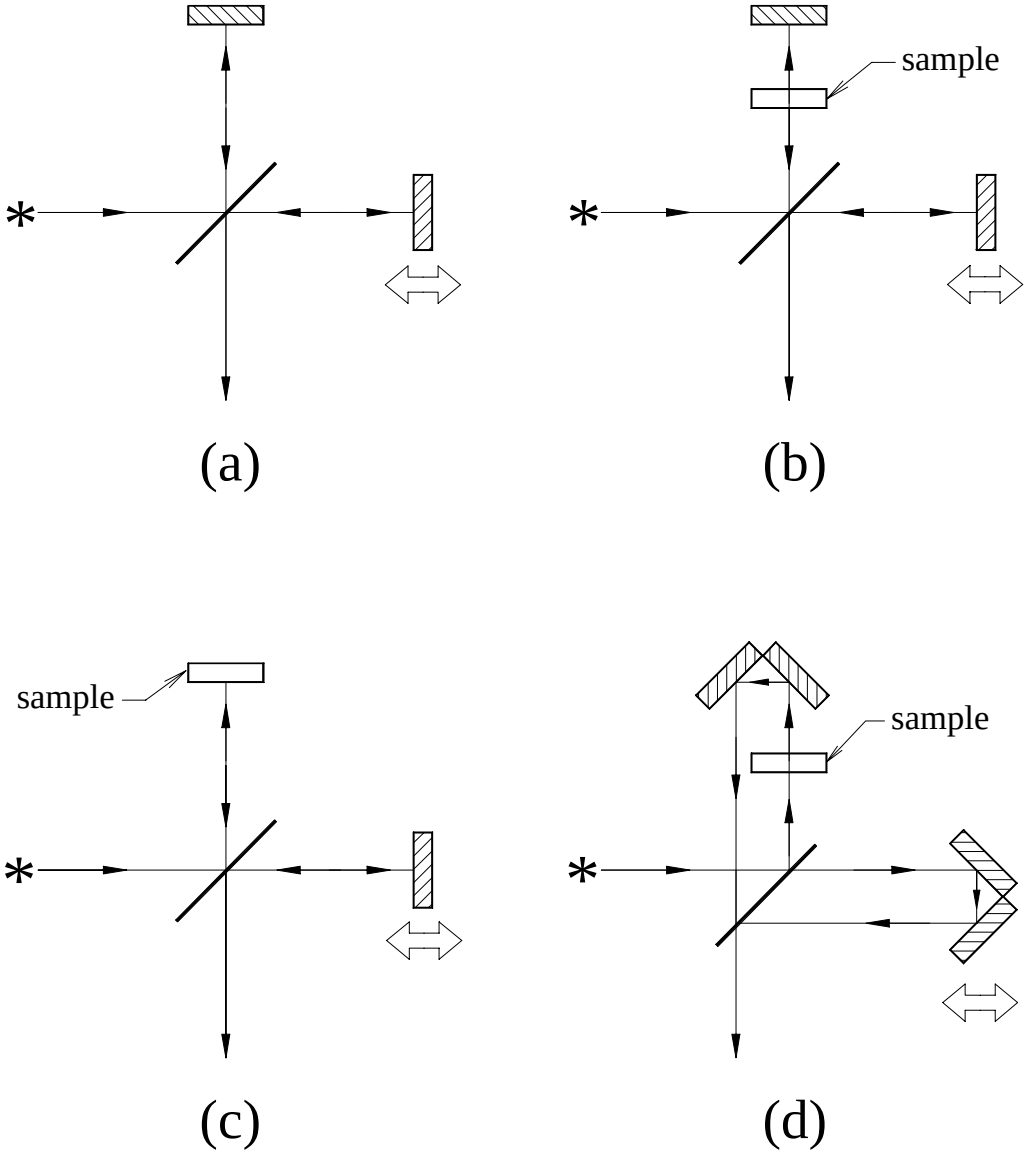

Figure 8.2: General setup for DFTS: (a) sample-free interferometer, (b) double-pass transmission measurement , (c) reflection measurement, (d) single-pass transmission measurement.

spectrum by Fourier transformation.

$$\left|\tilde{E}_0(\omega)\right|^2 = \tilde{E}_0(\omega)\tilde{E}_0^*(\omega) \propto \int_{-\infty}^{+\infty} I_0(\delta)e^{i\omega\delta/c}\mathrm{d}\delta, \tag{8.1}$$

where δ is the optical path difference, neglecting here the frequency response of the beam splitter. Equation (8.1) can be written as

$$\mathrm{FT}\{I_0(\delta)\} \propto \tilde{E}_0(\omega)\tilde{E}_0^*(\omega), \tag{8.2}$$

where $\mathrm{FT}\{f\}$ represents the Fourier transform of a function f .

When a sample is inserted in the fixed arm of the interferometer, the radiation propagating through the sample will be modified by the sample frequency-response, defined by

$$\tilde{S}(\omega) = |S(\omega)|\, e^{i\phi_s}. \tag{8.3}$$

This sample frequency-response is a complex factor that indicates changes of the wave amplitude and phase depending on experimental configurations. The modified electromagnetic wave can be written as

$$\tilde{E}_1(\omega) = \tilde{S}(\omega)\tilde{E}_0(\omega) \tag{8.4}$$

and the interferogram obtained from this arrangement is $I_1\,(\delta)$ where

$$\mathrm{FT}\{I_1(\delta)\} \propto \tilde{E}_1(\omega)\tilde{E}_0^*(\omega) = \tilde{S}(\omega)\tilde{E}_0(\omega)\tilde{E}_0^*(\omega). \tag{8.5}$$

From (8.2), (8.4), and (8.5), one can determine the sample frequency-response from the measurement by taking the ratio of the two Fourier transforms

$$\tilde{S}(\omega) = \frac{\mathrm{FT}\{I_1(\delta)\}}{\mathrm{FT}\{I_0(\delta)\}} = \frac{\tilde{E}_1(\omega)\tilde{E}_0^*(\omega)}{\tilde{E}_0(\omega)\tilde{E}_0^*(\omega)} = \frac{\tilde{E}_1(\omega)}{\tilde{E}_0(\omega)}. \tag{8.6}$$

By relating the sample frequency-response $\tilde{S}(\omega)$ obtained from the measurement to

that expressed in terms of optical constants, we can calculate the optical constants of the sample. The relationship of $\tilde{S}(\omega)$ and optical constants of the sample depends on the experimental configurations. The simplest experimental configuration is to place the sample into the fixed arm of the interferometer as shown in Figure 8.2(b). The radiation in the fixed arm propagates through the sample twice and the configuration is known as a double-pass transmission measurement. For an opaque sample, however, the transmitted radiation may be too small. The reflection measurement is then required for such a sample. The sample replaces the fixed mirror in the interferogram as shown in Figure 8.2(c). The phase shift in the transmission measurement is generally much greater than that obtained in the reflection measurement. Transmission measurements, if possible, are therefore preferred as they offer higher accuracy. For a sample whose transparency may be insufficient for the double-pass measurement, a single-pass transmission measurement may be conducted. A schematic diagram of a single-pass transmission measurement, in which the radiation propagates only once through the sample, is shown in Figure 8.2(d). The setup is more sophisticated than that of a double-pass transmission measurement. In addition to these basic measurements, optical constants of a sample can be obtained by considering reflections from two interfaces of the sample. The measurement can be set up in a similar way as the double-pass transmission measurement. Since reflection from the sample interfaces are compared, the radiation interferogram is no longer required. The following sections will describe the refractive index calculation from basic DFTS measurements including reflection measurement, single-pass transmission measurement, double-pass transmission measurement, and two-interface reflection measurement.

8.1.1 Reflection on the First Surface

For a sample with large absorption coefficients, transmission measurements can not be conducted pragmatically. The refractive index of such a sample may be determined by measuring reflection from the first surface of the sample. The principle of the method is to compare the radiation reflected from the sample to the original radiation field. The reflected radiation pulse is modified by the reflectivity of the sample

and this information can be extracted from the measurement. After recording the radiation interferogram $I_0(\delta)$, the fixed mirror is replaced by a sample and the sample interferogram $I_1(\delta)$, is then recorded. The replacement should be done such that the fixed mirror and the front surface of the sample occupy the same plane.

For a highly absorbing sample, only the first term of the amplitude reflection coefficient (described in Appendix B) will contribute to the recorded signal of $I_1(\delta)$. The amplitude reflectivity of the sample

$$\tilde{r} = |r|\, e^{i\phi_r}, \tag{8.7}$$

while that of a metallic mirror is

$$\tilde{r}_m = e^{i\pi}. \tag{8.8}$$

The sample frequency response can then be expressed in terms of the reflection coefficient by

$$\tilde{S}(\omega) = \frac{\mathrm{FT}\{I_1(\delta)\}}{\mathrm{FT}\{I_0(\delta)\}} = \frac{\tilde{E}_1(\omega)}{\tilde{E}_0(\omega)} = \frac{|r|\, e^{i\phi_r}}{e^{i\pi}} = -\tilde{r} \tag{8.9}$$

and can be related to the refractive index of the sample $\tilde{n}$ using (B.7) in Appendix B by

$$\tilde{n} = \frac{(1-\tilde{r})}{(1+\tilde{r})}, \tag{8.10}$$

assuming the interferometer is in an vacuum environment with $n_1 = 1$.

8.1.2 Single-pass Transmission

A schematic diagram of a single-pass transmission measurement is shown in Figure 8.2(d). The measurement requires both radiation interferogram and sample interferogram, taken with the sample placed in the fixed arm of the interferometer. Figure 8.3 shows a schematic of a radiation interferogram and a sample interferogram recorded

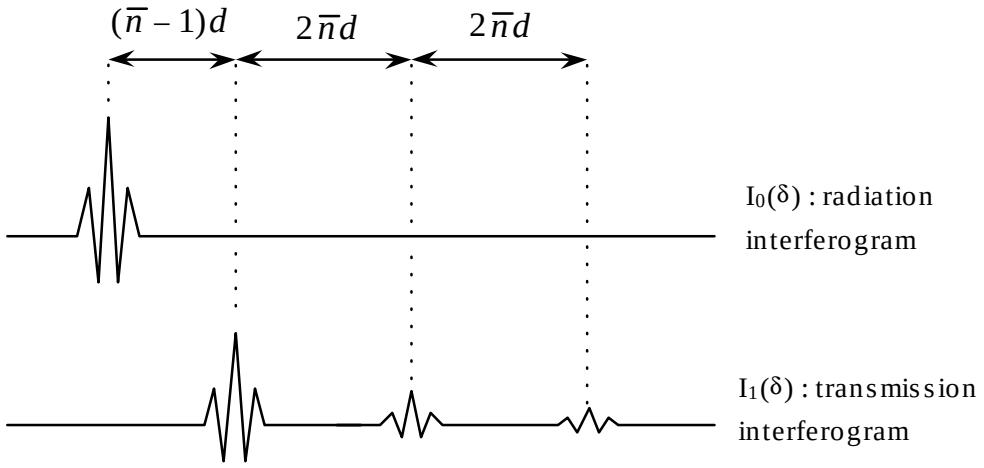

Figure 8.3: Radiation interferogram and transmission interferogram.

in a single-pass transmission measurement. If the sample is sufficiently thick and the radiation pulse duration is shorter than the travel time through the sample, the signatures associated with multiple reflections and transmissions are well separated. These signatures are displaced from the center of the radiation interferogram by $(\bar{n}-1)d$, $(3\bar{n}-1)d$, etc. Here, d is the sample thickness and $\bar{n}$ is the average value of the refractive index over the spectral range of interest. The single transmission signature is displaced from the center of the radiation interferogram by $(\bar{n}-1)d$ as shown in Figure 8.3. Using the first term of the transmission coefficient in $(B.14)$ we can expressed the single transmitted radiation field as $\tilde{E}_1(\omega) = \tilde{t}_{12}\tilde{a}_2\tilde{t}_{21}\tilde{E}_0(\omega)$.

The sample frequency-response from the measurement $\tilde{S}(\omega)$ for this case

$$\begin{aligned}\tilde{S}(\omega) &= \mathrm{FT}\{I_1(\delta)\}/\mathrm{FT}\{I_0(\delta)\} \\ &= e^{i2\pi\nu b}\mathrm{FT}\{I_1(\delta-b)\}/\mathrm{FT}\{I_0(\delta)\} = |S|\,e^{i\phi_s}, \end{aligned} \tag{8.11}$$

where $b = (\bar{n}-1)d$ is the separation between center of the two interferogram. This sample frequency-response can be related to optical constants of the sample through

the transmission coefficient by

$$\tilde{S}(\omega) = \frac{\mathrm{FT}\{I_1(\delta)\}}{\mathrm{FT}\{I_0(\delta)\}} = \frac{\tilde{E}_1(\omega)}{\tilde{E}_0(\omega)} = t_{12}a_2t_{21}e^{-i\omega d/c}, \tag{8.12}$$

where d is the sample thickness. Using the transmission and reflection coefficients in (B.8) and (B.10), the sample frequency-response, in terms of optical constants of the sample, is

$$\begin{aligned} \tilde{S}(\omega) &= \frac{\tilde{E}_1(\omega)}{\tilde{E}_0(\omega)} = \frac{4\tilde{n}}{(1+\tilde{n})^2}e^{i\omega\tilde{n}d/c}e^{-i\omega d/c} \\ &= \frac{4\tilde{n}}{(1+\tilde{n})^2}e^{-\omega n_i d/c}e^{i\omega(n_r-1)d/c} = |S|\, e^{i\phi_s}. \end{aligned} \tag{8.13}$$

This relationship and the sample frequency-response from the measurement in (8.11) allow us to calculate the complex refractive index of the sample. For $n_r \gg n_i$, which is true for a transparent sample, the phase ϕ_s can be equated to the phase $(n_r - 1)\,\omega d/c$ as well as the amplitudes $|S| = 4n_r/\left(1+n_r\right)^2$. The real and imaginary parts of the refractive index as a function of $\nu = \omega/2\pi c$, therefore, can be calculated by

$$n_r(\nu) = 1 + \frac{1}{2\pi\nu d}\left[\phi_s(\nu)\right]. \tag{8.14}$$

$$n_i(\nu) = \frac{1}{2\pi\nu d}\ln\left[\frac{16n_r(\nu)}{|S(\nu)|\left[1+n_r(\nu)\right]^2}\right]. \tag{8.15}$$

Noting that the phase ϕ_s obtained from the measurement or (8.11) is, however, only the principal value of the phase different between the two Fourier transforms. It may be necessary to replace ϕ_s in (8.11) by $\phi_s + 2m\pi$, where $m = 0, 1, 2,...$, especially for a highly dispersive sample, to keep the continuity of the true phase value when the computed phase changes branches. In general, more information is required to specify m. However, ϕ_s can be assumed to be approaching zero at low frequencies for small dispersive samples.

8.1.3 Double-pass Transmission

The setup for a double-pass transmission measurement requires less complication since a sample is just inserted into the fixed arm of a Michelson interferometer. A schematic diagram of the setup is shown in Figure 8.2(b). The measurement can be done in a similar manner as the single-pass transmission measurement for interferogram recording and for computation. Since the radiation propagates through the sample twice, the transmission interferogram is shifted from the center of the radiation interferogram by $2b = 2(\bar{n} - 1)d$ and the sample frequency-response is that of the single-pass transmission squared.

$$\tilde{S}(\omega) = \frac{\mathrm{FT}\{I_1(\delta)\}}{\mathrm{FT}\{I_0(\delta)\}} = \frac{e^{i4\pi\nu b}\mathrm{FT}\{I_1(\delta - 2b)\}}{\mathrm{FT}\{I_0(\delta)\}} = |S|\, e^{i\phi_s} = \frac{\tilde{E}_1(\omega)}{\tilde{E}_0(\omega)} = (\tilde{t}_{12}\tilde{a}_2\tilde{t}_{21})^2 e^{-i2\omega d/c}. \tag{8.16}$$

The real and imaginary parts of the complex refractive index can then be obtained from the phase ϕ_s and the amplitude $|S|$ by

$$n_r(\nu) = 1 + \frac{1}{4\pi\nu d}\left[\phi_s(\nu)\right]. \tag{8.17}$$

$$n_i(\nu) = \frac{1}{4\pi\nu d}\ln\left[\frac{16 n_r(\nu)^2}{|S(\nu)|\left[1 + n_r(\nu)\right]^4}\right]. \tag{8.18}$$

8.1.4 Two-interface Reflection

Reflection from two interfaces has been used to determine complex refractive indices of transparent solids. The setup is just the same as the one for a double-pass transmission measurement, in which a sample is inserted into the fixed arm of a Michelson interferometer. In this measurement, the interferograms of interest are associated with reflections from the two interfaces of the sample, the radiation interferogram is therefore not required. Since the two reflection interferograms can be taken with the presence of the sample in the interferometer, interruption for setting up the sample is eliminated. Moreover, both interferograms can be recorded in one scan.

Figure 8.4 shows a schematic diagram of the reflection from the front and rear

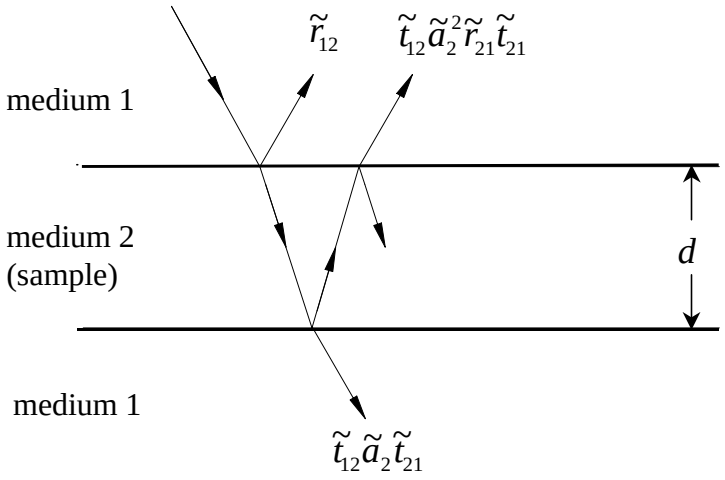

Figure 8.4: A schematic diagram of reflection from two interfaces.

interface of the sample. Having a sample placed in the fixed arm of the interferometer, the reflected field at the front interface is $\tilde{E}_F(\omega) = \tilde{r}_{12}\tilde{E}_0(\omega)$ while that at the rear interface is $\tilde{E}_R(\omega) = \tilde{t}_{12}\tilde{a}_2^2\tilde{r}_{21}\tilde{t}_{21}\tilde{E}_0(\omega)$, where $\tilde{r}_{12}$, $\tilde{r}_{21}$, $\tilde{t}_{12}$, $\tilde{t}_{21}$ are reflection and transmission coefficients described in Appendix B. Again, the sample should be sufficiently thick to be able to observe the two reflection interferograms separately. In this measurement, the concept of sample frequency-responses is not applied since we are interested in the radiation interferogram. We will use the relative frequency-response $\tilde{\gamma}(\omega)$, defined as the ratio of the Fourier transforms of the interferograms from the two interfaces, to calculate the complex refractive index. The relative frequency-response is

$$\begin{aligned} \tilde{\gamma}(\omega) &= \mathrm{FT}\{I_R(\delta)\}/\mathrm{FT}\{I_F(\delta)\} \\ &= e^{i2\omega b/c}\mathrm{FT}\{I_R(\delta-2b)\}/\mathrm{FT}\{I_F(\delta)\} = |\gamma|\, e^{i\phi_\gamma}, \end{aligned} \tag{8.19}$$

where $I_F(\delta)$ and $I_R(\delta - b)$ are the interferograms associated with the front and rear interface reflections. The two interferogram signatures are separated by $2b = 2\bar{n}d$.

The relative frequency-response can be related to optical coefficients by (Figure 8.4)

$$\begin{aligned}\tilde{\gamma}(\omega) &= \frac{\mathrm{FT}\{I_R(\delta)\}}{\mathrm{FT}\{I_F(\delta)\}} = \frac{\tilde{E}_R(\omega)}{\tilde{E}_F(\omega)} = \frac{\tilde{t}_{12}\tilde{a}_2^2\tilde{r}_{21}\tilde{t}_{21}}{\tilde{r}_{12}} \\ &= \frac{4\tilde{n}}{(1+\tilde{n})^2} e^{-2\omega n_i d/c} e^{i(2\omega n_r d/c+\pi)} = |\gamma|\, e^{i\phi_\gamma}. \end{aligned} \tag{8.20}$$

The phase of ϕ_γ and amplitude $|\gamma|$ of $\tilde{\gamma}(\omega)$ from the measurement and (8.20) allow us to calculate the refractive index assuming $n_r \gg n_i$ by

$$n_r(\nu) = \frac{1}{4\pi\nu d}\left[\phi_\gamma - \pi\right], \tag{8.21}$$

$$n_i(\nu) = \frac{1}{4\pi\nu d} \ln\left[\frac{4n_r(\nu)}{|\gamma|\left[1+n_r(\nu)\right]^2}\right]. \tag{8.22}$$

Some refractive index measurements based on the DFTS technique have been conducted at SUNSHINE to demonstrate the use of transition radiation generated from short electron bunches to spectroscopy applications. Silicon is selected to be a sample for the refractive index measurement. It is often used as a window material for far-infrared spectroscopy of liquid samples due to its high transparency in this spectral regime. The refractive index of silicon is also high enough so that a thin sample can be used, resulting in well-separated interferogram signatures. As a demonstration, the refractive index of silicon is measured by a double-pass transmission measurement and a two-interface reflection measurement. The determination of the refractive index of the pyroelectric detector crystal using DFTS will also be discussed.

8.2 Refractive Index Measurement for Silicon

Measurements of silicon refractive index have been conducted as examples of far-infrared spectroscopy using coherent transition radiation generated at SUNSHINE. The measurements shown here were not aimed for high accuracy, but rather to demonstrate the concept. A few simplifications, therefore, have been made in the data analysis. More measurements of the silicon refractive index will be available in the future, as the spectroscopy of liquid samples is being pursued at SUNSHINE.

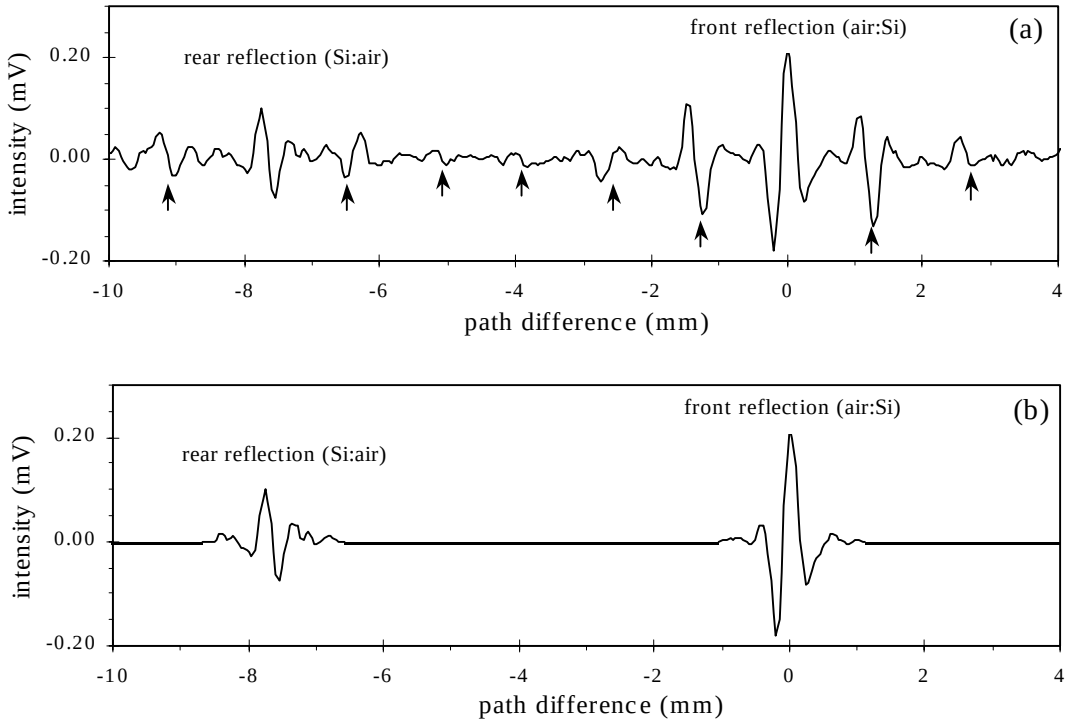

Figure 8.5: Front and rear interface reflection of the silicon sample.

The silicon sample used in the measurements is 1.12-mm thick, 25-mm in diameter, undoped, and polished optically flat on both sides. Since silicon is transparent in the far-infrared, we can use the measurement of the reflection from the two interfaces and the double-pass transmission measurement. Both measurements can be done using the same setup by placing the sample in the fixed arm normal to the radiation beam in a Michelson interferometer.

8.2.1 Two-interface Reflection Measurement

The interferogram containing reflection from the front and rear interface can be obtained in one scan. Figure 8.5(a) shows the interferogram displaying both the front-interface-reflection signature and the rear-interface- reflection signature. Note that a negative path difference represents a longer path difference than the zero path difference. The signature of multiple reflections in the detector crystal, indicated by

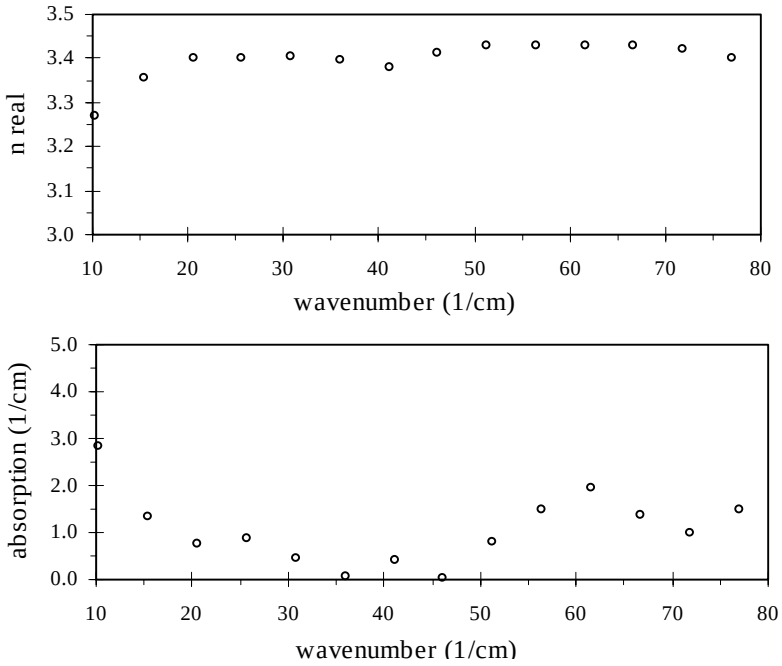

Figure 8.6: Calculated refractive index of silicon from two-interface reflection measurement.

arrows, are clearly visible in the interferogram. These signatures cause zero intervals in the radiation spectrum as discussed in Section 5.4.2. To avoid these zero intervals in the spectrum, we use only short pieces of the interferogram containing the signatures of interest. Figure 8.4(b) shows sections of the interferogram containing the front-interface and rear-interface reflection which will be used in the calculation. As a short length of the interferogram is considered, the spectral resolution is unfortunately reduced and any narrow absorption lines, which might be there, cannot be resolved. With the scan length of 2 mm, the spectral resolution is 5 cm^{-1}. This resolution is good enough for the refractive index measurement of silicon which is known to have no absorption in the far-infrared region. For measurements that require high resolution, a different kind of detector can be used to avoid the interference signatures in the interferogram. Another alternative is to use an editing technique described in Ref. [41] to replace interference signatures by baseline. This technique, however, should be applied with cautions since it might disturb frequency information in the

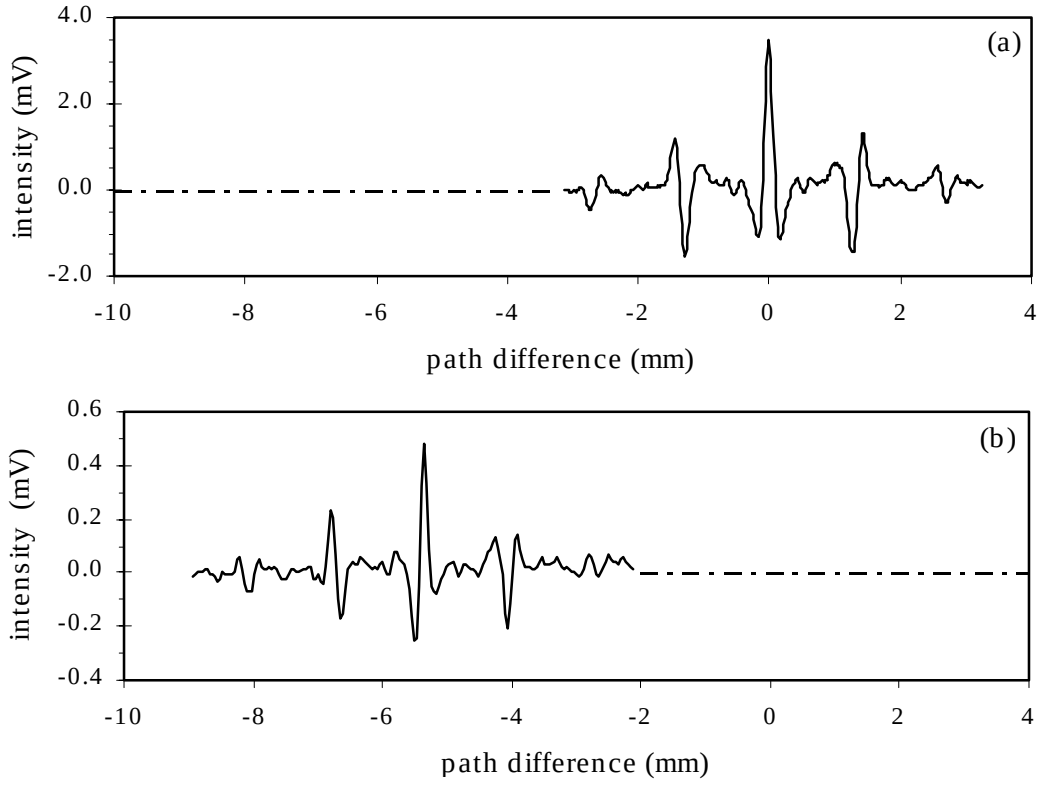

Figure 8.7: Double-pass transmission measurement of silicon: (a) radiation interferogram and (b) transmission iterferogram.

interferogram.

The complex refractive index of the silicon can be obtained from (8.21) and (8.22) following the procedures discussed in Section 8.1.4. The real refractive index and the absorption are shown in Figure 8.6. The real refractive index is quite constant over the frequencies from 10 cm^{-1} to 70 cm^{-1} and the absorption $\alpha = 4\pi\nu n_i$ is smaller than 3.0 cm^{-1} in this frequency range. A comparison of these results to the results from other reported experiments will be discussed in the data analysis.

8.2.2 Double-pass Transmission Measurement

Unlike a two-interface reflection measurement, a double-pass transmission measurement requires two scans. First, we record a radiation interferogram and then record

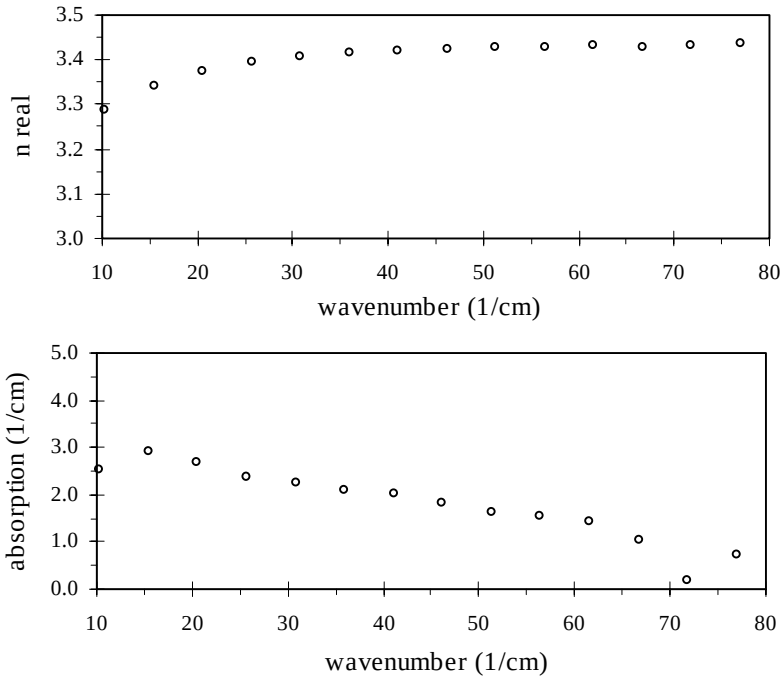

Figure 8.8: Calculated refractive index of silicon from the double-pass transmission measurement.

a transmission interferogram after placing the sample in the fixed arm of the interferometer. The radiation interferogram and the transmission interferogram are shown in Figure 8.7(a) and Figure 8.7(b), respectively. The transmission interferogram signatured has shifted 5.36 mm from the center of the radiation interferogram. We use a 2-mm-long interferogram to calculate the refractive index, giving a resolution of 5 cm^{-1}. Following the procedure in Section 8.1.3, we can calculate the real refractive index and absorption of silicon using (8.17) and (8.18). The results are shown in Figure 8.8. The real refractive index is again constant about 3.42 and the absorption is of the same order as that obtained from the double-pass transmission measurement.

8.2.3 Data Analysis

Figure 8.9 shows our experimental results compared to those reported in Refs. [42] and [43]. The real refractive index obtained from our measurements compares well

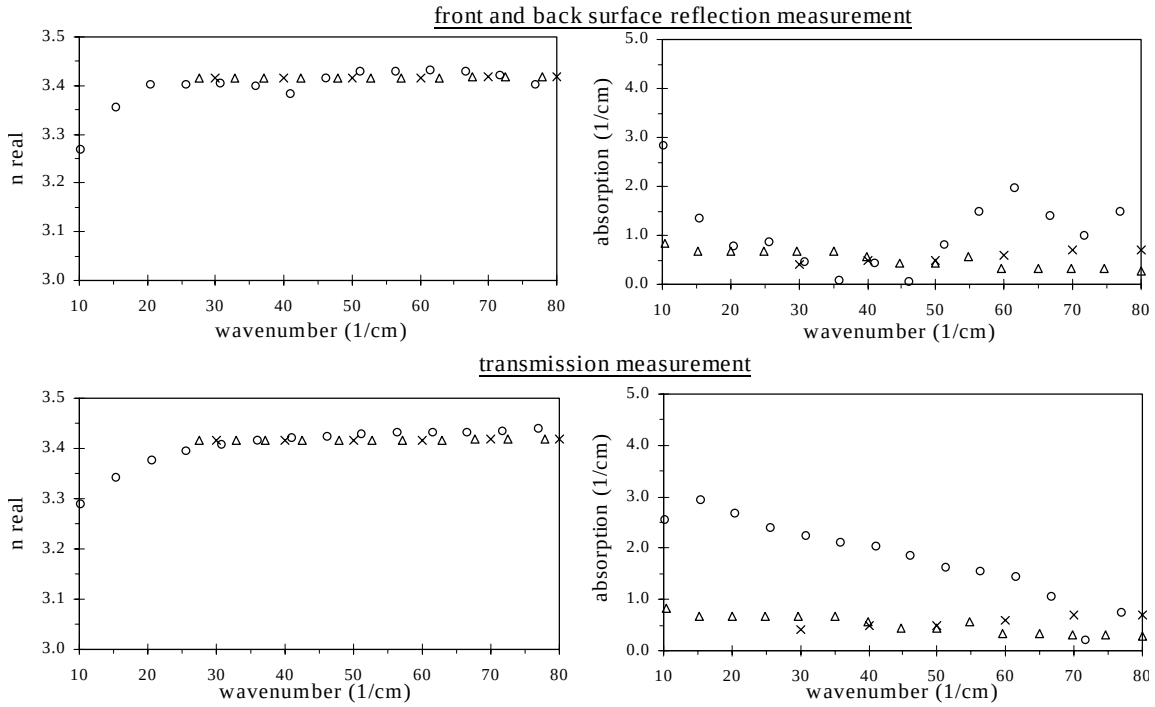

Figure 8.9: Experimental results for refractive index of silicon (o : our measurement, Δ : Reference [42], $\times$: Reference [43]).

with the results from others. The measurements confirm that silicon has an almost constant real refractive index of about 3.42 in the far-infrared regime. The absorption is, however, higher in our measurements compared to those in the literature. Both transmission measurement and two-interface reflection measurement give an absorption for the silicon sample up to 3 cm^{-1}, but the literature values for the absorption are less than 1 cm^{-1}. It is possible that this increased absorption results from our particular silicon sample which has a reduced resistivity. Unfortunately, exact information on the silicon crystal is not available from the vendor (Infrared Lab). According to Ref. [44], a silicon crystal with low resistivity features absorption at long wavelengths. More studies of a high resistivity silicon crystal will be reported in future work. A high resistivity silicon is suitable for and will be used as the window for a liquid sample holder [45].

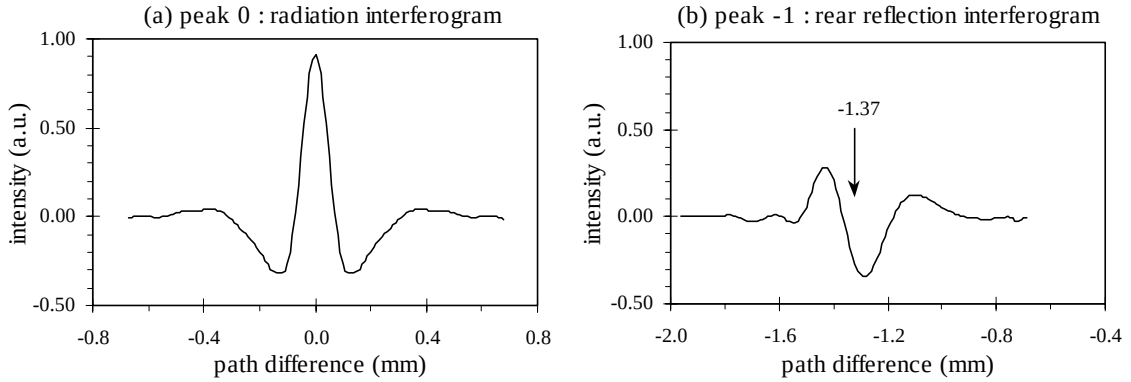

Figure 8.10: Radiation interferogram and rear interface reflection interferogram of the pyroelectric detector crystal ($LiTaO_3$).

8.3 Refractive Index Measurement for $LiTaO_3$

We consider the refractive index calculation for the pyroelectric detector crystal ($LiTaO_3$) as a by-product of the bunch length analysis. After being able to identify the cross-correlation of multiple reflections in the detector crystal, we realize that we can consider an interferogram taken by the pyroelectric detector as one obtained from a DFTS measurement having the detector crystal as a sample. An interferogram taken by the pyroelectric detector displaying multiple reflections is shown in Figure 5.6 and a detailed explanation of each signature is described by schematic diagrams in Figure 5.7. The main peak of the interferogram (signature 0) is just a radiation interferogram while the signature -1 is equivalent to the interferogram taken with the sample in the fixed arm. Figure 8.10 shows signature 0 and signature -1 of the interferogram taken with the pyroelectric detector which are associated with radiation interferogram and rear interface interferogram, respectively.

The sample frequency-response for this case is given by

$$\tilde{S}(\omega) = \frac{\mathrm{FT}\{I_{-1}(\delta)\}}{\mathrm{FT}\{I_0(\delta)\}} = \frac{e^{i2\omega b/c}\mathrm{FT}\{I_{-1}(\delta - 2b)\}}{\mathrm{FT}\{I_0(\delta)\}} = |S|\, e^{i\phi_s} = \frac{\tilde{E}_{-1}(\omega)}{\tilde{E}_0(\omega)} = (\tilde{t}_{12}\tilde{a}_2)^2 e^{i\pi}. \tag{8.23}$$

$I_0(\delta)$ is the radiation interferogram and $I_{-1}(\delta - 2b)$ is the rear interface reflection interferogram being shifted by $2b = 2\bar{n}d$ from the radiation interferogram. The transmission coefficient $\tilde{t}_{12}$ and the propagation factor $\tilde{a}_2$ are defined in Appendix B. The real refractive index can be obtained from the phase ϕ_s and amplitude $|S|$of $\tilde{S}(\omega)$ in (8.23) by

$$n_r(\nu) = \frac{1}{4\pi\nu d}\left[\phi_s(\nu) - \pi\right], \tag{8.24}$$

where $\nu = \omega/2\pi c$.

The calculated real refractive index of the pyroelectric detector crystal is shown in Figure 8.11. The real refractive index increases from $n_r = 6.79$ at 12 cm^{-1} to $n_r = 6.81$ at 75 cm^{-1}. The absorption of the crystal can not be calculated because some of the required parameters are not available. These parameters are, for example, the absorption, reflection and transmission coefficients of the metallic coatings.

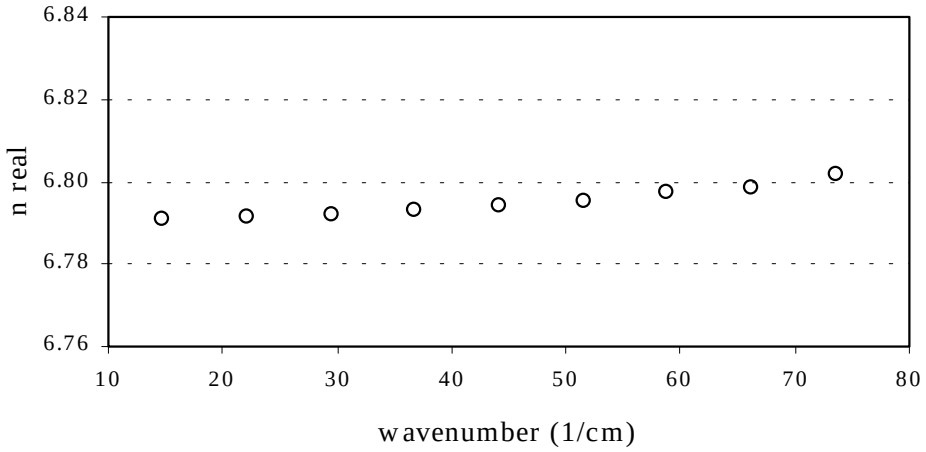

Figure 8.11: Calculated refractive index of the pyroelectric detector crystal ($LiTaO_3$).

Chapter 9

Summary

This thesis describes the generation, characterization and use of coherent far-infrared radiation from short electron bunches. The studies are based on two important aspects of coherent radiation; high intensity and its radiation spectrum which is determined by the bunch distribution. High intensity coherent transition radiation emitted from femtosecond electron pulses has a high potential to become a high brightness, coherent, polarized far-infrared radiation source for scientific and applied research. Because the coherent radiation spectrum which carries information of bunch distribution, the bunch length can be extracted from an autocorrelation of coherent radiation emitted by the electron bunch. This technique is capable of measuring a bunch length well below one picosecond.

9.1 FIR Radiation Source

Coherent transition radiation generated from femtosecond electron bunches at SUNSHINE covers much of the far-infrared spectral range. The radiation radiance (W/mr^2 $/mm^2/100\%BW$) is four to seven orders of magnitude above that of back body radiation and is at least three orders of magnitude above that of synchrotron radiation estimated using parameters from a typical VUV ring; E = 800 MeV, I_b= 500 mA, and B =1.4 T (Figure 4.17). High intensity radiation from millimeter waves up to

100 cm^{-1} can be detected by a room temperature detector. The radiation pulse duration is as short as $\sigma_z = 35$ μm (120 fs). Up to 400 μJ of radiation energy per macropulse, which contains about 3000 radiation pulses, has been observed. The radiation is collected within an acceptance angle of ± 154 mrad which is equivalent to a 38% collection efficiency for a 25 MeV electron beam.

Similarly, coherent diffraction radiation can be considered as another potential high intensity far-infrared radiation source. Although the radiation intensity is somewhat lower than coherent transition radiation when generated by a 25 MeV beam, the intensity still greatly exceeds that of a conventional blackbody radiation source. Moreover, the radiation emission process is nondestructive which allows a series of radiators along the beam line to be driven by the same electron beam.

9.2 Bunch Length Measurement

The bunch length measurement technique based on the autocorrelation of coherent transition radiation is a frequency-domain measurement and it is capable of measuring femtosecond bunches. Since bunch lengths are determined by frequency information obtained from the measurement, any impacts of experimental conditions on the measured radiation spectrum can potentially disturb bunch length measurements. These impacts can easily lead to wrong experimental conclusions and need to be considered to interpret the measurement correctly. This thesis addresses several effects such as the spectral sensitivity of pyroelectric detector, the absorption in humid air, and beam size effects. Multiple reflections occur within the pyroelectric detector crystal. Reflected pulses can interfere with incoming radiation pulses at a non-zero path difference in an interferogram causing a cross-correlation signature. These signatures must be identified and ruled out so that the bunch length is determined solely by an autocorrelation of coherent radiation emitted from the electron bunch. For convenience, a bunch length measurement can be done in air but the measured bunch length may appear longer due to dispersive effects. The dispersion causes the coherent radiation-pulse to become broader after propagating through ambient air, especially the radiation emitted from short bunches which extends over a broad spectral range.

Our measurements show that a $\sigma_z = 38$ μm radiation-pulse becomes 25% longer after propagating through 80 cm of ambient air. In addition, the effects of the beam size on the bunch length measurement was also demonstrated. Contribution of transverse distribution suppresses high frequency components of the coherent radiation. Non-axial observation will make a measured bunch length become a combination of the transverse and longitudinal distribution. Effects of the beam size on the bunch length measurement depends on the beam size, bunch length and observation angle. For an accurate bunch length measurement, the contribution of the transverse distribution must be minimized which can be done by limiting the observation angles θ to a small angle and by minimizing the spot size σ_ρ at the radiator such that $\sigma_\rho \sin\theta \ll \sigma_z \cos\theta$.

For nondestructive bunch length measurements, coherent diffraction radiation can be employed. However, subtleties of the diffraction radiation spectrum make a bunch length measurement and data analysis more elaborate in some cases. Depending on the beam energy, bunch length, and aperture sizes, more or less corrections must be applied. Simulations and practical guidelines for measurement have been described to minimized the need for such corrections. Bunch length measurements using coherent transition radiation is recommended to calibrate the coherent diffraction radiation bunch length measurement system.

9.3 Stimulated Coherent TR

Stimulation of coherent transition radiation by the radiation fields of previous electron bunches is observed. The radiation pulses emitted from previous bunches are circulated in an optical cavity while adjusting the cavity length such that these radiation pulses coincide at the radiator with an incoming electron bunch to stimulate more radiation from the electrons. Metallic mirrors and reflectors are arranged in an optical cavity such that the circulated radiation pulses arrive at the radiator with the correct phase and polarization. The cavity performance is measured by comparing the radiation intensity on and off resonance while varying the cavity length. We observed stimulated transition radiation up to the 9^{th} order resonance. With a 25-μm-thick beam divider, we can obtain a factor of nine for the stimulation enhancement. The

cavity, however, still has high losses from absorption in humid air, from non-perfect reflection, from mirror diffraction, and from radiation extraction. To improve the cavity performance (higher stimulation enhancement), a better designed and engineered cavity must be considered.

9.4 Far-infrared Spectroscopy

Optical properties of silicon were measured as an example of far-infrared spectroscopy using our radiation source. High intensity far-infrared radiation from femtosecond electron bunches allows the experiments to be conducted easily. Far-infrared spectroscopy, based on the Dispersive Fourier Transform Spectroscopy (DFTS) technique can be applied to measure the complex refractive index of solid and liquid samples, including highly absorbing substances. Such measurements are in progress at the SUNSHINE facility as part of another Ph.D. program. The high intensity and short duration of the radiation are essential to conduct such measurements.

Appendix A

Dielectric Constant of Aluminum

The complex dielectric constant of aluminum using the Drude's model is [46, 47]

$$\epsilon(\omega) = 1 - \frac{\Omega_p^2}{\omega(\omega + i/\tau)} + \delta\epsilon, \tag{A.1}$$

where ω is an angular frequency ($2\pi f$), Ω_p is the plasma frequency of aluminum, τ is the relaxation time for conducting electrons and $\delta\epsilon$ is small contribution from bound-electron absorption. The plasma frequency expressed in terms of the dc conductivity σ_0 and the relaxation time τ is

$$\Omega_p^2 = 4\pi\sigma_0/\tau, \tag{A.2}$$

The dielectric constant of Aluminum can be calculated using (A.1) and parameters listed in Table A.1. The contribution from $\delta\epsilon$ for good conductors in the far-infrared region can be neglected [**?**]. Figure A.1 shows the absolute value of the dielectric constants of aluminum in the far-infrared spectral range.

$\sigma_0(\text{sec}^{-1})$	$\tau(\text{sec})$
3.18×10^{17}	0.801×10^{-14}

Table A.1: DC conductivity and relaxation time of aluminum .

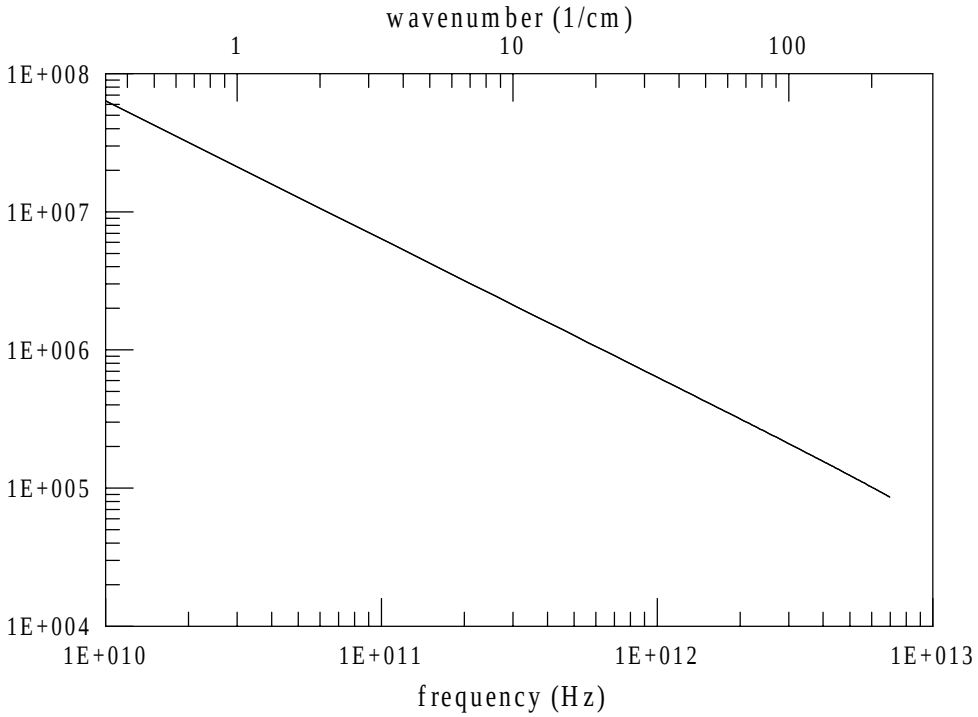

Figure A.1: Calculated dielectric constant for aluminum in the far-infrared spectral range.

Appendix B

Transmission and Reflection of a Sample

The purpose of this Appendix is to provide the general background for reflection and transmission of an electromagnetic wave on and through a sample [Ref. [41]].

B.1 At an Interface

The amplitude attenuation and phase shift of an electromagnetic wave due to reflection on or transmission through a plane interface are described by Fresnel's equations. These equations relate these effects to the optical constants, the angle of incidence and the polarization of the incident wave.

The Fresnel's equations are:

$$\begin{aligned} \tilde{r}_{\perp} &= \left(\tilde{n}_1 \cos\theta_1 - \tilde{n}_2 \cos\theta_2\right) / \left(\tilde{n}_1 \cos\theta_1 + \tilde{n}_2 \cos\theta_2\right), \\ \tilde{r}_{\parallel} &= \left(\tilde{n}_1 \cos\theta_2 - \tilde{n}_2 \cos\theta_1\right) / \left(\tilde{n}_1 \cos\theta_2 + \tilde{n}_2 \cos\theta_1\right), \\ \tilde{t}_{\perp} &= 2\tilde{n}_1 \cos\theta_1 / \left(\tilde{n}_1 \cos\theta_1 + \tilde{n}_2 \cos\theta_2\right), \\ \tilde{t}_{\parallel} &= 2\tilde{n}_1 \cos\theta_1 / \left(\tilde{n}_1 \cos\theta_2 + \tilde{n}_2 \cos\theta_1\right), \end{aligned} \tag{B.1}$$

where r and t is the amplitude reflection and transmission coefficients for the component of the incident wave polarized perpendicular to ($\perp$) and for that parallel ($\parallel$)

to the plane of incidence. The equations described the wave which is incident from medium 1 with an incident angle of $\theta_1$and transmit to medium 2 with the angle θ_2. The two angles are related by Snell's law

$$\tilde{n}_1 \sin\theta_1 = \tilde{n}_2 \sin\theta_2. \tag{B.2}$$

For the case of normal incidence from medium 1 to medium 2 the Fresnel's equations can be reduced to

$$\tilde{r}_\perp = \tilde{r}_\parallel = \tilde{r}_{12} = (\tilde{n}_1 - \tilde{n}_2)\,/\,(\tilde{n}_1 + \tilde{n}_2)\,, \tag{B.3}$$

$$\tilde{t}_\perp = \tilde{t}_\parallel = \tilde{t}_{12} = 2\tilde{n}_1/\,(\tilde{n}_1 + \tilde{n}_2)\,. \tag{B.4}$$

On the other hand, the equations for normal incidence from medium 2 to medium 1 are

$$\tilde{r}_{21} = -\tilde{r}_{12}, \tag{B.5}$$

$$\tilde{t}_{21} = \tilde{n}_2\tilde{t}_{12}/\tilde{n}_1. \tag{B.6}$$

When the medium 1 is vacuum with $\tilde{n}_1 = 1$, the Fresnel's equations become

$$\tilde{r}_{12} = (1-\tilde{n}_2)/(1+\tilde{n}_2), \tag{B.7}$$

$$\tilde{t}_{12} = 2/(1+\tilde{n}_2), \tag{B.8}$$

$$\tilde{r}_{21} = -\tilde{r}_{12}, \tag{B.9}$$

$$\tilde{t}_{21} = \tilde{n}_2\tilde{t}_{12}. \tag{B.10}$$

The more useful forms of Fresnel's equations are the exponential forms since the attenuation and phase terms are well separated. The amplitude reflection coefficient can be written in the form

$$\tilde{r}_{12} = |r_{12}|\, e^{i\phi_r}, \tag{B.11}$$

where $|r_{12}|$ is the magnitude which represent the attenuation and ϕ_r is the phase shift

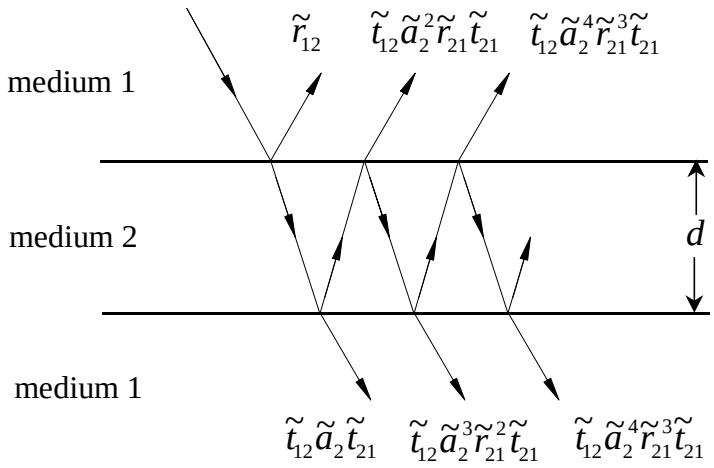

Figure B.1: Multiple reflection from and transmission through a sample (medium 2) immersed in a medium 1.

from the reflection. The amplitude transmission coefficient can be written in the form

$$\tilde{t}_{12} = |t_{12}|\, e^{i\phi_t}, \tag{B.12}$$

where $|t_{12}|$ is the magnitude which represent the attenuation and ϕ_t is the phase shift due to the transmission.

B.2 Of a Plane Parallel Sample

The Transmission and reflection of a plane parallel sample is an extended discussion from the transmission and reflection at an interface. Let us first introduce the complex propagation factor $\tilde{a}$ of the medium with a complex refractive index $\tilde{n} = n_r + in_i$, defined by

$$\tilde{a} = e^{-i\omega\tilde{n}x/c} = e^{-2\pi n_i \nu x} e^{i2\pi n_r \nu x}, \tag{B.13}$$

where x is the propagating distance in the medium, ω is the frequency of the wave and c is the velocity of light and the wave number $\nu = \omega/(2\pi c)$.

Consider, a plane parallel sample of refractive index $\tilde{n}_2$ and a thickness of d immersed in a medium of refractive index $\tilde{n}_1$, as shown in Figure B.1. The complex propagation factor of the medium $\tilde{a}_2 = e^{-i\omega\tilde{n}d/c}$. An incident electromagnetic wave is subjected to multiple internal reflections at the two interfaces between mediums. The total reflected and transmitted waves are given by the infinite sum of all partially reflected and transmitted waves. The total amplitude transmission (T) and reflection (R) coefficients are, then, given by

$$T = \tilde{t}_{12}\tilde{a}_2\tilde{t}_{21} + \tilde{t}_{12}\tilde{a}_2^3\tilde{r}_{21}^2\tilde{t}_{21} + \tilde{t}_{12}\tilde{a}_2^5\tilde{r}_{21}^4\tilde{t}_{21} + ... \quad \text{(B.14)}$$

$$R = \tilde{r}_{12} + \tilde{t}_{12}\tilde{a}_2^2\tilde{r}_{21}\tilde{t}_{21} + \tilde{t}_{12}\tilde{a}_2^4\tilde{r}_{21}^3\tilde{t}_{21} + ... \quad \text{(B.15)}$$

Here, $\tilde{t}_{12}, \tilde{t}_{21}, \tilde{r}_{12}, \tilde{r}_{21}$ are the Fresnel transmission and reflection coefficients at the interfaces between two mediums in the order defined by the sequence of subscripts shown.

Bibliography

[1] P. Kung, *Generation and Characterization of Subpicosecond Electron Bunches*, PhD thesis, Stanford University, California, 1995.

[2] H. Lihn, P. Kung, C. Settakorn and H. Wiedemann, "Measurement of subpicosecond electron pulses", *Physical Review E*, vol. 53, no. 6, pp. 6413–6418, 1996.

[3] H. Lihn, *Stimulated Transition Radiation*, PhD thesis, Stanford University, California, 1996.

[4] Committee on Free Electron Lasers and Other Advanced Coherent Light Sources, *Free Electron Lasers and Other Advanced Sources of Light*, National Academy Press, Washington, D.C., 1994.

[5] The UCSB Free Electron Lasers, http://sbfel3.ucsb.edu, 2001.

[6] Stanford Picosecond FEL center, http://www.stanford.edu/group/FEL/, 2001.

[7] The CLIO FEL facility, http://www.lure.u-psud.fr/clio.htm, 2001.

[8] The FELix IR user facility, http://ns2.rijnh.nl/n4/n3/f1234.htm, 2001.

[9] G. W. Chantry, *Submillimetre Spectroscopy*, Academic Press, London, 1971.

[10] V. Ginsburg and I. Frank, "Radiation of a uniformly moving electron due to its transition from one medium into another", *Journal Of Physics*, vol. 9, pp. 353, 1945.

[11] M. L. Ter-Mikaelian, *High-energy Electromagnetic Process in Condensed Media*, Wiley-Intersciencer, New York, 1972.

[12] V. L. Ginzburg and V. N. Tsytovich, Eds., *Transition Radiation and Transition Scattering*, Adam Hilger, Bristol, 1990.

[13] L. D. Landau and E. M. Lifshitz, *Electrodynamics of Continuous Media*, 2nd edition, Pergamon Press, Oxford, 1984.

[14] H. Motz, "Applications of the radiation from fast electron beams", *Journal of Applied Physics*, vol. 22, no. 5, 1951.

[15] M. Borland, *A High-brightness Thermionic Microwave Electron Gun*, PhD thesis, Stanford University, California, 1991.

[16] P. Kung, D. Bocek, H. Lihn and H. Wiedemann, "High-intensity coherent FIR radiation from sub-picosecond electron bunches", in *Proceeding of SPIE Gas, Metal Vapor and Free Electron Lasers and Applications*, V. N. Similey and F. K. Tittel, Eds., Los Angeles, 1994, pp. 491–201, SPIE.

[17] Infrared optical Products, Inc., *Optical Products for the Infrared*, Farmingdale, New York, 1990.

[18] R. V. McKnight and K. D. Moller, "Far-infrared spectrum of high-density polyethylene plates", *Journal of the Optical Society of America*, vol. 54, pp. 132, 1964.

[19] W. B. Tiffany, "The amazing versatile pyroelectric", Tech. Rep., Molectron Detector, Inc., Oregon.

[20] R. J. Bell, *Introductory Fourier Transform Spectroscopy*, Academic Press, London, 1972.

[21] E. Hecht and A. Zajac, *Optics*, 2nd edition, Addison Wesley, Reading, Massachusetts, 1990.

[22] J. S. Nodvick and D. S. Saxon, "Supression of coherent radiation by electrons in a synchrotron", *Physicsl Review*, vol. 96, pp. 180–184, 1954.

[23] A. R. Hight Walker T.B. Lucatorto et. al. U. Arp, G. T. Fraser, "Spontaneous coherent microwave emission and the sawtooth instability in a compact storage", *Physical Review Special Topics - Accelerators and Beams*, vol. 4, no. 054401, pp. 1–9, 2001.

[24] M. Born and E. Wolf, *Principles of Optics*, 6th edition, Pergamon Press, Oxford, 1990.

[25] A. P. Potylitsyn, "Transition radiation and diffraction radiation: Similarities and differences.", *Nuclear Instruments and Method in Physics Research B*, vol. 145, pp. 169–179, 1998.

[26] W. Barry, "An autocorrelation technique for measuring sub-picosecond bunch length using coherent transition radiation", in *Proceedings of the Workshop on Advanced Beam Instrumentation*, Tsukuba, Japan, 1991, KEK Proceeding 92-1, pp. 224–235, KEK.

[27] Carlos B. Roundy, *Advance in Pyroelectic Detectors*, PhD thesis, Stanford University, California, 1973.

[28] J. D. Jackson, *Classical Electrodynamics*, 2nd edition, John Willey and Sons, Inc., Singapore, 1990.

[29] J. R. Birch, A. J. Kemp and M.N. Afsar, "The refractive index of water vapour: A comparison of measurement and theory", *Infrared Physics*, vol. 18, pp. 827–833, 1978.

[30] R. Lai and A. J. Sievers, "On using the coherent far ir radiation produced by a charged-particle bunch to determine its shape: I analysis", *Physical Review E*, vol. 53, no. 6, pp. 6413–6418, 1996.

[31] I. C. McMichael J. M. Diels, J. J. Fontaine and F. Simoni, "Control and measurement of ultrashort pulse shapes with femtosecond accuracy", *Applied Optics*, vol. 24, no. 2, pp. 1270–1282, 1985.

[32] J. C. Diels and C. Yan, "Amplitude and phase recording of ultrashort pulses", *Journal of the Optical Society of America B*, vol. 8, pp. 1259–1263, 1991.

[33] K. Mogi, K. Naganuma and H. Yamada, "Time direction determination of asymmetric ultrashort optical pulses from second-harmonic generation autocorrelation signal", *Applied Physics Letters*, vol. 54, pp. 1201–1202, 1989.

[34] J. L. A. Chilla and O. E. Martinez, "Analysis of a method of phase measurement of ultrashort pulses in the frequency domain", *IEEE Journal of Quantum Electronics*, vol. 27, no. 5, pp. 1228–1235, 1991.

[35] D. J. Kane and R. Trebino, "Characterization of arbitrary femtosecond pulses using frequency-resolved optical gating", *IEEE Journal of Quantum Electronics*, vol. 29, no. 2, pp. 571–579, 1993.

[36] Yu. N. Dnestrovskii and D. P. Kostomarov, "A study of ultrarelativistic charges passing through a circular aperture in a screen", *Soviet Physics Doklady*, vol. 4, pp. 158–160, 1959.

[37] Yu. N. Dnestrovskii and D. P. Kostomarov, "Radiation of a modulated beam of charged particles in passing through a round opening in a flat screen", *Soviet Physics Doklady*, vol. 4, pp. 132–135, 1959.

[38] B. M. Bolotovskii and G. V. Voskresenskii, "Diffraction radiation", *Soviet Physics Uspekhi*, vol. 9, no. 6, pp. 73–96, 1966.

[39] Y. Shibata, S. Hasebe, K. Ishi and et al. "Observation of coherent diffraction radiation from bunched electrons passing through a circular aperture in the millimeter- and submillimeter-wavelength regions", *Physical Review E*, vol. 52, no. 6, pp. 6787–6794, 1995.

[40] H. Lihn, P. Kung, C. Settakorn and H. Wiedemann, "Stimulated transition radiation in the far-infrared", *Physical Review Letters*, vol. 76, no. 22, pp. 4163–4166, 1996.

[41] J. R. Birch and T. J. Parker, "Dispersive fourier transform spectroscopy", in *Infrared and Millimeter Waves V.2: Instrumentation*, K. J. Button, Ed., pp. 137–271. Academic Press, New York, 1979.

[42] C. Randall and R. Rawcliffe, "Refractive indices of germanium, silicon, and fused quartz in the far infrared", *Applied Optics*, vol. 6, no. 11, pp. 1889–1895, 1967.

[43] D. Smith, E. Loewenstein and R. Morgan, "Optical constants of far-infrared materials (2: Crystaline solids)", *Applied Optics*, vol. 12, no. 2, pp. 398–406, 1973.

[44] M. Exter D. Grischkowsky, S. Keiding and Ch. Fattinger, "Far-infrared time-domain spectroscopy with terahertz beams of dielectrics and semiconductors", *Journal of the Optical Society of America B*, vol. 7, no. 10, pp. 2006–2015, 1990.

[45] K. Woods, Private communication.

[46] H. E. Bennett and J. M. Bennet, "Validity of the drude theory for silver, gold and aluminum in the infrared", in *Optical Properties and Electronics Structure of Metals and Alloys*, F. Abeles, Ed., pp. 175–188. North-Holland, Amsterdam, 1966.

[47] D. Y. Smith, E. Shiles and M. Inokuti, "Optical Properties of Metallic Aluminum", in *Handbook of Optical Constants of Solids*, E. D. Palik, Ed., pp. 369–395, Academic Press, New York, 1985.